
Theses and Dissertations

2006

Stability analysis of atomic structures

Liang Zhang
University of Iowa

Follow this and additional works at: <https://ir.uiowa.edu/etd>

 Part of the [Mechanical Engineering Commons](#)

Copyright 2006 Liang Zhang


This dissertation is available at Iowa Research Online: <https://ir.uiowa.edu/etd/70>

Recommended Citation

Zhang, Liang. "Stability analysis of atomic structures." PhD (Doctor of Philosophy) thesis, University of Iowa, 2006.

<https://doi.org/10.17077/etd.db098kec>

Follow this and additional works at: <https://ir.uiowa.edu/etd>

 Part of the [Mechanical Engineering Commons](#)

STABILITY ANALYSIS OF ATOMIC STRUCTURES

by
Liang Zhang

An Abstract

Of a thesis submitted in partial fulfillment
of the requirements for the Doctor of
Philosophy degree in Mechanical Engineering
in the Graduate College of
The University of Iowa

December 2006

Thesis Supervisor: Assistant Professor Jia Lu

ABSTRACT

The stability and failure mechanism of a structure at the nanometer scale are important for understanding the mechanical behavior of nanoscale materials and structures. This thesis focuses on the material stability of atomic structures. First, the material stability of pristine carbon nanotubes is investigated at the continuum level by using the crystal elasticity theory. A homogenized continuum model is adopted. The strong ellipticity condition is employed to capture the localized failure of carbon nanotubes. The critical strain and strength predicted are reasonably comparable with experimental estimations.

An atomic material stability theory is developed as the atomistic counterpart of the continuum material stability theory in nonlinear elasticity. A local instability indicator named "atomic acoustic tensor" is derived and utilized to detect material failure at the atomic scale. The stability criterion is based directly on the local energetic responses of an atomic site, and resorts to neither the continuum theory nor the pristine lattice. Thus, it is applicable to inhomogeneous atomic systems provided that the site energy can be reasonably defined.

The atomic stability theory is combined with atomistic simulation to gain understanding on crack propagation and fracture as instabilities of bond structures. The atomic acoustic tensor is used as the indicator to detect the local instability at the crack tip, and then to decide bond breaking. Quasi-static crack growth till fracture is simulated by the atomistic finite element method, which is proposed according to the form of bond potential and lattice topology.

An Eshelby-type approximate method is presented for calculating the formation energy of Stone-Wales defects. A formula is derived to show that the energy variation consists of the change of local atomic potential due to bond reconfiguration in the defective region and a higher order correction that represents the influence of the

remaining system. The method is utilized to investigate the formation energy distribution in non-uniformly deformed nanotubes and to study the energetic interaction between multiple defects.

Abstract Approved: _____
Thesis Supervisor

Title and Department

Date

STABILITY ANALYSIS OF ATOMIC STRUCTURES

by

Liang Zhang

A thesis submitted in partial fulfillment of the
requirements for the Doctor of Philosophy
degree in Mechanical Engineering
in the Graduate College of
The University of Iowa

December 2006

Thesis Supervisor: Assistant Professor Jia Lu

Graduate College
The University of Iowa
Iowa City, Iowa

CERTIFICATE OF APPROVAL

PH.D. THESIS

This is to certify that the Ph.D. thesis of

Liang Zhang

has been approved by the Examining Committee
for the thesis requirement for the Doctor of Philosophy
degree in Mechanical Engineering at the December 2006 graduation.

Thesis Committee:



Jia Lu, Thesis Supervisor




Weimin Han



Sharif Rahman



Colby Swan



Shaoping Xiao

ACKNOWLEDGEMENTS

I would like to take this opportunity to express my deep gratitude to my advisor, Dr. Jia Lu, for his guidance, patience, and support. His wealth of ideas and knowledge is one of the many reasons for my admiration. It is him who leads me to enter the realm of mechanics. I also thank Profs. Weimin HAN, Sharif RAHMAN, Shaoping XIAO, and Colby SWAN, for their instruction in courses and invaluable advices on improving my research.

I am indebted to Prof. Ray Ogden for his direction on the stability and nonlinear elasticity theories. I also give thanks to Prof. Ian Murdoch for sharing with me his knowledge.

TABLE OF CONTENTS

LIST OF TABLES	vi
LIST OF FIGURES	vii
LIST OF SYMBOLS	x
CHAPTER	
1 OVERVIEW	1
1.1 Motivation and objectives	1
1.2 Organization	4
1.3 Contributions	7
2 BACKGROUND – STABILITY THEORY OF ELASTIC SOLIDS	8
2.1 Elements of nonlinear elasticity	8
2.1.1 Kinematics and strain	8
2.1.2 Stress and constitutive law	9
2.1.3 Balance of linear momentum	10
2.2 A unified approach of stability analysis	11
2.2.1 Stability under dead loads	13
2.2.2 Stability with controlled Cauchy stress	15
2.2.3 Stability with controlled 2nd P-K stress	17
2.2.4 Stability with all fixed displacement boundaries	19
2.3 Material stability	19
2.4 Global stability v.s. local stability	21
3 LOCALIZED FAILURE OF CARBON NANOTUBES	24
3.1 Introduction	24
3.2 Analysis of strain localization	28
3.3 Extended Cauchy-Born rule	31
3.4 Strain localization of carbon nanotubes	34
3.5 Results and discussion	37
3.5.1 Uniaxial tension and compression	37
3.5.2 Pure torsion	40
4 THE ATOMISTIC FINITE ELEMENT METHOD	51

4.1	Motivation	51
4.2	Weak form: the principle of virtual work	54
4.3	Element definition	55
4.3.1	Three types of interatomic potential	55
4.3.2	Atomistic element and the new 6-node element for CNTs	57
4.4	Atomistic finite element equations	60
5	AN ATOMIC LEVEL MATERIAL STABILITY THEORY	62
5.1	Introduction	62
5.2	The strong ellipticity condition	67
5.2.1	Strong ellipticity and acoustic tensor	67
5.2.2	Singular acoustic tensor at a material point	69
5.3	The atomic acoustic tensor	70
5.3.1	Global stability of an atomic system	70
5.3.2	Atomic acoustic tensor	71
5.3.3	Implication of a singular atomic acoustic tensor	75
5.4	Application: defective simple crystals	79
5.5	Application: carbon nanotubes	83
6	CRACK GROWTH IN BRITTLE FRACTURE	102
6.1	Introduction	102
6.2	Local atomic instability and bond- breaking algorithm	107
6.2.1	The atomic acoustic tensor	107
6.2.2	Computational method and bond-breaking algorithm	108
6.3	Results and discussions	109
6.3.1	Equilibrium cracks in atomic structures	109
6.3.2	Brittle fracture of carbon nanotubes	112
6.3.3	Discussions	115
7	DEFECT ENERGETICS IN CARBON NANOTUBES	126
7.1	Introduction	126
7.2	Structural Formation Energy of Stone- Wales Defect	130
7.3	Computational Procedure	134
7.4	Results and Discussions	136
7.4.1	Cluster size	136
7.4.2	Formation energy map	138
7.4.3	Defect interaction	140

7.4.4 Discussions	141
8 SUMMARY	149
APPENDIX	152
A PROOF OF VAN HOVE'S THEOREM	152
B VAN HOVE'S THEOREM IN DISCRETE CASE	154
C TENSILE BIFURCATION OF ARMCHAIR TUBES	161
D THE ATOMIC STABILITY	163
D.1 Proof of the sufficiency of stability	163
D.2 Atomic acoustic tensor for pairwise potentials	164
E PROOF OF FORMATION ENERGY CALCULATION	166
REFERENCES	169

LIST OF TABLES

Table

3.1	Critical tensile stress and strain	48
3.2	Critical stress and strain under compression	49
3.3	Critical twist and shear stress	50
5.1	Instability modes in Mode-I and Mode-II cracks	89
5.2	Instability modes of the void under stretch	89
5.3	Tensile failure strain of pristine CNTs.	100
5.4	Tensile failure strain of defective CNTs.	101

LIST OF FIGURES

Figure		
3.1	Schematics of strain localization bands. (a) Incipieny of necking; (b) (Plastic) collapse zone, as reported by Lourie et al.	43
3.2	Global and local structures of carbon nanotubes. (a) Armchair tube; (b) a unit cell with three lattice vectors.	44
3.3	Modified Cauchy-Born rule for hexagon lattice: affine transformation and shifting vector.	45
3.4	Critical stretch versus band orientation in compression. The angle Ψ is defined such that $\mathbf{N} = (\cos \Psi, \sin \Psi)$. For zigzag tube, the critical stretch is almost constant over a range of orientation.	46
3.5	Stretch at which $\det \mathbf{Q} = 0$ versus band orientation in tension. The angle Ψ is defined such that $\mathbf{N} = (\cos \Psi, \sin \Psi)$. For armchair and zigzag tubes, the critical state occurs at $\Psi = 0$	46
3.6	Uniaxial strain-stress curves for CNTs with different chirality.	47
3.7	Shear stress versus shear strain.	47
4.1	New six-node element for carbon nanotubes	59
5.1	The local environment of an atom site a is shown in 2-D. \mathbf{r}_{ab} denotes the position vector and \mathbf{f}_{ab} represents the force between a and b parallel to \mathbf{r}_{ab} . A family of planes with normal \mathbf{n} exist spatially. The atomic traction is averaged in the assumed region with volume ω_i and measured with respect to plane \mathbf{n} . The variation of position vectors is supposed to be $\delta \mathbf{r}_{ab} = \mathbf{b}(\mathbf{r}_{ab} \cdot \mathbf{n})$. The moving magnitudes relative to a increase uniformly by ratio $(\mathbf{r}_{ab} \cdot \mathbf{n})$	90
5.2	Undeformed 2-D atomic sheets:	91
5.3	Unstable modes of atoms in the Mode-I crack. Atom 2 right at the crack tip had a longitudinal instability mode; atoms 1 and 4 were unstable by mixed modes; and atom 3 was unstable due to a shear mode. Crack would grow by breaking bonds at atom 2; meanwhile dislocations could from the unstable region.	92
5.4	Unstable modes of atoms in the Mode-II crack.	93

5.5	Unstable modes of atoms in the uniaxially stretched void.	94
5.6	Unstable modes of atoms in the biaxially stretched void.	95
5.7	Perfect carbon nanotubes (10,10) and (17,0) were stretched axially. The deformed states in equilibrium were calculated by the molecular mechanics method. Atomic acoustic tensor $\bar{\mathbf{Q}}_a(\mathbf{n})$ and its smallest eigenvalue were obtained and depicted: the darkest circles represents unstable sites. Nanotubes showed uniform deformation in a long period till critical strains, 27% and 18% for armchair and zigzag type respectively, which are very close to the prediction in reference by Dumitrica et al. As characterized by $\bar{\mathbf{Q}}_a$, instability arrives quickly after critical strains.	96
5.8	the Stone-Wales defect in carbon nanotubes.	97
5.9	Microcrack in carbon nanotubes.	97
5.10	A non-reconstructed vacancy in carbon nanotubes.	98
5.11	Evolution of unstable zone in the (17,0) tube with symmetric one-atom vacancy (upper row) and two-atom vacancy (lower row).	98
5.12	Strain-stress curves of pristine and defective CNTs.	99
6.1	Propagation of a mode-I crack determined by local instability condition.	117
6.2	Propagation of a mode-II crack determined by local instability condition.	118
6.3	Propagation of a mixed mode crack determined by local instability condition.	119
6.4	Propagation of a mode-I crack determined by combining the local instability condition and the cutoff condition.	120
6.5	Development of Stone-Wales defect in armchair carbon nanotube. . . .	121
6.6	Development of Stone-Wales defect in zigzag carbon nanotube.	122
6.7	Development of reconstructed vacancy with one atom missing in zigzag carbon nanotube.	123
6.8	Development of reconstructed vacancy with two atoms missing in zigzag carbon nanotube.	123

6.9	Development of type-I reconstructed vacancy with one atom missing in armchair carbon nanotube.	124
6.10	Development of type-II reconstructed vacancy with one atom missing in armchair carbon nanotube.	125
7.1	Schematics of the method. (a) The grey dots represent the atoms of the local cluster D and the black dots represent pristine atoms. The interface is marked by the layer of dashed hexagon rings. (b) The deformed local region with the atom positioned at $\mathbf{r}^{(1)}$; (c) The defective replica \hat{D} , whose boundary is fixed but the interior atoms are allowed to relax.	143
7.2	Illustration of the defective patches. (a) and (b) The layer models for large diameter tubes; (c) and (d) The ring models for small diameter tubes.	144
7.3	Comparative formation energies versus stretch	145
7.4	Slender tubes (12nm) used in the computation. (a) (5,5) armchair; (b) (10,0) zigzag.	146
7.5	The distribution of formation energy in the uniformly stretched nanotube.	146
7.6	Four bended configurations of the (5,5) carbon nanotube.	147
7.7	The distribution of formation energy on bended (5,5) nanotubes. The curves (a) through (d) correspond to the configurations in Figure 7.6.	147
7.8	Relatively positioned multiple defects.	148
7.9	Formation energy of a second SW defect. The cases (a) through (f) correspond to the relative positions illustrated in Figure 7.8.	148

LIST OF SYMBOLS

Symbols

Ω_0	Material body in the reference configuration
Ω	Material body in the current configuration
χ	Motion mapping
\mathbf{X}	Position in the reference configuration
\mathbf{x}	Position in the current configuration
\mathbf{u}	Displacement
\mathbf{F}	Deformation gradient
\mathbf{E}	Green-Lagrangian strain
\mathbf{P}	First Piola-Kirchhoff stress
\mathbf{S}	Second Piola-Kirchhoff stress
$\boldsymbol{\sigma}$	Cauchy stress
W	Strain energy density function
\mathbb{D}	Reference material tangent moduli
\mathbb{C}	Current material tangent moduli
\mathbb{B}	Moduli in B-criterion
\mathcal{A}	Elasticity tensor
\mathbf{b}	Body force
\mathbf{t}	Traction force
E_a	Energy of atom a
E	Internal strain energy of the body

P	External work
∇_0	Gradient operator in the reference configuration
∇	Gradient operator in the current configuration
Π	Total energy in macroscopic systems
π	Total energy in atomic systems
Δ	Incremental symbol
δ	Variational symbol
\mathbf{Q}	Continuum acoustic tensor
\mathbf{Q}_a	Atomic acoustic tensor
\mathbf{r}_i	Position of atom i
\mathbf{r}_{ij}	Atomic vector from atom i to j
$\boldsymbol{\tau}_a$	Atomic stress
\mathbf{t}_a	Atomic traction
\mathbf{f}_{ab}	Atomic force between atom a and b
\mathbf{f}_i	External force acting on atom i
ω_a	Atomic volume
\mathbf{N}	Lagrangian vector
\mathbf{m}, \mathbf{n}	Eulerian vectors
V	Interatomic potential
ε_{crit}	Critical engineering strain
\mathbf{R}_{ij}	Undeformed atomic vector
\mathbf{R}_i	Undeformed atom position

\mathbf{A}	Undeformed lattice vector
\mathbf{a}	Deformed lattice vector
$\mathbf{T}^{(p)}$	Referential translation vector of p th atom in the unit cell
$\mathbf{t}^{(p)}$	Referential translation vector of p th atom in the unit cell
λ	Principal stretch
γ	Shear ratio
$\boldsymbol{\eta}$	Internal shift vector
θ	Current angle
Θ	Reference angle
θ_{ij}	Angle between renumbered atom bond i and j
B	Many-body coupled function
$\bar{\theta}_{abj}$	Angle between non-renumbered atom bond ba and bj
Θ_{kijl}	Dihedral angle between non-renumbered atom bond ik and jl
V_R	Repulsive potential
V_A	Attractive potential
r_i	Renumber bond length
r_{ab}	Non-renumbered bond length
\mathbf{I}	Second order identity tensor
ρ, ρ_0	Mass per unit current, reference volume
δ_{ij}	Kronecker delta function ($1 : i = j$ and $0 : i \neq j$)
$\bar{\rho}_i$	Electron density hosted at atom i
\mathbb{K}	Global stiffness matrix in atomistic FEM

\mathbf{K}_e	Elemental stiffness matrix in atomistic FEM
E_f	Formation energy
\mathbb{C}_{rs}	Compliance matrix associated with the interface atoms

CHAPTER 1 OVERVIEW

1.1 Motivation and objectives

The last few years have witnessed significant advances in nanotechnologies. Recently, nanoscale materials such as carbon nanotubes (CNTs) have been synthesized. The machines and devices of dimension at the molecular level have also been under development. The failure mechanism of a body at the nanometer scale is important for understanding the mechanical behavior of nanoscale materials and structures, the research of which provides a necessary foundation for the advance of this field.

The stability of an elastic body is a well developed subject. In continuum mechanics, there are a number of treatises devoted specifically to this topic [1, 2, 3, 4, 5]. Most of existing theories are for analyzing the stability of macroscopic bodies. In physics, there are classic methods such as Crystal Elasticity and Lattice Dynamics [6, 7] that analyze the stability of a material element in the pristine crystal. Also, many relevant contributions [6, 8, 9, 10, 11, 12, 13, 14, 15, 16, 17, 18] have been devoted to investigating the intrinsic stability and ideal strength of the material. Most of them are based on the assumption of “perfect” crystals and “homogeneous” deformation, and thus boil down essentially to the continuum stability theory.

There are two major limitations in these theories. First, in some of them, the stability merely related to material behaviors has not been clearly identified.

The instability may be induced either by structural features such as the shape and size of the structure, or by unstable material responses. The former is often called *structural instability*, like elastic buckling, and usually relates to the global response the whole structure; the later is named *material instability* that leads to material failure and may occur in a localized region. However, material instability cannot be identified in many theories. For example, the stability criteria of [11, 12, 13, 14, 15] were derived under the assumption that the material body is subject to stress boundary conditions. Hence, the unstable modes predicted therein may not be kinematically admissible and cannot be observed if the boundary of the body is all constrained. Essentially, these criteria do not completely eliminate the contribution of the external loading mechanism which can influence the stability of the whole system, thus they cannot exactly predict material failures.

Second, in the microscopic view, any matter is essentially composed of discrete atoms or molecules. The material responses determined by the interaction between atoms can be described at different length scales. Classic continuum theories assume the material to be homogeneous. For this reason, applying models [11, 12, 13, 16, 17, 18] based on the homogeneous assumption to defective systems are limited. Currently, investigating the behaviors of nano-materials in the presence of defects is of great practical interest. Defects may seriously affect the mechanical function of nano-materials. Up to now, however, there is no unified approach [19, 15, 20, 21, 22, 23] to analyze the material stability of nanoscale structures with defects or underlying highly distorted deformation.

Crack growth and fracture also relate to instabilities. At continuum scale,

linear elasticity theory is employed to describe the deformation of a cracked body, and energy-based criteria are often utilized to capture crack growth. Bond breaking essentially can be considered as material failure taking place at a small region near crack tips. In terms of stability, crack growth is the result of local instability, and then, fracture can be attributed to the loss of global stability. Continuum level fracture theories have rarely been developed from the perspective of stability. In addition, due to the discreteness of an atomic system, classic fracture theories cannot be directly applied at such a small scale. In this regard, a connection between fracture and atomic instabilities merits investigation.

Besides fracture, the rearrangement of bond structures is another natural way for a lattice adapting to excessive loads. The Stone-Wales (SW) defect, a pentagon-heptagon ring embedded in the hexagonal structure of carbon nanotubes, is the topological defect encountered when subject to large tensile strain. Energetic analysis is often performed to investigate the thermodynamics stability of the defective system. The condition for defect nucleation can also be recast in the framework of thermodynamical stability, as a first order condition like Griffith's energy criterion for crack growth.

Motivated by the needs for atomistic stability analysis, we propose to examine the theoretical foundation of material stability at the nanoscale and to investigate the connection of stability to fracture and defect motions. Specifically, we will (1) examine existing theories of material stability as they apply to atomic systems, (2) analyze the localized failure observed in carbon nanotubes, (3) develop the atomistic material stability criterion that is suitable for nanometer scale

atomic structures (either perfect or defective), and thus lay down the microscopic foundation of material stability of macroscopic continuum solids, (4) apply the atomic material stability theory in atomic scale fracture propagation, and (5) to develop a method for computing the formation energy of Stone-Wales defects in deformed CNTs.

1.2 Organization

To approach these goals, the thesis is organized as follows. Chapter 2 provides a critical review of existing theories of elastic stability. A unified framework of energy based stability theory is presented. A stable equilibrium state corresponds to a local minimum of the total potential energy of the system. In general, the total energy consists of contributions from the internal strain energy and the external work. In the unified framework, the role of the external work is emphasized. Existing methods for crystal stability are categorized into several cases according to the type of boundary conditions. Based on the critical review of classical stability theories, the condition corresponding to material stability is identified.

In Chapter 3, the material stability of pristine carbon nanotubes is investigated at the continuum level by using the crystal elasticity theory. A homogenized continuum model based on the extended Cauchy-Born rule is adopted. The material stability of carbon nanotubes under tension, compression, and torsion are studied. It has been reported that the loss of stability of stretched and compressed CNTs is manifested as localized necking and collapse. In this chapter, these phenomena are captured by material instability and thus lead the way to a fully atomic

level material stability study in the sequel.

In Chapter 4, an atomistic finite element method (FEM) is proposed. Based on the principle of virtual work, the atomistic FEM has a similar code structure to the continuum FEM and can be embedded into existing FEM packages. The advantage of this atomistic FEM is that constructing FEM for atomic systems is systematic and normalized. A same element module can be utilized for different materials described by the same type of interatomic potential, differing only in material modules. Based on the bond order many-body Tersoff-Brenner potentials [24, 25], a new 6-node atomic element is designed for analyzing carbon nanotubes. Different from the other atomic level FEM models, the present 6-node element for CNTs can be conveniently extended for considering bond-torsion effects. The first and second generation Brenner potentials [24, 25] can be incorporated into this 6-node element.

An atomic level material stability theory is developed in Chapter 5. The material stability of an atomic system is described by the energy landscape at the atomic site. An “atomic acoustic tensor” is derived, the singularity of which is used as an indicator of local instability of the atomic structure. The atomic material stability theory is shown to be the atomistic counterpart of the continuum material stability theory in nonlinear elasticity. In the proposed approach, the stability of an atomic site is intrinsically determined by the property of the atomic energy function, and no continuum stability concepts are involved. Therefore, it is believed that the criterion is applicable in defective nanoscale systems provided that the site energy can be reasonably defined. To test for the validity, this stability theory

is applied to defective simple crystals and defective carbon nanotubes.

In Chapter 6, the atomic material stability theory is combined with atomistic simulation to gain understanding on crack propagation and fracture as they relate to instabilities of bond structures. The atomic acoustic tensor is used as the indicator to detect the local instability at the crack tip, and then to decide bond breaking. Quasi-static crack growth till fracture, i.e. the passage from local instability to global instability, is simulated by the atomistic FEM. Special emphasis is placed on the evaluation of an early conjecture made by Barenblatt [26] who assumed that a crack tip possesses an invariant shape which is maintained by the balance of applied stress and cohesive forces. Combining the bond breaking criteria of atomic instability and cutoff distance, the cohesive zone near the crack tip and the location of crack tip can be clearly observed. Thus, this work provided some simulation-based justification for Barenblatt's fracture theory.

The nucleation and evolution of topological defects are pathways to release excessive strain energy prior to material failure. The tendency of defect nucleation is often predicted by the energy variation during defect formation. In Chapter 7, an approximate method is presented for calculating the formation energy of Stone-Wales defect in deformed carbon nanotubes. A formula is derived to show that the structural energy variation consists of the change of local atomic potential due to bond reconfiguration in the defective region and a higher order correction that represents the influence of the remaining system. The advantages lie in the computational efficiency. The optimization of the global configuration of defective nanotubes can be eliminated. The method is utilized to investigate the formation

energy map in non-uniformly deforming nanotubes and to study the energetic interaction between multiple defects.

1.3 Contributions

The contributions of the present work include:

1. Proposed a theoretical framework of stability analysis for nanoscale structures.
2. Analyzed the localized failure of carbon nanotubes from the stand point of material stability.
3. Created a new 6-node atomic element for CNTs by the unified atomistic finite element method.
4. Developed an atomic level material stability theory and studied the local instability of defective nanoscale structures.
5. Applied the atomic stability theory and atomistic FEM in simulating the quasi-static crack growth and fracture in atomic systems.
6. Presented an approximate method for calculating the formation energy of Stone-Wales defects in CNTs.

CHAPTER 2 BACKGROUND – STABILITY THEORY OF ELASTIC SOLIDS

2.1 Elements of nonlinear elasticity

In this section, the fundamentals of nonlinear elasticity are briefly introduced. The full scale exposition of this subject can be found in the classic textbook by Ogden [3].

2.1.1 Kinematics and strain

In classic continuum mechanics, one is concerned with the motion of a body consisting of continuously distributed materials. Let Ω_0 be the region occupied by the material body in the reference configuration. The material point is identified by its position \mathbf{X} in Ω_0 . Let $\chi : \mathbb{R}^3 \rightarrow \mathbb{R}^3$ be the motion that brings the material point \mathbf{X} to its deformed position \mathbf{x} in the current configuration Ω at time t ,

$$\mathbf{x} = \chi(\mathbf{X}; t). \quad (2.1)$$

The deformation of the body is determined by the static displacement. The deformation gradient is defined as

$$\mathbf{F} = \frac{\partial \chi}{\partial \mathbf{X}}, \quad d\mathbf{x} = \mathbf{F}d\mathbf{X}, \quad (2.2)$$

where $d\mathbf{x}$ and $d\mathbf{X}$ are material vectors in the current and reference configuration respectively. The stretch of the material line at position \mathbf{X} is measured by

$$\frac{(ds)^2 - (dS)^2}{(dS)^2} = \mathbf{N} \cdot (\mathbf{F}^T \mathbf{F} - \mathbf{I})\mathbf{N}, \quad (2.3)$$

where $d\mathbf{X} = dS\mathbf{N}$ and \mathbf{N} is the unit vector denoting the direction of the material line, $(ds)^2 = d\mathbf{x} \cdot d\mathbf{x}$. The Green-Lagrangian strain at \mathbf{X} is defined as

$$\mathbf{E} = \frac{1}{2}(\mathbf{F}^T\mathbf{F} - \mathbf{I}), \quad (2.4)$$

where \mathbf{I} is the second order identity tensor.

2.1.2 Stress and constitutive law

In the thesis, it is assumed that the material body is hyperelastic, namely there is an elastic potential energy function W which represents the stored energy density per unit reference volume. W locally depends on the deformation gradient at the material point \mathbf{X} . Writing $W = W(\mathbf{F})$, the first Piola-Kirchhoff (P-K) stress is defined as

$$\mathbf{P} = \frac{\partial W}{\partial \mathbf{F}}. \quad (2.5)$$

The Cauchy stress is related to \mathbf{P} by

$$\boldsymbol{\sigma} = J^{-1}\mathbf{P}\mathbf{F}^T, \quad (2.6)$$

where $J = \det\mathbf{F}$ is the volume ratio. The second Piola-Kirchhoff stress is a non-physical quantity which is obtained by projecting the nominal stress back to the reference configuration, i.e.,

$$\mathbf{S} = \mathbf{F}^{-1}\mathbf{P}. \quad (2.7)$$

Therefore, the Cauchy stress and the 2nd P-K stress has relation as $\boldsymbol{\sigma} = J^{-1}\mathbf{F}\mathbf{S}\mathbf{F}^T$.

By the invariance under superposed rigid body motion, the strain energy function is written as $W = \widehat{W}(\mathbf{E})$, and the 2nd P-K stress can be computed from the energy

density as

$$\mathbf{S} = \frac{\partial \widehat{W}}{\partial \mathbf{E}}. \quad (2.8)$$

The referential tangent moduli of the material is

$$\mathbb{D} = \frac{\partial^2 W}{\partial \mathbf{E} \partial \mathbf{E}}. \quad (2.9)$$

The elasticity tensor is defined as

$$\mathcal{A} = \frac{\partial^2 W}{\partial \mathbf{F} \partial \mathbf{F}}. \quad (2.10)$$

Notice that $\mathbf{P} = \mathbf{F} \frac{\partial W}{\partial \mathbf{E}}$. Use the chain rule, it follows that

$$\mathcal{A}_{i\alpha j\beta} = \mathbb{D}_{\lambda\alpha\mu\beta} F_{i\lambda} F_{j\mu} + S_{\alpha\beta} \delta_{ij}, \quad (2.11)$$

2.1.3 Balance of linear momentum

The balance of linear momentum is written as

$$\frac{d}{dt} \int_{\mathcal{P}} \rho \mathbf{v} \, dv = \int_{\mathcal{P}} \rho \mathbf{b} \, dv + \int_{\partial \mathcal{P}} \mathbf{t} \, da, \quad (2.12)$$

where \mathcal{P} denotes any subregion of body Ω , and $\frac{d}{dt}$ represents material derivative, \mathbf{v} is the velocity, ρ stands for the mass per unit current volume, \mathbf{b} is the body forces, and \mathbf{t} is the traction force on the surface of region \mathcal{P} whose normal is \mathbf{n} . By using the relation of stress and traction i.e. $\boldsymbol{\sigma} = \mathbf{t}\mathbf{n}$ and the divergence theorem, one can convert the surface integral into volume integral and obtain the local form of equation of motion

$$\rho \mathbf{b} + \nabla \cdot \boldsymbol{\sigma} = \rho \dot{\mathbf{v}}, \quad (2.13)$$

in the current configuration, and

$$\rho_0 \mathbf{b} + \nabla_0 \cdot \mathbf{P} = \rho_0 \dot{\mathbf{v}}, \quad (2.14)$$

in the reference configuration, in which the mass per unit reference volume $\rho_0 = J\rho$, “ $\nabla \cdot []$ ” and “ $\nabla_0 \cdot []$ ” denote the divergence operator in the current and reference configuration respectively.

2.2 A unified approach of stability analysis

The mechanical elastic stability of an equilibrium configuration is considered in this thesis. A material body is said to be stable at an equilibrium state if the increase of the strain energy under any admissible configurational perturbation exceeds the work done by external forces [3]. Practically, the perturbation is assumed to be small, and hence the stability so concerned is called infinitesimal (linearized) stability. Clearly, an infinitesimally stable equilibrium configuration corresponds to a local minimum of the total potential energy of the system.

In continuum mechanics, the infinitesimal stability is often related to uniqueness of solution of a boundary value problem (BVP). In fact, the boundary condition (BC) plays an important role in the stability of the body. In general, the total potential energy has contributions from both the internal stored energy and the external work supplied by the loading mechanism. The stability of the system is decided by the competition between the change of these two. Instability can be induced by either unstable material responses or non-material features such as the geometry of the body and boundary conditions. The merely constitutive-related instability is called material stability; the instability related to geometries and BC is called structural instability. The results on elastic stability have been scattered in literature [6, 2, 8, 9, 11, 13]. In what follows stability criteria of an elastic body

subject to different loading mechanisms will be summarized. Based on a critical review on various criteria, the material stability condition is identified.

The stability of an elastic body at equilibrium requires that the increase in the strain energy in any real or virtual incremental displacement exceeds the mechanical work done by the applied loadings [2, 3], i.e.,

$$\Delta E > \Delta P, \quad (2.15)$$

where E is the strain energy, P is the external work, and “ Δ ” stands for the change of the quantity from the one configuration to another. If the body is stable, any perturbed configuration is energetically unfavorable. In a purely mechanical system, the strain energy in a finitely deformed body is

$$E = \int_{\Omega_0} W(\mathbf{F}; \mathbf{X}) dV. \quad (2.16)$$

The external work P is in general a function of displacements \mathbf{u} , body forces \mathbf{b} and surface traction \mathbf{t} . If the external forces are conservative, one can define an external potential as

$$P = P(\mathbf{b}, \mathbf{t}, \mathbf{u}). \quad (2.17)$$

The total potential energy of the system (including elastic body and loading mechanism) is defined as the strain energy minus the external potential,

$$\Pi(\mathbf{F}, \mathbf{u}; \mathbf{X}) = E - P. \quad (2.18)$$

If the external forces are not conservative, one can write the work increment by

$$\Delta P(\mathbf{b}, \mathbf{t}, \mathbf{u}, \Delta \mathbf{u}),$$

and the incremental total energy can be written as

$$\Delta\Pi(\mathbf{F}, \mathbf{u}; \mathbf{X}) = \Delta E - \Delta P. \quad (2.19)$$

Therefore, in either case, the stability condition (2.15) of an equilibrium configuration χ can be stated as

$$\Delta\Pi(\chi) > 0 \quad (2.20)$$

for any kinematically admissible perturbation $\Delta\mathbf{u}$ from this configuration. Practically, the virtual displacement is supposed to be small. At the aid of variation calculus, we expand the energy increment as

$$\Delta\Pi = \delta\Pi + \frac{1}{2!}\delta^2\Pi + \frac{1}{3!}\delta^3\Pi + \dots \quad (2.21)$$

Since the configuration χ is equilibrium, $\delta\Pi = 0$ for any $\delta\mathbf{u}$. Now, for stability, one needs to evaluate the next leading term $\delta^2\Pi$. The stability condition (2.20) can be rewritten as

$$\delta^2\Pi > 0 \quad (2.22)$$

for any infinitesimal perturbation $\delta\mathbf{u}$. If $\delta^2\Pi = 0$, the stability will be determined by the sign of the next even order term $\delta^4\Pi$, and so on.

2.2.1 Stability under dead loads

Consider an elastic material body subject to mixed boundary conditions and assume the traction forces are dead loads [3], i.e. constant under perturbations. This case is usually applied in bifurcation analysis, see references [10, 3]. Then, the external potential P is

$$P = \int_{\Omega_0} \rho_0 \mathbf{b} \cdot \mathbf{u} \, dV + \int_{\partial\Omega_0^t} \bar{\mathbf{t}} \cdot \mathbf{u} \, dA, \quad (2.23)$$

where “ (\cdot) ” stands for inner product, $\bar{\mathbf{t}}$ is the constant surface traction, $\partial\Omega_0$ represents the boundary, and $\partial\Omega_0^{\mathbf{t}}$ denotes the traction boundary. The total potential energy of the system is

$$\Pi = \int_{\Omega_0} W(\mathbf{F}; \mathbf{X}) dV - \int_{\Omega_0} \rho_0 \mathbf{b} \cdot \mathbf{u} dV - \int_{\partial\Omega_0^{\mathbf{t}}} \bar{\mathbf{t}} \cdot \mathbf{u} dA. \quad (2.24)$$

The variation due to a virtual displacement $\delta\mathbf{u}$ gives

$$\delta\Pi = \int_{\Omega_0} \mathbf{P} \cdot \delta\mathbf{F} dV - \int_{\Omega_0} \rho_0 \mathbf{b} \cdot \delta\mathbf{u} dV - \int_{\partial\Omega_0^{\mathbf{t}}} \bar{\mathbf{t}} \cdot \delta\mathbf{u} dA. \quad (2.25)$$

According to the divergence theorem,

$$\int_{\Omega_0} \mathbf{P} \cdot (\nabla_0 \delta\mathbf{u}) dA = - \int_{\Omega_0} (\nabla_0 \cdot \mathbf{P}) \cdot \delta\mathbf{u} dV + \int_{\partial\Omega_0^{\mathbf{t}}} \mathbf{P}\mathbf{N} \cdot \delta\mathbf{u} dA,$$

the first variation of the potential energy

$$\delta\Pi = - \int_{\Omega_0} (\nabla_0 \cdot \mathbf{P} + \rho_0 \mathbf{b}) \cdot \delta\mathbf{u} dV + \int_{\partial\Omega_0^{\mathbf{t}}} (\mathbf{P}\mathbf{N} - \bar{\mathbf{t}}) \cdot \delta\mathbf{u} dA, \quad (2.26)$$

vanishes in the light of the balance law $\nabla_0 \cdot \mathbf{P} + \rho_0 \mathbf{b} = 0$ and boundary condition $\mathbf{P}\mathbf{N} = \bar{\mathbf{t}}$.

Following the first variation (2.25), given that the body force and surface traction are constant and $\delta(\delta\mathbf{u}) = 0$, the second variation $\delta^2\Pi = \delta(\delta\Pi)$ becomes

$$\begin{aligned} \delta^2\Pi &= \int_{\Omega_0} \delta\mathbf{P} \cdot \delta\mathbf{F} dV = \int_{\Omega_0} (\delta\mathbf{F}\mathbf{S} + \mathbf{F}\delta\mathbf{S})\delta\mathbf{F} dV \\ &= \int_{\Omega_0} \delta\mathbf{F} \cdot (\mathbf{F}\mathbb{D}\mathbf{F}^T + \mathbf{1} \boxtimes \mathbf{S})\delta\mathbf{F} dV, \\ &= \int_{\Omega} \nabla\delta\mathbf{u} \cdot (\mathbb{C} + \mathbf{1} \boxtimes \boldsymbol{\sigma})\nabla\delta\mathbf{u} dv, \end{aligned} \quad (2.27)$$

where \mathbb{C} is the push-forward of material tangent $\mathbb{D} \mathbb{C} = \frac{1}{J} \mathbf{F}\mathbf{F}\mathbb{D}\mathbf{F}^T\mathbf{F}^T$, and “ \boxtimes ” is the Kronecker product that is defined by the multiplication $(\mathbf{U} \boxtimes \mathbf{V})\mathbf{u} \otimes \mathbf{v} =$

$\mathbf{U}\mathbf{u} \otimes \mathbf{V}\mathbf{v}$. The stability condition (2.22) requires $\delta^2\Pi$ to be positive, which gives

$$\int_{\Omega_0} \delta\mathbf{F} \cdot (\mathbf{F}\mathbb{D}\mathbf{F}^T + \mathbf{1} \boxtimes \mathbf{S})\delta\mathbf{F} \, dV > 0, \quad \forall \delta\mathbf{F} \neq 0 \quad (2.28)$$

in the reference configuration, or,

$$\int_{\Omega} \nabla\delta\mathbf{u} \cdot (\mathbb{C} + \mathbf{1} \boxtimes \boldsymbol{\sigma})\nabla\delta\mathbf{u} \, dv > 0, \quad \forall \delta\mathbf{u} \neq 0, \quad (2.29)$$

in the current configuration. In deriving inequality (2.28) and (2.29), the relation $\nabla\delta\mathbf{u} = \delta\mathbf{F}\mathbf{F}^{-1}$ is used. The corresponding local forms of stability criteria are that the elasticity tensor

$$\mathcal{A}_{i\alpha j\beta} = \mathbb{D}_{\lambda\alpha\mu\beta} F_{i\lambda} F_{j\mu} + S_{\alpha\beta} \delta_{ij} \quad (2.30)$$

or its Eulerian counterpart

$$A_{ikjl} = \mathbb{C}_{ikjl} + \sigma_{kl} \delta_{ij} \quad (2.31)$$

is positive definite. Apparently, satisfying the local condition at each point is sufficient for the body being stable (the underlying deformation can be either uniform or non-uniform). Nonetheless, the converse may not be true. Only when the material is homogeneous, the underlying deformation is uniform (perturbations are also uniform), and the body is subject to all round dead load, the global stability criteria (2.28) and (2.29) are equivalent to the local one.

2.2.2 Stability with controlled Cauchy stress

In this section, a different case is studied in which the body is subject all round traction boundary condition and the Cauchy stress on the boundary is assumed unaltered under perturbations. This condition has been discussed in references [27, 11, 12, 13]. The stability criterion has been used in literature [14, 15].

To fulfill this condition, the traction forces on the boundary may be subjected to change. Therefore, the work done by the traction cannot be written as a linear function of the boundary displacement. However, it can be shown [3] that an equivalent energy functional can be obtained by combining the stored energy and a surface potential that only depends on configurations. Since the current configuration is equilibrium, one can state the first variation of the potential energy vanishes in accordance with the principle of virtual work

$$\delta\Pi = \int_{\Omega} \boldsymbol{\sigma} \cdot \nabla^s \delta \mathbf{u} \, dv - \int_{\partial\Omega} \bar{\boldsymbol{\sigma}} \mathbf{n} \cdot \delta \mathbf{u} \, da = 0. \quad (2.32)$$

Here $\bar{\boldsymbol{\sigma}}$ is the constant Cauchy stress. Applying the divergence theorem to the domain integral gives

$$\int_{\Omega} \boldsymbol{\sigma} \cdot \nabla^s \delta \mathbf{u} \, dv = \int_{\partial\Omega} \boldsymbol{\sigma} \mathbf{n} \cdot \delta \mathbf{u} \, da - \int_{\Omega} (\nabla \cdot \boldsymbol{\sigma}) \cdot \delta \mathbf{u} \, dv.$$

Then, one arrives at

$$\delta\Pi = \int_{\partial\Omega} (\boldsymbol{\sigma} - \bar{\boldsymbol{\sigma}}) \mathbf{n} \cdot \delta \mathbf{u} \, da - \int_{\Omega} (\nabla \cdot \boldsymbol{\sigma}) \cdot \delta \mathbf{u} \, dv = 0. \quad (2.33)$$

Since the variation is arbitrary, one concludes $\boldsymbol{\sigma} = \bar{\boldsymbol{\sigma}}$ on the boundary and the local balance law $\nabla \cdot \boldsymbol{\sigma} = 0$.

To compute the second variation, first rewrite Eq. (2.32) in the reference configuration as

$$\delta\Pi = \int_{\Omega_0} \mathbf{P} \cdot \delta \mathbf{F} \, dV - \int_{\Omega_0} J \bar{\boldsymbol{\sigma}} \cdot \nabla \delta \mathbf{u} \, dV, \quad (2.34)$$

the second variation is computed as follows

$$\begin{aligned}
\delta^2\Pi &= \int_{\Omega_0} \delta\mathbf{P} \cdot \delta\mathbf{F} \, dV - \int_{\Omega_0} (\delta J \bar{\boldsymbol{\sigma}} \cdot \delta\mathbf{F}\mathbf{F}^{-1} + J \bar{\boldsymbol{\sigma}} \cdot \delta\mathbf{F}\delta\mathbf{F}^{-1}) \, dV \\
&= \int_{\Omega_0} \delta\mathbf{F} \cdot (\mathbf{1} \boxtimes \mathbf{S} + \mathbf{F}\mathbb{D}\mathbf{F}^T) \delta\mathbf{F} \, dV \\
&\quad - \int_{\Omega_0} [J(\mathbf{1} \cdot \nabla\delta\mathbf{u})(\bar{\boldsymbol{\sigma}} \cdot \nabla\delta\mathbf{u}) - J\bar{\boldsymbol{\sigma}} \cdot \nabla\delta\mathbf{u}\nabla\delta\mathbf{u}] \, dV \\
&= \int_{\Omega} \delta u_{i,j} \underbrace{[\mathbb{C}_{ijkl} - \delta_{kl}\sigma_{ij} + \delta_{ik}\sigma_{jl} + \delta_{il}\sigma_{kj}]}_{\mathbb{B}} \delta u_{k,l}
\end{aligned}$$

in which conditions such as

$$\delta J = J\mathbf{F}^{-T} \cdot \delta\mathbf{F},$$

$$\delta\mathbf{F} = \nabla\delta\mathbf{u}\mathbf{F},$$

constant $\bar{\boldsymbol{\sigma}}$, homogeneous $\boldsymbol{\sigma}$, $\boldsymbol{\sigma} = \bar{\boldsymbol{\sigma}}$ on $\partial\Omega$, $\nabla \cdot \boldsymbol{\sigma} = 0$, and $\delta(\nabla \cdot \boldsymbol{\sigma}) = 0$ are used.

If one restricts to the case that $\nabla\delta\mathbf{u}$ is an incremented strain (i.e., not rotation), then, the \mathbb{B} tensor in the integral can be replaced by its symmetrized counterpart

$$\mathbb{B}_{ijkl}^s = \mathbb{C}_{ijkl} + (1/2)(\delta_{ik}\sigma_{jl} + \delta_{jk}\sigma_{il} + \delta_{jl}\sigma_{ik} + \delta_{il}\sigma_{jk} - 2\delta_{kl}\sigma_{ij}). \quad (2.35)$$

\mathbb{B}^s has been used as B -criterion in [27, 11, 12, 13] that demands \mathbb{B}_{ijkl}^s is positive definite. The difference between \mathbb{B} and \mathbb{B}^s is that, \mathbb{B}^s has the minor symmetry $\mathbb{B}_{ijkl}^s = \mathbb{B}_{jikl}^s = \mathbb{B}_{ijlk}^s$ while \mathbb{B} does not.

2.2.3 Stability with controlled 2nd P-K stress

In this section, the stability condition with 2nd P-K stress being fixed on all the boundary is discussed. In practice, it is very difficult to control 2nd P-K stress (so is controlling Cauchy stress). However, this result has pedagogic values because it sheds light into the nature of the classic stability criterion of Born [6].

In this case, the virtual work principle gives

$$\delta\Pi = \int_{\Omega_0} \mathbf{P} \cdot \delta\mathbf{F} \, dV - \int_{\partial\Omega_0} \mathbf{F}\bar{\mathbf{S}}\mathbf{N} \cdot \delta\mathbf{u} \, dA = 0. \quad (2.36)$$

Applying the divergence theorem to the domain integral gives

$$\int_{\Omega_0} \mathbf{F}(\mathbf{S} - \bar{\mathbf{S}})\mathbf{N} \cdot \delta\mathbf{F} \, dV - \int_{\Omega_0} (\nabla_0 \cdot (\mathbf{F}\bar{\mathbf{S}})) \cdot \delta\mathbf{u} \, dV = 0, \quad (2.37)$$

where $\mathbf{P} = \mathbf{F}\mathbf{S}$ is applied. Since the variation is arbitrary, the balance of internal stress and external stress $\mathbf{S} = \bar{\mathbf{S}}$ and the local balance law $\nabla_0 \cdot (\mathbf{F}\bar{\mathbf{S}}) = 0$ are obvious.

Still assume the deformation and stress are always uniform. Rewrite (2.36)

as

$$\delta\Pi = \int_{\Omega_0} \mathbf{P} \cdot \delta\mathbf{F} \, dV - \int_{\Omega_0} [\nabla_0 \cdot (\mathbf{F}\bar{\mathbf{S}}) \cdot \delta\mathbf{u} + \mathbf{F}\bar{\mathbf{S}} \cdot \delta\mathbf{F}] \, dV. \quad (2.38)$$

Now, everything is written in the reference configuration. The second variation as

$$\begin{aligned} \delta^2\Pi &= \int_{\Omega_0} \delta\mathbf{P} \cdot \delta\mathbf{F} \, dV - \int_{\Omega_0} \delta(\nabla_0 \cdot (\mathbf{F}\bar{\mathbf{S}})) \cdot \delta\mathbf{u} \, dV - \int_{\Omega_0} \delta\mathbf{F}\bar{\mathbf{S}} \cdot \delta\mathbf{F} \, dV \quad (2.39) \\ &= \int_{\Omega_0} \delta\mathbf{E} \cdot [\mathbb{D}]\delta\mathbf{E} \, dV \\ &= \int_{\Omega} \nabla^s \delta\mathbf{u} \cdot [\mathbb{C}]\nabla^s \delta\mathbf{u} \, dv, \end{aligned}$$

where the incremental balance law $\nabla_0 \cdot (\delta\mathbf{P}) = 0$ is used. The local stability condition in this case is that \mathbb{D} is positive definite, which is the Born's stability criteria in [6].

2.2.4 Stability with all fixed displacement boundaries

If all the displacements on the boundary are fixed, the total potential energy of the system would become

$$\Pi = \int_{\Omega_0} W(\mathbf{F}; \mathbf{X}) dV \quad (2.40)$$

The variation due to a virtual displacement gives

$$\delta\Pi = \int_{\Omega_0} \mathbf{P} \cdot \delta\mathbf{F} dV = - \int_{\Omega_0} (\nabla_0 \cdot \mathbf{P}) \cdot \delta\mathbf{u} dV + \int_{\partial\Omega_0} (\mathbf{P}\mathbf{N}) \cdot \delta\mathbf{u} dV. \quad (2.41)$$

Because $\delta\mathbf{u} = 0$ on $\partial\Omega_0$, the second integral in (2.41) vanishes. Then, the principle of stationary potential energy still holds $\delta\Pi = 0$, since the balance law makes $\nabla_0 \cdot \mathbf{P} = 0$. For stability

$$\delta^2\Pi = \int_{\Omega_0} \delta\mathbf{F} \cdot \mathcal{A}\delta\mathbf{F} dV > 0 \quad (2.42)$$

must hold for any $\delta\mathbf{F} \neq 0$. The corresponding local form is

$$\delta\mathbf{F} \cdot \mathcal{A}\delta\mathbf{F} > 0, \quad (\forall \delta\mathbf{F} \neq 0). \quad (2.43)$$

2.3 Material stability

The diversity of stability criteria begs the question as to: among those stability criteria under various conditions, which one is associated only with intrinsic material properties? Apparently, when the elastic body is subject to all round traction BC or mixed BC, there are non-constrained boundaries through which the influence of environment to the second variation of potential energy will be brought in. If the non-constrained boundary is loading free, there is no second order energetic contribution entering from the free boundary, on which however the

perturbation might develop divergently (e.g. large rotation could occur). Then, the body may bifurcate to another equilibrium configuration. Euler buckling is a typical example. This bifurcation definitely relates to the particular boundary condition and the geometry of the body.

Gibbs [28] defined the stability as: *the system be stable with respect to arbitrary reconfigurations that do not alter its boundaries*. From this definition, it is clear that this type of stability excludes all the external contributions and the unstable geometric modes. Therefore, it is intrinsically related to the material behavior. Under Dirichlet BC, an elastic body with homogeneous properties under uniform deformation should arrive at a unique configuration as long as the material is robust (or say the constitutive relation is well-posed). According to the celebrated theorem of Van Hove [29], for a homogeneous elastic body under uniform deformation, the strong ellipticity

$$(\mathbf{m} \otimes \mathbf{N}) \cdot \mathcal{A}(\mathbf{m} \otimes \mathbf{N}) > 0 \quad (2.44)$$

for all $\mathbf{m} \otimes \mathbf{N} \neq 0$, where \mathbf{m} is the Eulerian vector and \mathbf{N} the Lagrangian vector, is the *necessary and sufficient* condition for the the Dirichlet BVP having a unique solution and guarantees the Gibbs's stability criterion (2.42), a proof of which is recorded in Appendix A.

The sufficiency is apparent when invoking Van Hove's theorem, i.e. if strong ellipticity (2.44) is satisfied, the stability condition (2.42) holds. Conversely, for the necessity, once (2.44) is violated for some nonzero vector \mathbf{m} and \mathbf{N} , it is always possible to choose a localization zone over which the integral has sufficiently negative contribution to the total integral (2.42) such that the global condition (2.42)

fails [30, 29]. It implies that for all round constrained displacement BC (ruling out all the geometric modes), there could still exist admissible modes inducing localized failure if (2.44) were violated. This failure is merely due to unstable material responses. In contrast, the stability criteria obtained by [11, 12, 13] are not purely material since the unstable modes they detect may not be kinematically admissible in the constrained displacement case. (Notice that the necessity and sufficiency of strong ellipticity to linearized stability is only valid for the body under Dirichlet boundary conditions. Structural bifurcation, e.g. buckling, may be possible for a body under mixed BC with dead loads even though strong ellipticity holds everywhere.)

It is also known that the loss of strong ellipticity is related to the existence of weak discontinuity (strain localization) and stationary acoustical (elastic) waves. We shall discuss these implications in more detail in Chapter 3 and Chapter 5. Particularly, the strong ellipticity condition is to be applied to analyze the localized failure of carbon nanotubes. In order to study the local instability in atomic systems (pristine or defective), an atomistic counterpart of the material stability theory is to be developed.

2.4 Global stability v.s. local stability

As discussed previously, the stability of an equilibrium configuration of the elastic body is governed by the second order increment of the potential energy under perturbations. Without loss of generality, the stability criteria can be written

in a global integral form

$$\int_{\Omega_0} \mathbf{G} \cdot [\mathbb{M}] \mathbf{G} \, dV > 0, \quad (\forall \mathbf{G} \neq 0), \quad (2.45)$$

and in a local differential form

$$\mathbf{G} \cdot [\mathbb{M}] \mathbf{G} \, dV > 0, \quad (\forall \mathbf{G} \neq 0), \quad (2.46)$$

where \mathbf{G} is a second order tensor representing an incremental deformation, and \mathbb{M} is a fourth order tensor denoting the associated tangent moduli. Apparently, if the local condition (2.46) is satisfied at each point, the global condition (2.45) holds. Conversely, the global condition (2.45) implies the local condition (2.46) only when (i) the deformation is uniform, (ii) material is homogeneous, and (iii) the increment (perturbation) is also uniform. In fact, for the cases with unaltered Cauchy stress and 2nd P-K stress, we have assumed all traction BC and uniform deformation field. In these two cases, the global form and local form of stability criteria are equivalent but have to be limited to the particular cases. In general, the global condition and local condition are different. Violating the local condition (2.46) is inconclusive for the loss of global stability (violating condition (2.45)).

The local stability condition is a stronger condition, and guarantees the global counterpart if it is satisfied at each material point. However, the local condition (2.46) does not have to be satisfied everywhere for the body to be globally stable. If the deformation field is non-uniform, the local condition (2.46) fails at some discrete points in the body may not result in a global failure. In other words, if the body is non-uniformly deformed, while the global condition holds, there can be some local singularities. For example, a cracked body may still be able to

bear loads without failure. On the other hand, if the global condition (2.45) fails (due to either material instability or structural instability), there must be some locally unstable region inside the body. For a small scale structure, the passage from local to global instability therefore becomes an practically important issue. To investigate the relationship of global and local stability and distinguish local instability and global instability is an objective of the present work. We shall stress on this problem at Chapter 5 and Chapter 6.

CHAPTER 3 LOCALIZED FAILURE OF CARBON NANOTUBES

3.1 Introduction

The stability condition for a uniformly deformed body with all-round fixed displacement BC reflects the intrinsic limit of the material. If the strong ellipticity condition is satisfied, the homogeneous deformation state must be the unique solution of such a BVP and the material-related bifurcation in the body is excluded. The loss of strong ellipticity may induce strain localization and crack initiation. Since the continuum theory does not contain the atomistic description, it cannot be directly applied to nanoscale atomic structures.

Some work has been done on extending and applying the continuum material stability theory to analyze the microscopic failure mechanisms. Gao and Klein [31, 32] proposed a virtual internal bond (VIB) model and used the loss of strong ellipticity for crack initiation. Sunyk and Steinmann [33] formulated a mixed atomistic-continuum model for analyzing strain localization in simple (monoatomic) crystals. In that paper, the quasi-continuum method [34] was used to define the equivalent strain energy density. Sunyk and Steinmann utilized a pairwise Lennard-Jones potential that can be treated as a function of deformation gradient by making use of Cauchy-Born rule. In this chapter, by using the crystal elasticity theory and the extended Cauchy-Born rule [6, 35], the strong ellipticity condition is applied to investigate the localized failure of carbon nanotubes at the continuum level.

Carbon nanotubes have been found to have exceptional mechanical and electronic properties. Applications of CNT's as building blocks for high-strength material or nano-device have been proposed and investigated in many studies. The mechanical characteristics of nanotube reinforced material or nanodevices with nanotube as building blocks depend on the intrinsic mechanical properties of CNTs. These include not only the elastic modulus of CNTs, which describes the elastic property at small strains, but also the stability and failure of CNTs at large strains.

Early studies show that CNTs can be subject to very large strain without causing failure or defect formation. Yakobson et al. [36, 37] investigated the buckling behavior of CNTs under large deformation using molecular dynamics (MD). It has been showed that under axial compression, nanotubes exhibit structural instabilities resulting in sideway buckling at as early as 5% of compressive strain. Large diameter tubes may buckle earlier by way of wall rippling. Torsion of a tube above a critical value results in ribbon-like flatten shapes. When bended beyond a buckling point, multiple kinks develop on the compressive side of the wall. These simulations agree with the experimental findings by Iijima et al [38]. Arroyo and Belytschko [39, 40] replicated these buckling patterns using finite element formulation based on crystal elasticity derived from bond-order potentials, and predicted a family of buckling patterns and post buckling motions.

In these deformations, the CNT remains in the elastic limit, and restores its original geometry once the load is removed. The material instability appearing as localized failure has also been observed and reported in the literature. Yakobson et al [37] and recently Marques [41], studied the failure of CNT under tension

at large strains. The initial response appears homogeneous; the hexagon bonds extend as the tube is stretched. At a certain critical level, one of few C-C bonds break almost instantaneously, and the resulting “hole” in a tube wall becomes a precursor of fracture. At this point, the strain redistributes itself to form a largely distorted neck between two quickly relaxing segments of the nanotube. This transition is followed by the formation of atomic chains being pulled out of tube segments. The breaking strains are found to be in the range of 30% to 40%, and the results are confirmed by Marques [41]. In the experimental study for tensile breaking mechanism of multiwall CNTs, Yu et al. [42] reported failure strain around 12% under tensile load. Belytschko et al [43], using a modified Morse potential, predicted tensional fracture strain from 10% to 16%, which are comparable to the experimental determined values. Mielke et al [44] further attributed the differences to the defects existing in the tube or being created during deformation.

Lourie et al [45] tested embedded nanotubes and reported some intriguing features of buckling and failure modes under compression. Instead of sideway buckling or rippling, embedded thin-wall tubes were observed to fail by compressive collapse or crushing, which manifests itself by progressive fragmentation of tubes separated by thin collapse zones scattered along the tube length. See Figure 4 in [45]. The critical stress, referred to collapse stress hereafter, was determined to be in the range of 116.7 to 151GPa, which is higher than the elastic buckling stress of laterally free tubes. The actual instability of an embedded tube is determined by the relative values of the critical stresses. If the tube is laterally constrained as in Lourie’s experiments, the Euler buckling stress could be higher than the collapse

stress. In this case, localized collapse may precede structural buckling. Srivastava and coworkers further studied the post-collapse atomic motion using tight-binding molecular dynamics [46, 47]. They reported that, at about 12% compression of a zigzag tube, the relaxation of compressive tube results in a spontaneous plastic collapse. Localized collapse zones appear at the ends of a tube through the formation of sp^3 diamond bond, driven by strain relaxation in the center region of the tube. The critical stress predicted by Srivastava is in the range of experimental estimations.

In this chapter, we are interested in predicting the conditions under which a homogeneous deformation of CNT may give rise to localized failure, in particular tensile necking or localized collapse under compression. Although the failure mechanisms at the atomic level and post failure motions can only be described with atomistic model, we speculate that onset of failure, which is intrinsically related to bond strength, could be reasonably captured by crystal elasticity derived from bond-order potentials. At a length scale comparable to tube size with the tube being characterized as a continuum, the collapse zones reported in Lourie's experiment may be regarded as strain localization bands. The necking zone appearing in tension can be modeled similarly. The scheme is illustrated in Figure 3.1. With this interpretation, the critical conditions can be established within the well-established mathematical framework for strain localization analysis [48, 1], which has been used historically to study the stability of elastic-plastic continuum [30, 49]. Recently, this approach has been applied to analyze at atomistic scale the incipience of dislocation and plastic deformation in crystals [31, 17, 18, 18].

This issue will be discussed further in Section 2. It should be noted that the present analysis relies on a continuum representation of nanotubes, which falls into the quasi-continuum framework. The atomistic informed continua depends on the particular selection of interatomic potential. In this chapter and following chapters, the Tersoff-Brenner many body potential [50, 24] is employed for characterize the interaction between carbon atoms. Since atomic scale kinematics is not considered, the analysis may tend to overestimate the limit strength. In addition, the stability results in this paper correspond to that of ideal, defect-free tubes. Recent studies show that the presence of defects can significantly reduce the ultimate strength of nanotubes [43, 51, 52].

Some classical results relating to strain localization analysis are summarized in Section 3.2, including a brief discussion on the connection to structural bifurcation. The extended Cauchy-Born rule is introduced in Section 3.3. In Section 3.4, a continuum model for CNT is adapted from the theories advocated in [53, 54, 55, 40, 39]. In Section 3.5, the critical conditions for localized deformation under compression and tension are computed and compared to results reported in the literature. The analysis is also applied to torsional failure, and the critical stress and strain for CNTs of various chirality are predicted.

3.2 Analysis of strain localization

The mathematical framework for determining the critical conditions for the onset of strain localization has been well established [48, 30], which is in the context of material instability. Within this framework, a material element is considered

subject to all around displacement boundary conditions consistent with homogeneous deformations. One wishes to determine conditions at which a homogeneous, quasi-static deformation increment could give rise to strain localization within a narrow band, in such manner that the deformation gradient increment $\dot{\mathbf{F}}$ allows a jump across the surface. With reference to Figure 3.1, let \mathbf{N} be the orientation of the band surface in the reference configuration. If the incremental displacement field is continuous, there is a kinematical compatibility condition that $\dot{\mathbf{F}}$ must have the form [1]

$$[[\dot{\mathbf{F}}]] = \mathbf{m} \otimes \mathbf{N}, \quad (3.1)$$

where $[[\cdot]]$ denotes the jump in the value of a function immediately across the surface, \mathbf{m} is an vector function of position and “ \otimes ” means the standard tensor product. Traction continuity across the jump surface requires that

$$[[\dot{\mathbf{P}}]]\mathbf{N} = \mathbf{0}, \quad (3.2)$$

where \mathbf{P} is the first Piola-Kirchhoff stress. To first order, the increment in the nominal stress immediately inside (indicated by a superscript “+”) and outside (“-”) the band are given as

$$\dot{\mathbf{P}}_{iA}^+ = \mathcal{A}_{i\alpha j\beta} \dot{F}_{j\beta}^+, \quad \dot{\mathbf{P}}_{iA}^- = \mathcal{A}_{i\alpha j\beta} \dot{F}_{j\beta}^-. \quad (3.3)$$

Here \mathcal{A} is the material elasticity tensor, which assumes the same value immediately across the band surface because the deformation at the incipency of bifurcation is homogeneous. This gives a jump in stress across the surface

$$[[\dot{P}_{i\alpha}]] = \mathcal{A}_{i\alpha j\beta} [[\dot{F}_{j\beta}]] = \mathcal{A}_{i\alpha j\beta} N_{\beta} m_j. \quad (3.4)$$

Traction continuity across the surface requires that

$$[[\dot{P}_{i\alpha}]]N_\alpha = \mathcal{A}_{i\alpha j\beta}N_\alpha N_\beta m_j = 0. \quad (3.5)$$

Writing

$$Q_{ij} = \mathcal{A}_{i\alpha j\beta}N_\alpha N_\beta, \quad (3.6)$$

the condition (3.5) requires that

$$Q_{ij}m_j = 0, \quad \text{or} \quad \det \mathbf{Q} = 0. \quad (3.7)$$

The tensor \mathbf{Q} is called the *acoustic tensor*. There exists a large body of classical literature on the stability of solids under finite deformation, see Ogden [48, 3] and reference therein. We shall discuss the acoustic tensor in more detail in Chapter 5. It has been known that $\det \mathbf{Q} = 0$ is a necessary condition for the existence of stationary discontinuity, in particular strain localization band. The condition also corresponds to loss of ellipticity of the governing equations for the quasi-static incremental deformation. Hill [56] pointed out that the condition (3.5) also corresponds to stationary traction. Suppose an incremental deformation given by $\dot{\mathbf{x}} = \mathbf{m}f(\mathbf{N} \cdot \mathbf{X})$ is superposed on a homogeneous deformation, thus giving a deformation gradient increment $\dot{\mathbf{F}} = f'\mathbf{m} \otimes \mathbf{N}$. The corresponding traction increment on the surface of normal \mathbf{N} is given by

$$\dot{t}_i = \mathcal{A}_{i\alpha j\beta}\dot{F}_{j\beta}N_\alpha = f'Q_{ij}m_j. \quad (3.8)$$

It follows that if $\det \mathbf{Q} = 0$, there exists a direction \mathbf{m} such that $Q_{ij}m_j = 0$, hence the traction is stationary with respect to such a deformation increment. If the

stationary point is followed by strain softening, the point then marks the incipient unstable response that often precedes material failure.

A remark on the relation between this work and the bifurcation analysis in Ref. [57, 53, 54] is in place. Both approaches originate from the stability analysis. As discussed before, when a material body is subject to mixed displacement/traction boundary conditions, bifurcations in the form of smooth inhomogeneous deformation is possible. Examples include Euler buckling and rippling. The bifurcation analysis by Huang's group falls into this category. In contrast, the present approach captures the transition point of $\det \mathbf{Q} = 0$ at which (2.44) is violated. Hill [48] argued that, if the acoustic tensor is indefinite, say having negative eigenvalue at an orientation \mathbf{N} , it is possible to construct a narrow band, bounded by surfaces with normal \mathbf{N} , across which the deformation gradient exhibits a jump of the form $[[\mathbf{F}]] = \mathbf{m} \otimes \mathbf{N}$, such that the integral (2.28) is negative. Therefore, the point $\det \mathbf{Q} = 0$ indicates the occurrence of possible banded localized deformation, which may occur even if the material body is subject to all around displacement boundary conditions.

3.3 Extended Cauchy-Born rule

For a nanoscale structure, the continuum theory cannot be applied directly since the object is essentially a discrete system. The Cauchy-Born rule bridges the microscopic kinematics and the macroscopic deformation field, based on which the crystal elasticity theory can be constructed [6, 35]. However, Cauchy-Born rule is originally proposed for simple crystals. For complex crystals, like graphenes

and CNTs, in order to develop the homogenized continuum model, an extended Cauchy-Born rule needs to be introduced.

the Cauchy-Born rule [6]. It stipulates that the mapping between deformed lattice vectors \mathbf{a} and reference lattice vectors \mathbf{A} is related by the deformation gradient \mathbf{F} ,

$$\mathbf{a} = \mathbf{F}\mathbf{A}. \quad (3.9)$$

Cauchy-Born rule connects the deformation of microscopic lattices and macroscopic deformations and has been widely used in crystal elasticity theories.

A perfect crystalline structure that can be represented as a periodic lattice structure with basis atoms. For mono-atomic crystals (one basis atom for a lattice point), the coordinates of atoms making up lattice vectors in the reference configuration $\mathbf{R}_{ij} = \mathbf{R}_j - \mathbf{R}_i$, where $i \neq j$ stands for two atoms labeled by i and j . Deformed lattice vectors given by the current atomic positions are $\mathbf{r}_{ij} = \mathbf{r}_j - \mathbf{r}_i$. Eq. (3.9) describes the motion of all the atoms in monatomic crystals, which means

$$\mathbf{r}_{ij} = \mathbf{F}\mathbf{R}_{ij}. \quad (3.10)$$

For polyatomic crystals (two or more basis atoms for a lattice point) that consist of more than one atom per primitive unit cell, Cauchy-Born rule cannot determine the atomic positions in deformed configurations. Suppose there are N_b basis atoms in the primitive cell. Then there are N_b sublattices in the crystal. Without loss of generalities, one sublattice or one atom in the unit cell labelled by 0 is fixed so that rigid body translations are ruled out. At the aid of translational symmetry, the position of the p th ($p = 0, 1, \dots, N_b - 1$) atom in the unit cell in the reference

configuration is expressed as

$$\mathbf{X}^{(p)} = l_k \mathbf{A}_k + \mathbf{T}^{(p)}, \quad (3.11)$$

where \mathbf{A}_k are undeformed lattice vectors, l_k are integers, $\mathbf{T}^{(p)}$ is the translation vector relative to the 0th atom in the unit cell, and k is a dummy index ranging from 1 to 3 (summing under convention). Obviously, $\mathbf{T}^{(0)} = 0$. With the sum rule, $l_k \mathbf{A}_k$ represents the lattice location of the unit cell that the p th atom belongs to. Given $N_b - 1$ translation vectors inside the unit cell and all lattice locations of the crystal, all the atomic positions can be uniquely determined. Assuming the translational symmetry still holds after deformation, the atomic position in a deformed configuration is

$$\mathbf{x}^{(p)} = l_k \mathbf{a}_k + \mathbf{t}^{(p)}, \quad (3.12)$$

where \mathbf{a} is the deformed lattice vector related with \mathbf{A} by (3.9), $\mathbf{t}^{(p)}$ is the translation vector in the deformed unit cell. It is noted that no explicit relation between $\mathbf{T}^{(p)}$ and $\mathbf{t}^{(p)}$.

The vector connecting any two atoms in the crystal can be written in the undeformed and deformed configurations, respectively,

$$\mathbf{R}^{(pq)} = \delta l_k \mathbf{A}_k + \mathbf{T}^{(pq)}, \quad \mathbf{r}^{(pq)} = \delta l_k \mathbf{a}_k + \mathbf{t}^{(pq)}, \quad (3.13)$$

where p and q are atomic labels in the unit cell, δl_k is the difference of Bravais locations, $\mathbf{T}^{(pq)} = \mathbf{T}^{(q)} - \mathbf{T}^{(p)}$ and $\mathbf{t}^{(pq)} = \mathbf{t}^{(q)} - \mathbf{t}^{(p)}$. Making use of Cauchy-Born rule (3.9), the deformed atomic vector is

$$\begin{aligned} \mathbf{r}^{(pq)} &= \mathbf{F}(\delta l_k \mathbf{A}_k + \mathbf{T}^{(pq)}) + \mathbf{t}^{(pq)} - \mathbf{F}\mathbf{T}^{(pq)} \\ &= \mathbf{F}\mathbf{R}^{(pq)} + \boldsymbol{\eta}^{(pq)}, \end{aligned} \quad (3.14)$$

where

$$\boldsymbol{\eta}^{(pq)} = \mathbf{t}^{(pq)} - \mathbf{F}\mathbf{T}^{(pq)}. \quad (3.15)$$

Since the translation vectors differ from lattice vectors, the mapping between $\mathbf{T}^{(pq)}$ and $\mathbf{t}^{(pq)}$ cannot be related by the deformation gradient. Therefore, $\boldsymbol{\eta}^{(pq)}$ do not vanish unless $p = q$, i.e. two atoms overlap in a same unit cell or fall into different unit cells but in a same sublattice. For monatomic crystals, $\boldsymbol{\eta}^{(pq)} = 0$. Then, Eq. (3.14) reduces to (3.9). The relation (3.14) is call extended Cauchy-Born rule. In section 3.4, we shall apply the extended Cauchy-Born rule to carbon nanotubes in order to construct an equivalent continuum model.

3.4 Strain localization of carbon nanotubes

The Tersoff-Brenner potential [50, 24] is used to model carbon-carbon bonding energy. This empirical potential has been widely used in studying graphite sheets and carbon nanotubes and is found to be able to accurately describe the bond energy, elastic modulus and even defect nucleation. In this potential, the interatomic energy between atom i and j is expressed by the function

$$V(r_{ij}) = V_R(r_{ij}) - BV_A(r_{ij}), \quad (3.16)$$

where r_{ij} is the distance between atoms i and j , V_R and V_A are the repulsive and attractive terms depending on the distance, and function B models the multibody coupling between bond ij and its environment which is a function of angles between ij and adjacent bonds. The functional form and parameters are given in [24]. The

total potential of whole tube is the sum of all bond potentials, given as

$$E = \sum_i \sum_{j>i} [V_R(r_{ij}) - B_{ij}V_R(r_{ij})] f_c(r_{ij}) \quad (3.17)$$

At an atomic site of a CNT, one can distinguish the three bond vectors in the unit cell of the honeycomb lattice of graphene by vectors \mathbf{A}_i , $i = 1, 2, 3$ which makes three angles, labeled such that θ_{ij} is the angle between bond i and j , see Figure 3.2(b). The average energy at an atomic site is obtained as half of the sum of the pair-wise bond energy of the three bonds, divided by the average area an atom occupies. This gives an energy density per unit reference area

$$W = \frac{1}{A_0} \sum_{i=1,3} [V_R(r_i) - B(\cos \theta_{ij}, \cos \theta_{ik})V_A(r_i)], \quad (j \neq k \neq i \neq j) \quad (3.18)$$

where $A_0 = 3\sqrt{3}/2r_0^2$, r_0 is the reference length of the bond. After deformation, according to the extended Cauchy-Born rule (3.14), the reference bond vector \mathbf{R}_i has a length

$$r_i = \|\mathbf{F}\mathbf{R}_i + \boldsymbol{\eta}\|, \quad (3.19)$$

where $\|\cdot\|$ is the norm of vector. The current angle between i th and j th bonds is

$$\cos \theta_{ij} = \frac{(\mathbf{F}\mathbf{R}_i + \boldsymbol{\eta}) \cdot (\mathbf{F}\mathbf{R}_j + \boldsymbol{\eta})}{r_i r_j}. \quad (3.20)$$

Substituting Eqs. (3.19) and (3.20) into the strain energy density (3.18) yields a function of deformation gradient \mathbf{F} and shifting vector $\boldsymbol{\eta}$

$$W = W(\lambda_i, \cos \theta_{ij}, \cos \theta_{ik}) = \tilde{W}(\mathbf{F}, \boldsymbol{\eta}, \mathbf{R}_1, \mathbf{R}_2, \mathbf{R}_3). \quad (3.21)$$

The shifting vector is determined at constitutive level by minimizing the energy relative to $\boldsymbol{\eta}$:

$$\frac{\partial \tilde{W}}{\partial \boldsymbol{\eta}} = 0. \quad (3.22)$$

This determines $\boldsymbol{\eta}$ implicitly as a function of \mathbf{F} .

Using the continuum description, the first Piola-Kirchhoff stress is derived by taking derivative of W relative to \mathbf{F} , evaluating at relaxation of $\boldsymbol{\eta}$.

$$\mathbf{P} = \frac{d\tilde{W}}{d\mathbf{F}} = \frac{\partial\tilde{W}}{\partial\mathbf{F}} + \frac{\partial\tilde{W}}{\partial\boldsymbol{\eta}} \frac{\partial\boldsymbol{\eta}}{\partial\mathbf{F}}. \quad (3.23)$$

Because the derivative to $\boldsymbol{\eta}$ vanishes at relaxation, the second term is eliminated.

The expression of nominal stress reduces to the original form (2.5). In detail,

$$\begin{aligned} \mathbf{P} = \frac{1}{A_0} \sum_{i=1}^3 \left\{ \frac{\partial V_R}{\partial r_i} \frac{\partial r_i}{\partial\mathbf{F}} - B(\cos\theta_{ij}, \cos\theta_{ik}) \frac{\partial V_A}{\partial r_i} \frac{\partial r_i}{\partial\mathbf{F}} \right. \\ \left. - V_A(r_i) \left(\frac{\partial B}{\partial \cos\theta_{ij}} \frac{\partial \cos\theta_{ij}}{\partial\mathbf{F}} + \frac{\partial B}{\partial \cos\theta_{ik}} \frac{\partial \cos\theta_{ik}}{\partial\mathbf{F}} \right) \right\}, \end{aligned} \quad (3.24)$$

where $j, k = 1, 2, 3$ and $i \neq j \neq k \neq i$. Further,

$$\mathcal{A} = \frac{d\mathbf{P}}{d\mathbf{F}} = \frac{\partial^2\tilde{W}}{\partial\mathbf{F}\partial\mathbf{F}} + \frac{\partial^2\tilde{W}}{\partial\mathbf{F}\partial\boldsymbol{\eta}} \frac{\partial\boldsymbol{\eta}}{\partial\mathbf{F}}. \quad (3.25)$$

From $\frac{\partial\tilde{W}}{\partial\boldsymbol{\eta}} = \mathbf{0}$, it follows that

$$\frac{\partial^2\tilde{W}}{\partial\boldsymbol{\eta}\partial\mathbf{F}} + \frac{\partial^2\tilde{W}}{\partial\boldsymbol{\eta}\partial\boldsymbol{\eta}} \frac{\partial\boldsymbol{\eta}}{\partial\mathbf{F}} = 0. \quad (3.26)$$

Combining (3.25) and (3.26) yields

$$\mathcal{A} = \frac{\partial^2\tilde{W}}{\partial\mathbf{F}\partial\mathbf{F}} - \frac{\partial^2\tilde{W}}{\partial\mathbf{F}\partial\boldsymbol{\eta}} \left(\frac{\partial^2\tilde{W}}{\partial\boldsymbol{\eta}\partial\boldsymbol{\eta}} \right)^{-1} \frac{\partial^2\tilde{W}}{\partial\boldsymbol{\eta}\partial\mathbf{F}}. \quad (3.27)$$

With the elasticity tensor in hand, the acoustic tensor can be expressed readily from Eq. (3.6), as

$$Q_{ij} = \frac{\partial^2\tilde{W}}{\partial F_{i\alpha}\partial F_{j\beta}} N_\alpha N_\beta - N_\alpha \frac{\partial^2\tilde{W}}{\partial F_{i\alpha}\partial\eta_k} \left(\frac{\partial^2\tilde{W}}{\partial\eta_k\partial\eta_l} \right)^{-1} \frac{\partial^2\tilde{W}}{\partial\eta_l\partial F_{j\beta}} N_\beta, \quad (3.28)$$

where \mathbf{N} is the orientation of the band surface. The singular point of the acoustic tensor, if exists, is determined numerically. The critical deformation is identi-

fied by varying \mathbf{N} over all possible orientations. In the next Section, this procedure is applied to determine to critical deformations for CNTs under uniaxial tension/compression and pure torsion.

It is known that the derivative of the cutoff function introduces a unphysical surge to the interatomic force at the cutoff distance [43]. The second derivative from the cutoff function is discontinuous at the cutoff distance, which may influence the instability strain predicted by the present method. To exclude these artificial effects the cutoff is directly applied on the force and second derivative from the pair-wise potential without cutoff. In other words, the derivatives of the cutoff function are not considered.

3.5 Results and discussion

3.5.1 Uniaxial tension and compression

The experiments by Lourie et al showed that under compression embedded nanotubes may develop thin crushing zones prior to failure [45]. Yakobson et al found that for CNT under tension, ductile necking may appear at 30% to 40% of stretching. Motivated by these findings, uniaxial tension and compression are considered in the present work. It is expected that the analysis would reasonably predict the critical condition for localized plastic collapse for laterally constrained nanotubes [45] since the boundary condition is close to all around displacement type. Prior to the onset of localization, the deformation gradient is homogeneous, and its in-plane part is given as

$$\mathbf{F} = \lambda_z \mathbf{e}_z \otimes \mathbf{E}_z + \lambda_\theta \mathbf{e}_\theta \otimes \mathbf{E}_\theta, \quad (3.29)$$

where $(\mathbf{e}_z, \mathbf{e}_\theta)$ and $(\mathbf{E}_Z, \mathbf{E}_\Theta)$ are the current and reference axes of the cylindrical-polar coordinates. Given an axial stretch λ_Z , the corresponding hoop stretch λ_Θ and shifting vector $\boldsymbol{\eta}$ are computed numerically from the equilibrium condition $P_{\theta\Theta} = 0$ and relaxation equation (3.22). Therefore, the critical state is determined from the following equations

$$\frac{\partial \tilde{W}}{\partial \boldsymbol{\eta}} = \mathbf{0}, \quad P_{\theta\Theta} = \frac{\partial \tilde{W}}{\partial \lambda_\Theta} = 0, \quad \det \mathbf{Q} = 0. \quad (3.30)$$

The solution of (3.30)₃ depends on the band normal \mathbf{N} . The critical stretch is defined by

$$\lambda_{crit} = \min_{\mathbf{N}} \{ \lambda_Z : \det \mathbf{Q}(\mathbf{F}, \mathbf{N}) = 0 \}.$$

A bi-section procedure is employed in finding the critical stretch.

3.5.1.1 Tension

Table 3.1 shows the critical stretches and the corresponding orientation angles for tubes of different chirality. The reported failure strains are in the range of 35% to 44% for a variety of tube types, in good agreement with the breaking strains predicted by Yakobson et al. [37] using MD simulation. In particular, the critical strain $\varepsilon_{crit} = 44.3\%$ for an armchair tube matches the breaking strain of 42% obtained by Yakobson for the same type of tube, as well as the 43% fracture strain obtained by Huang's group [57] using buckling analysis. Indeed, for an armchair the criterion derived here coincides with the buckling condition deduced in [57, 54] for the same type of tube with infinite radius. See Appendix for an analysis. In contrast to buckling results, the critical condition here is intrinsic to material strength and does not depend on tube geometry. Nevertheless, the values

appear to be in good agreement. Failure strain for zigzag tubes is found to be 35%, which is in excellent agreement with a recent MD simulation by Marques [41] where a breaking strain of 34% is reported for a (4,0) tube. Note that, throughout the whole thesis, strain is taken as the principal control variable for comparison because evaluating stresses of nanotubes depends on the thickness value of the tube used in calculation. When reporting the stress in the thesis, the tube thickness is assumed to be 3.34 Å.

3.5.1.2 Compression

The results from uniaxial compression are reported in Table 3.2. In [45], the collapse stress is estimated to be in the range of 115-150 GPa for thin but multi-wall nanotubes. Tight-binding MD simulation by Srivastava et al. [46] predicted a yield stress ~ 150 GPa occurring at $\sim 12\%$ of compression for zigzag tubes. The present method appears to over predict the critical strain; however, the critical stress for a zigzag tube (124 GPa) is in the experimentally determined range and is in good agreement with Srivastava's work. Critical strains for the onset of localized collapse are found to be around 20%, which also confirms Yakobson's observation that axially compressed tubes remains elastic till 20% of compression [36, 58].

As indicated in Figure 3.4, although a zigzag tube attains a minimum collapse strain with a band orientation $\Psi = 30^\circ$, there exists a range of orientations (0° to 40°) within which the collapse strain remains almost constant. In particular, at $\mathbf{N} = (1, 0)$, the collapse strain is predicted to be $\lambda_{crit} = 0.75$, or $\varepsilon_{crit} = 25\%$ with a corresponding compressive stress $\sigma_{crit} = 124$ GPa. The results are virtually

the same as the critical values attended at $\mathbf{N} = (\cos 30^\circ, \sin 30^\circ)$. It appears that collapse zones oriented from 0° to 40° are almost equally possible. This finding also correlates nicely with Lourie's experiments. Additionally, it is noted that the patterns of band orientation in tension and compression are different. In tension, the discontinuity surface turns to align with the tube axis regardless of tube chirality, as shown in Table 3.1 and Figure 3.5, Although not reported, the vector \mathbf{m} in these cases are also parallel to tube axis as well, indicating a precursor to a mode-I fracture. In contrast, in compression the orientations vary with tube chirality, indicating that the collapse zone may appear oblique.

Uniaxial stress-strain curves for selected tubes are plotted in Figure 3.6. The critical strains correlate nicely with the those at which the stress reaches global maximum. Beyond this point, the response is in strain-softening regime. This resonates with the observation made by Hill [56]. In essence, the present analysis captures failure point intrinsic to the atomic bond.

3.5.2 Pure torsion

It is speculated that if the lateral surface of tube is properly constrained (say embedded in matrix), localized failure may also appear in torsion. There are numerous reports on the torsional buckling of free tubes. However, to the best knowledge of the authors there is no report regarding the localized torsional failure for constrained tubes, although this failure mode could be of considerable interest to nanotube-reinforced composites. Here, the method is applied to pure torsion and the critical states are predicted.

The motion prior to failure is described by

$$r = \lambda_{\Theta} R, \quad \theta = \Theta + \kappa Z, \quad z = \lambda_Z Z, \quad (3.31)$$

where (R, Θ, Z) are the polar coordinates of a material point on the undeformed tube and (r, θ, z) are the current coordinates. Here κ is the twist angle per unit length. The deformation gradient in polar coordinates takes the form

$$\mathbf{F} = \lambda_{\Theta} \mathbf{e}_{\theta} \otimes \mathbf{E}_{\Theta} + \kappa r \mathbf{e}_{\theta} \otimes \mathbf{E}_Z + \lambda_Z \mathbf{e}_z \otimes \mathbf{E}_Z. \quad (3.32)$$

The tube is subject to torque at both ends. Equilibrium equations in the case reduce to

$$S_{\Theta\Theta} + 2\kappa R S_{\Theta Z} = 0, \quad S_{ZZ} = 0. \quad (3.33)$$

The first equation essentially states that the Cauchy stress in the hoop direction is zero. See [59, 60] for a derivation of these equations. The stretches λ_{Θ} and λ_Z are determined from these equations at prescribed torsion κ . Similar to the uniaxial case, the deformation at which the determinant of \mathbf{Q} becomes singular depends on the band orientation. The critical shear strain is identified according to

$$\gamma_{crit} = \min_{\mathbf{N}} \{ \kappa R : \det \mathbf{Q}(\mathbf{F}, \mathbf{N}) = 0 \}.$$

Table. 3.3 shows the critical shear strain, shear stress and the corresponding orientation for tubes of different chirality. The failure patterns are obviously more complicated than uniaxial tension and compression. This could be due to the anisotropy of the bond system, and that some bonds are subject to large rotation. Nevertheless, it can be seen that an armchair tube is more susceptible to

torsional failure. Additionally, an armchair tube could develop a discontinuity surface parallel the tube cross section whereas a zigzag doesn't. Stress-strain curves in Figure 3.7 also indicate that armchair tubes are weaker in torsion. This finding agrees with reference [61] in which the shear modulus of zigzag CNT was found higher than that of armchair CNT.

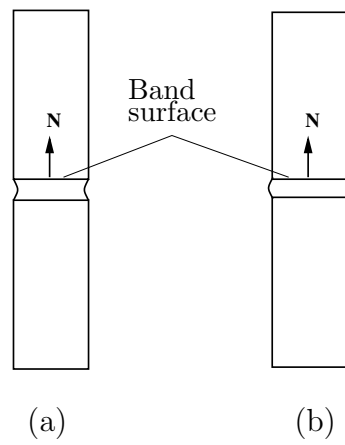


Figure 3.1: Schematics of strain localization bands. (a) Incipency of necking; (b) (Plastic) collapse zone, as reported by Lourie et al.

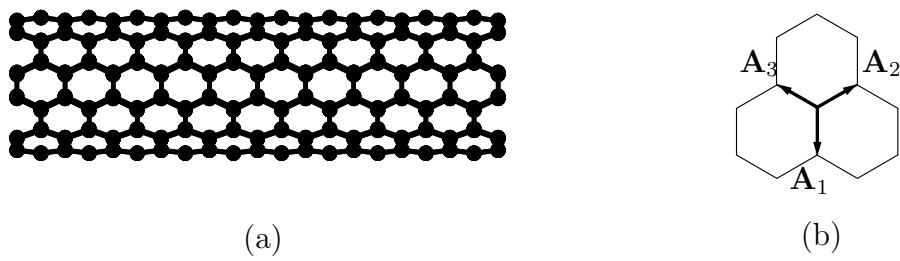


Figure 3.2: Global and local structures of carbon nanotubes. (a) Armchair tube; (b) a unit cell with three lattice vectors.

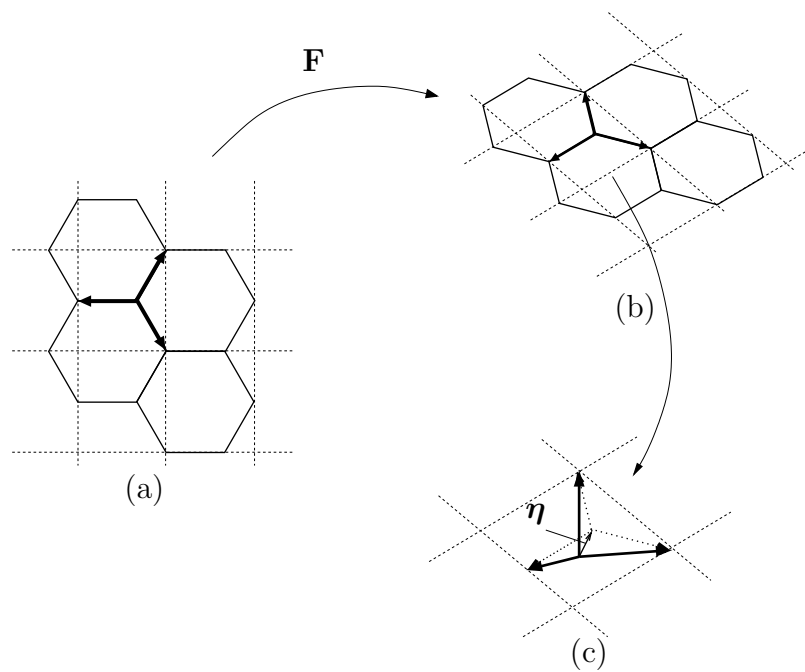


Figure 3.3: Modified Cauchy-Born rule for hexagon lattice: affine transformation and shifting vector.

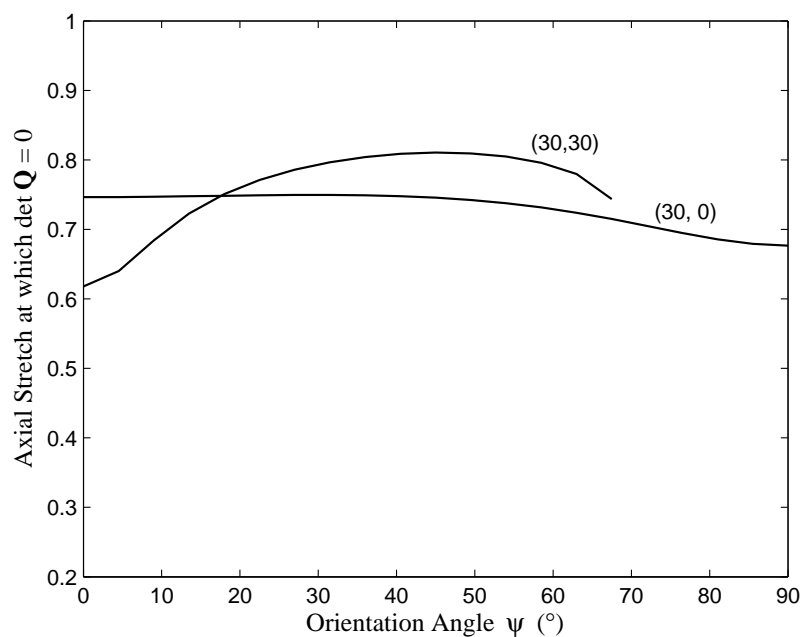


Figure 3.4: Critical stretch versus band orientation in compression. The angle Ψ is defined such that $\mathbf{N} = (\cos \Psi, \sin \Psi)$. For zigzag tube, the critical stretch is almost constant over a range of orientation.

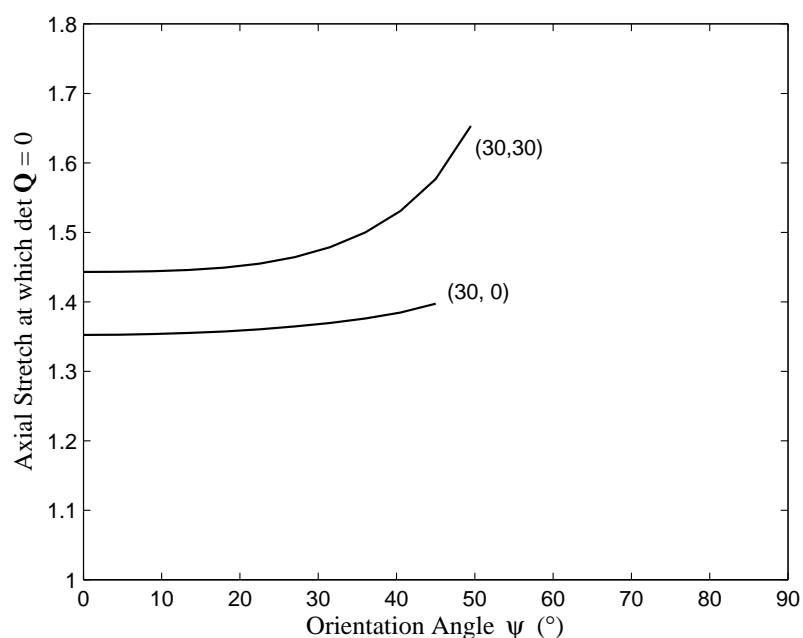


Figure 3.5: Stretch at which $\det \mathbf{Q} = 0$ versus band orientation in tension. The angle Ψ is defined such that $\mathbf{N} = (\cos \Psi, \sin \Psi)$. For armchair and zigzag tubes, the critical state occurs at $\Psi = 0$

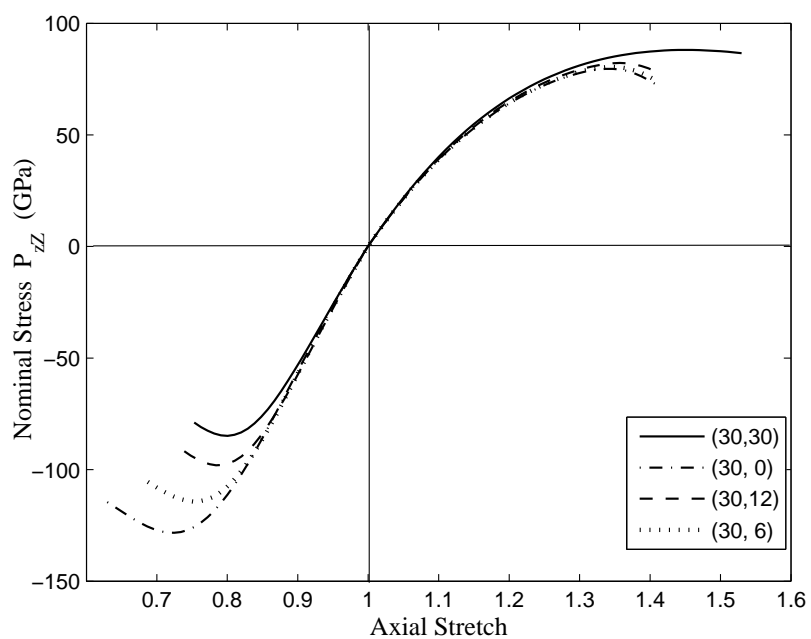


Figure 3.6: Uniaxial strain-stress curves for CNTs with different chirality.

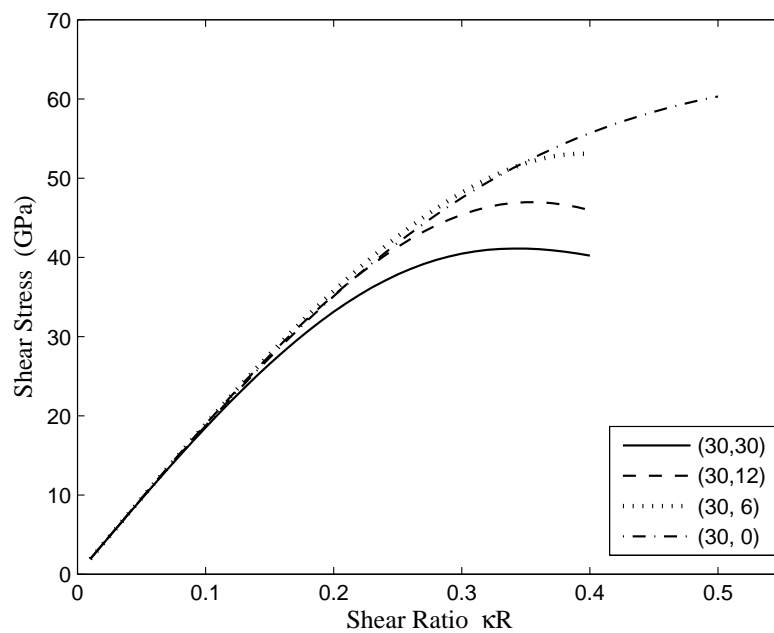


Figure 3.7: Shear stress versus shear strain.

Table 3.1: Critical tensile stress and strain

Uniaxial Tension			
Tube type	N_{crit}	$\varepsilon_{crit}(\%)$	$\sigma_{crit}(\text{GPa})$
(30, 30)	0°	44.3	88.0
(30, 20)	0°	37.8	84.8
(30, 12)	0°	36.1	82.1
(30, 6)	0°	35.5	80.1
(30, 0)	0°	35.2	79.2
(30, -12)	0°	37.9	84.8
(30, -15)	0°	44.3	88.0
(30, -18)	0°	37.8	84.8

Table 3.2: Critical stress and strain under compression

Uniaxial Compression			
Tube type	N_{crit}	$\varepsilon_{crit}(\%)$	$\sigma_{crit}(\text{GPa})$
(30, 30)	45.0°	18.9	83.3
(30, 20)	40.5°	19.1	85.5
(30, 12)	36.0°	19.7	93.5
(30, 6)	31.5°	21.3	106.4
(30, 0)	30.0°	25.0	123.9
(30, -12)	49.5°	19.5	86.2
(30, -15)	45.0°	18.9	83.3
(30, -18)	40.5°	19.1	85.6

Table 3.3: Critical twist and shear stress

Critical State in Pure Torsion			
Tube type	N_{crit}	γ_{crit}	τ_{crit} (GPa)
(30, 30)	166.5°	0.32	41.0
(30, 20)	162.0°	0.32	42.6
(30, 12)	162.0°	0.34	46.9
(30, 6)	157.5°	0.38	53.0
(30, 0)	94.5°	0.38	54.4
(30, -12)	81.0°	0.32	40.6
(30, -15)	86.5°	0.32	41.0
(30, -18)	162.0°	0.32	42.7

CHAPTER 4 THE ATOMISTIC FINITE ELEMENT METHOD

4.1 Motivation

Finite element methods (FEM) have proved powerful in solving boundary value problems. Many commercial FEM softwares and codes have been highly developed. With the advances of nanotechnology, there is a growing need for mechanical engineers to be able to perform fundamental atomic level analysis. While these analyses are commonly conducted by using molecular dynamics (MD) methods, it is possible to cast some MD code into the framework of FEM. The advantages are two folds: first, existing FEM resources can be exploited; second, the multiscale modeling turns very convenient in the same FEM framework.

Energy minimization is a general approach in both continuum mechanics and atomistics. For elasticity problems, FEM usually proceeds an optimization or energy minimization to find equilibrium states of the system. The principle of minimum potential energy is widely applied in solving the elastic statics. In atomistics, energy minimization is a cornerstone of molecular dynamics, i.e. the first step in the simulation. For a given force-field (interatomic potential), finding the equilibrium structure is often called molecular mechanics (MM) or statics which provides information that is complementary to molecular dynamics. Energy minimized structures represent the underlying configurations about which thermal fluctuations occur. Moreover, in some particular cases, for instance while investigating the stability of a quasi-equilibrium state, it is necessary to obtain the

equilibrium solution.

Motivated by the same goal to make the best use of FEM, various elements have been designed for different interatomic potentials and in different multiscale models. In particular, there are many atomic level FEM designed for carbon nanotubes (CNT). Based on the Tersoff-Brenner potential [24], Liu and Huang et al. [62, 63] proposed an atomic-scale ten-node element to analyze the mechanical behavior of CNTs. The authors also demonstrated the advantages of atomic FEM in saving computational time over the conjugate gradient method that is often used in the minimization process of molecular dynamics. The 10-node element includes the interacting neighborhoods within a certain range around the target carbon atom. While it can characterize bond stretch and bond angle bending, this element does not include bond torsion, thus cannot accurately describe the out-plane bending of a CNT. This method is inconvenient to extend to conform the second generation of Brenner potential [25] because in order to do so the number of nodes in each element has to be drastically increased. In refs.[62, 63, 64], the coupling of atomic scale FEM and continuum FEM was presented. The atomic level FEM was found suitable for multiscale modeling of static problems at nanoscale. Atomic FEM and continuum FEM can be generated within a unified framework. Afterwards, Mahdavi and Mockensturm [65] created a different four-node element for nanotubes in their hierarchical multiscale model. Similarly, the bond torsion is difficult to be incorporated in this method. Nasdala et al. [66] developed a four-node element for CNTs but applied the DREIDING force field [67]. This 4-node element consists of three subelements which include stretching, bending and bond

torsion, but the difficulty of implementation is relatively increased. It is fair to say that the current atomic level FEM is various and lacks the uniformity that is the trade mark of the continuum FEM.

The present work is aimed to provide a unified and systematic approach to develop new FEM for atomic structures, which can be embedded into existing FEM packages. We suggest a consistent logic that the definition of atomic element should conform to the class of interatomic potentials. For example, pairwise potentials, bond order many-body potentials, and atom-wise many-body potentials are the most widely utilized force fields in literature. We suggest to (1) take the bond energy as elemental energy for pairwise and bond-wise potentials, treat the atomic energy as elemental energy for potentials generated by Embedded Atom Methods, (2) consider the atoms included in the associated elemental energy as nodes of FEM, and (3) obtain the equilibrium configuration of the atomic structure by solving nonlinear FEM equations iteratively. When consistent with the class of potential in the atomistic theory, the atomic finite element is able to model different materials of the same potential class, using corresponding material modules. The element categorized by atomistic theory is named atomistic FEM here. In the present work, as an example, we propose a new six-element for carbon nanotubes that suits the bond-order many-body Tersoff-Brenner (TB) potentials [25, 24]. The new element can be easily extended in order to take into account the bond torsion effect.

4.2 Weak form: the principle of virtual work

The principle of virtual work (PVW) is an equivalent way of expressing the equations of equilibrium, and is usually referred as the starting point of finite element method. PVW states that for a mechanical system at equilibrium the total work done by virtual displacements is zero. Virtual displacement $\delta \mathbf{u}$ is defined to be arbitrary displacement which is *kinematically admissible*, i.e. satisfies displacement constraints. In continuum FEM, the PVW of deformable body is often applied as the weak form of the differential balance equations, i.e.

$$\begin{aligned} \nabla \cdot \boldsymbol{\sigma} + \rho \mathbf{b} - \rho \ddot{\mathbf{u}} &= 0, & (\text{Strong form}) \\ \int_{\Omega} \boldsymbol{\sigma} \cdot \nabla^s \delta \mathbf{u} dv + \int_{\Omega} \rho \ddot{\mathbf{u}} \cdot \delta \mathbf{u} dv &= \int_{\Omega} \rho \mathbf{b} \cdot \delta \mathbf{u} dv + \int_{\partial \Omega_t} \bar{\mathbf{t}} \cdot \delta \mathbf{u} da, & (\text{Weak form}). \end{aligned} \quad (4.1)$$

For an atomic system, atoms are considered as particles interacting with each other. Interatomic potential is used to characterize this interaction. Assume the total interatomic potential energy is a function of atomic positions $E = E(\mathbf{r}_i)$, ($i = 1 \sim N$). At equilibrium, each atom satisfies

$$\frac{\partial E}{\partial \mathbf{r}_i} - \mathbf{f}_i = 0, \quad (i = 1 \sim N), \quad (4.2)$$

where \mathbf{f}_i is the external force acting on atom i . The virtual displacement of atom i is supposed to be $\delta \mathbf{r}_i$. According to PVW, the total virtual work is zero, i.e.

$$\sum_{i=1}^N \left(\frac{\partial E}{\partial \mathbf{r}_i} - \mathbf{f}_i \right) \cdot \delta \mathbf{r}_i = 0. \quad (4.3)$$

One can easily show the equivalence of the equilibrium equation (4.2) and the virtual work equation (4.3) by noticing the fact that $\delta \mathbf{r}_i$ is arbitrary under dis-

placement constraints. Starting from PVW equation (4.3), the atomistic FEM can be developed.

4.3 Element definition

In continuum FEM, the continuous field is discretized into elements. The primary unknown field defined in each element are usually continuous functions, and are interpolated by element shape functions. The virtual displacement is expressed in terms of the same shape function in Galerkin methods. Correspondingly, one can write out the elemental weak form and FEM equations. After solving the assembled FEM equation, one obtains the approximate solution of a problem. Apparently, it is not necessary to discretize an atomic system. Each atom serves as a node in the atomistic FEM framework. One needs to directly solve for the spatial position of each atom in the equilibrium configuration. In order to utilize the existing FEM solver, we explicitly define the “element” in the atomistic case. As we shall discuss shortly afterwards, the element is dictated by the structure of the interatomic potential.

4.3.1 Three types of interatomic potential

In literature, three types of potential are often employed. Firstly, the most common one probably would be the pairwise potential, e.g. L-J potential and Morse potential, which has the form as

$$E = \sum_{i < j} V_{ij} = \sum_{i < j} V_{ij}(r_{ij}), \quad (4.4)$$

in which the potential energy stored in bond ij only depends on the distance between these two atoms, and the total energy in the system is the sum of every bond energy. The pairwise potential is a general form in modeling simple interactions between two particles.

Secondly, a similar bond order potential is created to characterize covalent-bonding energy, involving many-body effect. A prominent example is the Tersoff-Brenner potential of the first and second generations [24, 25] which are often used in describing hydrocarbon compound and fullerene. In these potentials, the energy in bond V_{ij} is not only dependent on its bond length but also associated with the length of other bonds or the angle between other bonds and itself. In general, this type of many-body potential can be written as

$$E = \sum_{i<j} V_{ij} = \sum_{i<j} V_{ij}(r_{ij}, r_{ik}, r_{jl}, r_{kl}, \dots). \quad (4.5)$$

We shall use the atomistic FEM based on T-B potentials to analyze the mechanical behavior of carbon nanotubes.

Thirdly, another type of many-body potential, which is usually utilized in characterizing metallic crystals, is obtained by the *Embedded Atom Method* (EAM) [68]. EAM views all atoms as being embedded in the host consisting of all other atoms. The general form of the potential energy by EAM can be written as

$$E = \sum_i E_i, \quad (4.6)$$

where E_i is the direct contribution to total energy from atom i . E_i may be expressed as follows

$$E_i = F_i[\bar{\rho}_i(r_{ij}, j \neq i)] + \frac{1}{2} \sum_{j(\neq i)} V_{ij}(r_{ij}), \quad (4.7)$$

where the first term F_i in (4.7) is electron-density dependent and represents the energy to embed an atom i in to the background electron density $\bar{\rho}_i$ at site i , in which $\bar{\rho}_i$ can be approximately written as a function of bond length linking atom i ; the second term in (4.7) is a pairwise interaction and denotes the core-core repulsion. Therefore, the energy function by EAM in (4.6) can be rewritten as the sum of atomic energy E_i that in general depends on positions of neighboring atoms around atom i , i.e.

$$E = \sum_i E_i(r_{ij}, j \neq i). \quad (4.8)$$

4.3.2 Atomistic element and the new 6-node element for CNTs

The element in atomistic FEM is defined according to the atomistic theory, namely the particular structure of the interatomic potential energy. According to the type of potential energies, we propose two elements: one is the bond-wise element for those bond-wisely defined potentials (many-body and pairwise), the other is the atom-wise element that suits EAM potentials. They represent two ways of partitioning the total energy. For bond based elements, the elemental energy is identical to the bond energy in bond-wise potentials (4.5), $E_e = V_{ij}$. Each element consists of the target bond and atoms contributing to the bond energy. For atom-wise potentials, the elemental energy is suggested to take the atomic site energy in (4.8), $E_e = E_i$. The atom based element in this case consists of the target atom and its neighboring atoms within the interaction range. The element is still locally defined, i.e. all the elemental properties can be computed in

terms of nodal positions within this element. By this definition, only one element module with different material modules is needed for a certain class of potential energy function.

In this work, a new six-node element is developed for CNTs. Figure 4.1 shows the configuration of this element. The Tersoff-Brenner potential of the first generation (type-I in [24]) is employed to model the interatomic interaction in carbon nanotubes (CNT). The elemental energy E_e is written as

$$E_e = V_R(r_{ij}) - \bar{B}(\cos \bar{\theta}_{ijk}, \cos \bar{\theta}_{jil})V_A(r_{ij}), \quad (k, l \neq i, j) \quad (4.9)$$

where $\bar{B} = (B_{ij} + B_{ji})/2$ is the function to describe $\sigma - \pi$ bond in the covalent system,

$$B_{ij} = [1 + \sum_{k(\neq i, j)} G(\bar{\theta}_{ijk})]^{-0.8}, \quad (4.10)$$

θ_{ijk} is the bond angle between ij bond and jk bond as shown in Figure 4.1, and the function G is given by

$$G(\theta) = a_0[1 + \frac{c_0^2}{d_0^2} - \frac{c_0^2}{d_0^2 + (1 + \cos \theta)^2}], \quad (4.11)$$

in which $a_0 = 0.011304$, $c_0 = 19$, $d_0 = 2.5$. The data of Brenner potential are adopted from reference [24, 57]. Note that in this thesis the cutoff function of T-B potentials is removed in computation due to its unphysical response in interatomic forces (see discussion in [54]). Eventually, \bar{B} can be expressed as a function of distances between atoms (nodes) within the element. Hence, the 6-node element for CNTs is locally defined.

Eq. (4.9) is based on the bonding energy in the first-generation Brenner potential [24]. Recently, some advanced bond-wise potentials [25, 69] have been

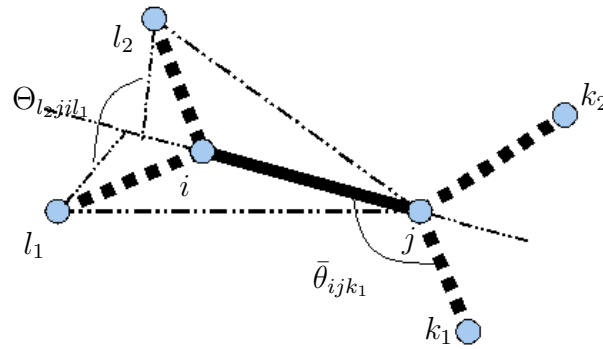


Figure 4.1: New six-node element for carbon nanotubes

proposed such that the dihedral bonding (bond torsion) in carbon-carbon double bond can be characterized. In these potentials, E_e is to be defined as a function including an additional dihedral term, and has a general form like

$$E_e = E_e(r_{ij}, \cos \bar{\theta}_{ijk}, \cos \Theta_{kjil}), \quad (4.12)$$

where the dihedral angle Θ_{kjil} is the angle between plane $k - j - i$ and $j - i - l$ and the associated cosine term can be calculated by

$$\cos \Theta_{kjil} = \frac{\mathbf{r}_{kj} \times \mathbf{r}_{ji}}{|\mathbf{r}_{kj} \times \mathbf{r}_{ji}|} \cdot \frac{\mathbf{r}_{ji} \times \mathbf{r}_{il}}{|\mathbf{r}_{ji} \times \mathbf{r}_{il}|}.$$

In ref.[69], the total potential energy is written as

$$E_e = \sum_{i < j} [E_{ij}^{TB} + \sum_{k(\neq i, j)} \sum_{l(\neq i, j, k)} E_{kijl}^{tors}], \quad (4.13)$$

where the first term in the parenthesis represents Tersoff-type bond order potential including bond stretch and bond angle bending, and the second term is the torsional potential which is a function of dihedral angle Θ_{kijl} . Thus, all quantities

in the advanced bond-wise potential (4.13) can be determined by nodal positions within the 6-node element. (See the dihedral angle $\Theta_{l_2jil_1}$ in Figure 4.1) Therefore, for Stuart potential [69], the 6-node atomistic element works as well. The advantage is that both the 1st-generation Brenner potential and the Stuart potential can be implemented in the same element, modifying only the corresponding material module in FEM packages.

The 6-node element can also be implemented for boundary atoms. For the element on the boundary, the number of nodes in the element may not be six, whereas the structure of the element does not change. In this case, the contributions from the missed atoms to B function and torsional potential are removed, i.e. skipped in the summation in equation (4.10) and (4.13). Certainly, missed atoms do not contribute to any force vector or stiffness matrix in FEM either.

4.4 Atomistic finite element equations

By using the variational principle, one can equivalently rewrite the PVW equation (4.3) as

$$\delta\Pi = \delta\Pi_{ext} - \delta\Pi_{int} = 0, \quad (4.14)$$

where $\Pi_{int} = \sum E_e$, and $\Pi_{ext} = \sum_i \mathbf{f}_i \cdot \mathbf{r}_i$ with \mathbf{f}_i assumed to be constant forces. Solving (4.14) which is usually a nonlinear equation system, one can obtain the equilibrium position of each atom.

We use the Newton-Raphson method in atomistic FEM to solve the nonlinear system iteratively. Rewriting the variational form (4.14) arrives at

$$\sum_i \mathbf{f}_i \cdot \delta\mathbf{r}_i - \sum_{elements} \left(\sum_j \frac{\partial E_e}{\partial \mathbf{r}_j} \cdot \delta\mathbf{r}_j \right) = 0. \quad (4.15)$$

One can expand the first sum term by Taylor series at the current state, then obtain the residual is

$$\mathbf{R} = \mathbf{F}_{ext} - \mathbf{F}_{int}, \quad (4.16)$$

where $\mathbf{F}_{ext} = \{\mathbf{f}_1, \mathbf{f}_2, \dots\}$ is the vector composed by external forces, and \mathbf{F}_{int} is the assembled internal force vector. Given an initial guess (at 0th step), the incremental displacement vector at k th step is computed as

$$\{\Delta \mathbf{u}\}^k = -\mathbb{K}^{-1}\{\mathbf{R}\}^k, \quad (4.17)$$

where \mathbb{K} is the global stiffness matrix

$$\mathbb{K} = -\frac{\partial\{\mathbf{R}\}^k}{\partial\{\mathbf{u}\}}, \quad (4.18)$$

and the atomic positions are updated step by step

$$\{\mathbf{r}\}^{k+1} = \{\mathbf{r}\}^k + \{\Delta \mathbf{u}\}^k, \quad (4.19)$$

until the solution converges to within a certain tolerance.

The elemental stiffness matrix \mathbf{K}_e and elemental internal force \mathbf{f}_e have expressions as follows

$$\begin{aligned} [\mathbf{K}_e]_{ij} &= \frac{\partial^2 E_e}{\partial \mathbf{r}_i \partial \mathbf{r}_j}, \\ \{\mathbf{f}_e\}_i &= \frac{\partial E_e}{\partial \mathbf{r}_i}, \end{aligned} \quad (4.20)$$

where i and j run over nodes (atoms) within the element, \mathbf{K}_e and \mathbf{f}_e are of dimension $3Ne \times 3Ne$ and $3Ne$ in 3-D space with Ne being the number of nodes in each element. \mathbf{K}_e and \mathbf{f}_e in (4.20) are used to assemble the global stiffness matrix and the residual vector. The assembly procedure is the same as classic FEM. The atomistic FEM has been implemented the nonlinear FEM package FEAP.

CHAPTER 5 AN ATOMIC LEVEL MATERIAL STABILITY THEORY

5.1 Introduction

Defect nucleation in atomic lattices is usually caused by local elastic instability that marks the elastic limit of the lattice structure. Thus, it closely relates to material instability. In a non-homogeneous system, the resulting transition from reversible (elastic) states to irreversible (inelastic) states first occurs at the “weak spots” where the local deformation has exceeded the stability limit of the lattice structure. Existing defects in the material often act as a predominant source of instability and material failure. In this chapter, the local unstable responses of a non-homogeneous atomic system containing defects are investigated.

Currently, there is no unified method for detecting the local instability in a defective atomic system. Jayanthi et al. [19] decomposed the global eigenfrequencies in terms of each atomic bond and defined a local participation fraction for indicating a bond-wise contribution to the global singularity. In this method, the local instability is well defined only when a global instability appears. However, in reality, the local instability may occur before global instabilities. Thus, a theory for the incipency of material instability prior global failure is imperative. Kitamura et al. [20, 21] proposed a method of stability analysis for inhomogeneous systems, in which the instability was detected by the eigenvalues of the global stiffness matrix. This analysis includes the material instability as well as structural instabilities. Dmitriev et al. [70, 23] demonstrated a local analysis scheme for the stability of

regions near a defect site, where only the atoms in a small vicinity of the defect were assumed movable. Strictly speaking, this embedded region stability is not of material but a local structure. When analyzing a nonhomogeneous system, Yashiro [15] used a stability indicator that was derived from the stability criterion by Wang [11] for uniform deformation. As discussed previously, Wang's criterion pertains to the stability condition with fixed Cauchy stress on the boundary of the material body. The unstable mode may not be kinematically admissible in other cases.

Historically, for material stability, Born [6] and others [9, 27, 11, 13] have derived stability criteria for perfect crystals under uniform deformations. These criteria are formulated in terms of the elastic constants and stresses. Thus, they are usually used for analyzing spatially uniform bifurcations and cannot be used when the deformation is non-uniform or the material is non-homogeneous. Using lattice dynamics [7], one can describe instabilities of a periodic lattice using the concept of *soft phonon mode*. The phonon dispersion relation (relation between wave vectors and the corresponding eigen-frequencies) displays all the possible structural vibration responses. Corresponding to each vibration frequency, there is one normal vibration mode. If the eigen-frequency for a certain vibration mode is zero or imaginary, the corresponding mode is called soft phonon mode. The homogeneous vibration modes can be regarded as the mode of infinite wavelength and is located on the acoustical branches of phonon dispersion curves. Although lattice dynamics is useful for analyzing lattice stability, it suffers from the same homogeneity restriction due to the fact that nonuniform deformation or the presence of defects destroys the periodicity of pristine lattices. Therefore, these stability theories for

crystals cannot be directly applied to non-uniformly deformed bodies or defective systems.

In nonlinear elasticity, material instability can be detected by the loss of strong ellipticity (SE) [1, 3], or equivalently, by the singularity of the acoustic tensor. For homogeneous materials under uniform deformation, SE guarantees the linearized stability of an elastic body subject to the boundary condition of place [29, 1, 3], and then indicates the constitutive relation of the material is well-posed. For a body undergoing non-uniform deformations, SE and the acoustic tensor can be evaluated at each material point, which is known to be fundamentally associated with the *ellipticity* of the governing partial differential equation (PDE) in that place [71]. Accordingly, the loss of SE relates to many important problems in continuum mechanics. Hill [48] first related the singularity of the acoustic tensor to the presence of a stationary acceleration wave. Knowles and Sternberg [71] demonstrated that for homogeneous materials weak discontinuity could occur where the acoustic tensor is singular. Rice [30] treated essentially the same instability in the context of shear band and connected it to the onset of localized discontinuous strains. Hill [56] further pointed out that the singularity of the acoustic tensor also indicates that the traction increment is zero due to the particular incremental deformation, and thus often marks an incipient local strain softening. Thus, by using the SE condition and the acoustic tensor, one is able to study not only the stability of the body as a whole, but also the responses of local material points.

In the framework of multiscale modeling, traditional continuum models

can be enhanced by adding in atomistic descriptions. Several recent studies have demonstrated that the SE condition can be successfully applied to identify material instability at atomic scales by using the atomic-informed continuum models. Gao and Klein [31, 32] constructed a continuum model from the atomic potential and applied the corresponding SE condition to detect strain localization. They also related the loss of SE to fracture nucleation in an initially perfect crystal. In Chapter 3 of this thesis, at the aid of crystal elasticity, SE is used to predict the localized failure strain of carbon nanotubes at the continuum level. Utilizing the quasi-continuum method, Zhu et al. [18] applied the acoustic tensor condition to predict the homogeneous dislocation nucleation in nano-indentation. In another series of papers, Li and Yip et al. [17, 16, 72] established an atomic-level stability condition (termed Λ -criterion) by extending the application of the continuum wave theory. They directly applied the propagation condition of acceleration waves [48] on each atom and expected that the dislocations would nucleate when this criterion was violated. In all these contributions above, however, the implementation of stability criteria involves either an equivalent continuum model or the concept of microscopic stresses and elastic constants [73, 74]. When passing from atomistic theories to the continuum model, one has to impose smoothness or homogeneity requirement on the deformation and the material. Due to this, the instability response is essentially examined at the continuum level. Moreover, problems would arise if there were defects or if the deformed field is distorted drastically. In these cases, the SE condition based on continuum theory is inapplicable because the length scale necessary to describe material responses must be reduced to the size

of atomic spacing and thus the definition of elastic constants and strains on an individual atom becomes unclear.

The discrete nature of atomic systems suggests a direct method for testing the local stability. In the context of classical stability theory, the positiveness of the second-order variation of total potential energy is evaluated. As a material particle, each atom contributes to the total potential energy and load-bearing capability of the system. If the local deformation is too large, an atom may lose the capability to resist any further deformations. In continuum theory, the material behavior is described by the strain energy density. For discrete atomic systems, in comparison, the energetic contribution of an atomic site, i.e. *site energy*, becomes the essential characteristic that describes the local response. Instead of using homogenization techniques to obtain an equivalent continuum model and then evaluating the equivalent energy density [31, 75], it is more reasonable to directly examine the response of the atomic site energy. Motivated by the continuum SE condition, one can test the behavior of the site energy by assuming a local testing mode that prescribes the motion of atoms interacting with the atom of interest. In general, an atom strongly interacts with the neighboring atoms within a certain distance; outside of the immediate range, the interactions are negligible. Therefore, one can attain a local stability criterion provided that: (1) the site energy can be identified, and (2) the test modes correspond to physically plausible motion. This approach applies to perfect as well as defective media because it does not depend on the pristine lattice and continuum concepts. By using this approach, an atomic level material stability criterion that suits non-homogeneous atomic systems is

proposed.

The present work is organized as follows. The strong ellipticity condition in nonlinear elasticity and the related acoustic tensor are reviewed in section 5.2. Parallel to the continuum theory, in section 5.3, an atomic stability criterion is introduced and the “atomic acoustic tensor” is defined as an indicator for identifying the local elastic instability (material instability) in atomic systems. The relevant physical implications of the atomic acoustic tensor are also demonstrated. In section 5.4, the application of the new indicator in defective metallic crystals is presented. In section 5.5, the atomic acoustic tensor is used to predict the critical tensile strain of carbon nanotubes with defects.

5.2 The strong ellipticity condition

5.2.1 Strong ellipticity and acoustic tensor

As reviewed in Chapter 2, for an elastic body under dead-load or all fixed displacement B.C., the linearized (infinitesimal) stability of an equilibrium configuration requires the inequality

$$\int_{\Omega_0} \delta \mathbf{F} \cdot \mathcal{A} \delta \mathbf{F} > 0 \quad (5.1)$$

to hold for all infinitesimal $\delta \mathbf{F} \neq 0$ satisfying $\delta \mathbf{u} = 0$ at $\partial \Omega_0 \setminus \partial \Omega_0^t$.

The local form of the stability condition (5.1) is given by

$$\delta \mathbf{F} \cdot \mathcal{A} \delta \mathbf{F} > 0, \quad (5.2)$$

for all $\delta \mathbf{F} \neq 0$, where the elasticity tensor is defined as (2.10). The local condition is a strong condition. If (5.2) is satisfied at all material points, the global condition (5.1) must hold.

Assume the incremental deformation gradient to be proportional to a rank-one tensor, i.e., $\delta\mathbf{F} = \mathbf{m} \otimes \mathbf{N}$, where \mathbf{m} is an Eulerian vector and \mathbf{N} is a Lagrangian vector [3]. Thus, the local condition (5.2) reduces to

$$(\mathbf{m} \otimes \mathbf{N}) \cdot \mathcal{A}(\mathbf{m} \otimes \mathbf{N}) > 0. \quad (5.3)$$

for all $\mathbf{m} \otimes \mathbf{N} \neq 0$, which is called the *strong ellipticity* condition. For homogeneous material under uniform deformation, satisfying (5.3) is sufficient for uniqueness of solution of a boundary value problem with *all* boundary condition of place [1, 3], which indicates that the uniform field is the unique solution in that case as long as the constitutive relation is well-posed. Therefore, strong ellipticity characterizes *material stability* that only depends on the constitutive behavior of the material and has nothing to do with boundary conditions.

In accordance with the strong ellipticity condition, a second-order tensor $\mathbf{Q}(\mathbf{N})$ depending on \mathbf{N} can be defined as

$$Q_{ij} = \mathcal{A}_{i\alpha j\beta} N_\alpha N_\beta, \quad (5.4)$$

so that the SE condition (5.3) is equivalent to that $\mathbf{Q}(\mathbf{N})$ is positive definite, i.e.,

$$\mathbf{m} \cdot \mathbf{Q}(\mathbf{N})\mathbf{m} > 0, \quad \forall \mathbf{m}, \mathbf{N} \neq 0. \quad (5.5)$$

The quantity $\mathbf{Q}(\mathbf{N})$ relates to the propagation of infinitesimal plane waves. For homogeneous material, the incremental form of the equation of motion becomes

$$\mathcal{A}_{i\alpha j\beta} \delta u_{j,\alpha\beta} = \rho_0 \delta \ddot{u}_i. \quad (5.6)$$

Superpose an infinitesimal plane wave perturbation on an infinite homogeneously deformed body $\delta \mathbf{u} = \mathbf{m} \exp[i(\mathbf{N} \cdot \mathbf{X} - ct)]$, with \mathbf{N} representing the direction of

wave propagation and c being the wave speed. Substituting (5.4) and $\delta \mathbf{u}$ into (5.6), one arrives at

$$Q_{ij}m_i m_j = \rho_0 c^2. \quad (5.7)$$

In three-dimension, three eigenvalues of $\mathbf{Q}(\mathbf{N})$ are associated with the acoustical vibration frequencies of the lattice in three independent directions when the wave-number approaches zero. Therefore, $\mathbf{Q}(\mathbf{N})$ is called the *acoustic tensor*.

5.2.2 Singular acoustic tensor at a material point

The strong ellipticity in the sense of elastic stability is used for evaluating material stability defined on the homogeneous body with uniform strains. Knowles and Sternberg [71] demonstrated that, if the acoustic tensor at a local material point is singular, i.e.,

$$\mathbf{m} \cdot \mathbf{Q}(\mathbf{N}; \mathbf{X}) \mathbf{m} = 0, \quad (5.8)$$

for some $\mathbf{m}, \mathbf{N} \neq 0$, the corresponding quasi-linear PDE systems (both equilibrium equation and its incremental form (5.6)) lose *ellipticity* at that point, and a discontinuous strain field is kinematically admissible. The discontinuity induces strain localization and fracture.

Additionally, the singularity of $\mathbf{Q}(\mathbf{N})$ results in the vanishment of the incremental traction and the incipency of strain softening. Recall that the traction $\mathbf{t} = \mathbf{P}\mathbf{N}$ at a plane of normal \mathbf{N} at \mathbf{X} . Under the incremental deformation gradient $\delta \mathbf{F} = \mathbf{m} \otimes \mathbf{N}$, the incremental traction is

$$\delta t_i = \delta P_{i\alpha} N_\alpha = \mathcal{A}_{i\alpha j \beta} N_\alpha N_\beta m_j. \quad (5.9)$$

Hence, if Eq. (5.8) is satisfied, the incremental traction $\delta \mathbf{t}$ vanishes on the plane

with normal \mathbf{N} in direction \mathbf{m} . indicating an incipient strain softening at the material point. Although softening at a local point does not necessarily means global instability of the whole body, it marks an initiation of material failure.

5.3 The atomic acoustic tensor

5.3.1 Global stability of an atomic system

Consider an arbitrary atomic structure with N atoms resting at an equilibrium state (assuming temperature $T=0$). Let \mathbf{r}_a be the position vector of atom a in a coordinate system. Including the potential of external forces, the total potential energy of the discrete atomic system is defined as

$$\pi = E - \sum_{m=1}^{N_b} \mathbf{f}_m \cdot \mathbf{r}_m, \quad (5.10)$$

where E is the internal energy that can be obtained from interatomic potentials, and \mathbf{f}_m are the external forces acting on atoms labeled by m with number N_b . The equilibrium of the system requires the first order variation to be zero,

$$\delta\pi = \sum_{i=1}^N \frac{\partial E}{\partial \mathbf{r}_i} \cdot \delta \mathbf{r}_i - \sum_{m=1}^{N_b} \mathbf{f}_m \cdot \delta \mathbf{r}_m = 0, \quad (5.11)$$

for all $\delta \mathbf{r}_i \neq 0$, which can also be realized in terms of the virtual work principle.

Since the virtual movement $\delta \mathbf{r}_i$ are independent mutually, the balance law of each atom at equilibrium can be obtained as

$$-\frac{\partial E}{\partial \mathbf{r}_i} + \mathbf{f}_i = 0, \quad (\mathbf{f}_i = 0 \text{ if } i \neq m). \quad (5.12)$$

Assume \mathbf{f}_m being constant. The global stability under small perturbations demands a positive second-order variation of the total potential energy, i.e.,

$$\delta^2\pi = \delta^2 E = \sum_i \sum_j \delta \mathbf{r}_i \cdot \frac{\partial^2 E}{\partial \mathbf{r}_i \partial \mathbf{r}_j} \cdot \delta \mathbf{r}_j > 0. \quad (5.13)$$

The global stability condition (5.13) applies to arbitrary atomic systems. In molecular mechanics, $\frac{\partial^2 E}{\partial \mathbf{r}_i \partial \mathbf{r}_j}$ for all i and j constitute the current global stiffness matrix of the structure. Condition (5.13) has been used in the stability analysis of inhomogeneous atomic systems [20, 21] and the near-surface lattices [23]. In these works, the eigen-properties of the global stiffness matrix are exploited.

5.3.2 Atomic acoustic tensor

Concentrate on the response of an atomic site. Let $\mathbf{r}_{ab} = \mathbf{r}_b - \mathbf{r}_a$ be the bond vector from atom a to atom b ($a \neq b$). In general, the internal potential energy at an atomic site a is a function of the bonds \mathbf{r}_{ab} connecting to a and other bonds \mathbf{r}_{cd} within the potential range. Write the internal energy as

$$E = \sum_a E_a = \sum_a E_a(\mathbf{r}_{ab}, \mathbf{r}_{cd}), \quad (5.14)$$

where E_a is the site energy of atom a which can be found by partitioning the total potential energy. For simple crystals characterized by pairwise interatomic potentials, the partition of the total energy is obvious; however, for those complex crystals, the partition is not straightforward. In this work, it is assumed that the atomic energy partition is possible. (In fact, one can refer to the strategy of Embedded-Atom Method (EAM) [68, 76], in which the site energy can be defined.) Although clearly the energy function of this form is not universal, it can be used to model a large family of atomic systems.

One restricts the test mode (i.e. the incremental motion) to be local, namely being nonzero only for atoms within the potential range from the site of interest, then the energetic test naturally localizes to the atomic site. According to (5.13),

after manipulations as shown in Appendix D.1, the stability condition of the atom site a is obtained

$$\sum_{b \neq a} \sum_{c \neq d} \delta \mathbf{r}_{ab} \cdot \frac{\partial^2 E_a}{\partial \mathbf{r}_{ab} \partial \mathbf{r}_{cd}} \delta \mathbf{r}_{cd} > 0 \quad (5.15)$$

holding for any small perturbations $\delta \mathbf{r}_{ab}$ which are nonzero for bonds within the potential range, where ab runs through the bonds connecting with the atom of interest and cd runs through the bonds in the potential range including ab . In particular, when the configuration is homogeneous (there is no defects and the atomic positions uniformly locate in both the equilibrium and perturbed configurations), the atomic condition (5.15) is equivalent to the global condition (5.13). Obviously, for nonhomogeneous configurations, satisfying (5.15) at all of atomic positions guarantees the linearized stability condition (5.13) (see Appendix D.1). The relation of local condition (5.15) and global condition (5.13) is identical to the counterpart of continuum stability theory as introduced in section 2.4.

Now, the interest is to find a sufficient condition for instability. To do this, consider a special mode of increment motion

$$\delta \mathbf{r}_{ab} = \mathbf{b}(\mathbf{r}_{ab} \cdot \mathbf{n}), \quad (5.16)$$

which can be regarded as the first order expansion of the plane wave perturbation as chosen in the continuum case. The mode (5.16) is schematically shown in Figure 5.1. If choosing atom a as the reference, the mode (5.16) indicates its neighboring atoms move along \mathbf{b} direction by uniformly varying magnitudes in terms of ratio $(\mathbf{r}_{ab} \cdot \mathbf{n})$. Hence, mode (5.16) describes a locally-homogeneous deformation with respect to atom a . If $\mathbf{n} \perp \mathbf{b}$, (5.16) is a shear mode; and if $\mathbf{n} \parallel \mathbf{b}$, it presents a

stretch mode. Requiring the energy increment to be positive in this perturbation yields the condition

$$\mathbf{b} \cdot \mathbf{Q}_a(\mathbf{n})\mathbf{b} > 0, \quad (5.17)$$

for all $\mathbf{n}, \mathbf{b} \neq 0$, where

$$\mathbf{Q}_a(\mathbf{n}) = \sum_{b \neq a} \sum_{c \neq d} (\mathbf{r}_{ab} \cdot \mathbf{n}) \frac{\partial^2 E_a}{\partial \mathbf{r}_{ab} \partial \mathbf{r}_{cd}} (\mathbf{r}_{cd} \cdot \mathbf{n}). \quad (5.18)$$

Obviously, (5.17) is a necessary condition of (5.15). If a negative increment

$$\mathbf{b} \cdot \mathbf{Q}_a(\mathbf{n})\mathbf{b} \leq 0 \quad (5.19)$$

exists for some directions \mathbf{n} and \mathbf{b} at a particular site, the site is identified unstable.

Tensor \mathbf{Q}_a is symmetric for simple crystals while it is asymmetric for complex crystals. In computation, the instability condition can be alternatively written as, $\mathbf{b} \cdot \bar{\mathbf{Q}}_a \mathbf{b} \leq 0$, for some $\mathbf{b} \in \mathbb{R}^3$ at the aid of its symmetrized counterpart, $\bar{\mathbf{Q}}_a = \frac{1}{2}(\mathbf{Q}_a + \mathbf{Q}_a^T)$.

The second order tensor \mathbf{Q}_a is called “atomic acoustic tensor” because it is the atomistic counterpart of the acoustic tensor in continuum elasticity. The eigenvalues of the continuum acoustic tensor in (5.4) precisely capture the elastic wave speed. For homogeneous elastic body under uniform deformation, as shown in Van Hove theorem (Appendix A), the positive definite acoustic tensor guarantees the global stability of the system if the boundary condition of place is held all around. In comparison, we show the discrete version of Van Hove theorem (in Appendix B), that is, as long as the atomic acoustic tensor is positive definite, it is assured that an pristine atomic system is stable under acoustical perturbation related to the elastic wave with infinitely long wavelength. Moreover, in simple

crystals where Cauchy-Born rule applies, the testing mode (5.16) prescribed on the neighboring atoms of atom a exactly reproduces the homogeneous deformation field endured by the whole body when the configuration is homogeneous. Then, in this case, \mathbf{Q}_a is identical to the continuum acoustic tensor (5.4) (see Appendix D.2).

In a discrete atomic system, the site energy of each atom replaces the role of the strain energy density in continuum theory. Mathematically, strong ellipticity (5.3) requires the strain energy density is rank-one convex [77]; by contrast, in an atomic system, one cannot define *ellipticity* since the governing equation is not PDE; the local stability condition (5.17) represents a convexity of the atomic site energy with respect to mode (5.16), i.e., the function $w(\varepsilon) := E_a(\mathbf{r}_{ab} + \varepsilon\mathbf{b}(\mathbf{r}_{ab} \cdot \mathbf{n}))$ is convex relative to ε at $\varepsilon = 0$, for any vectors (\mathbf{b}, \mathbf{n}) . Assume E_a is smooth, the convexity condition is equivalent to $\frac{\partial^2 w(\varepsilon)}{\partial \varepsilon^2} \Big|_{\varepsilon=0} > 0$. Further, for homogeneous body, the local mode (5.16) stands for a rank-one mode acting on lattice vectors: $(\mathbf{b} \otimes \mathbf{n})\mathbf{r}_{ab}$. Therefore, the condition (5.17) is the microscopic counterpart of the strong ellipticity condition in the continuum elasticity theory. Since (5.17) is defined for each atom and does not depend on the pristine lattice, it is expected that the criterion to be valid for pre-defective media as well, provided that the site energy can still be reasonable defined. Hence, the present work lays a solid foundation for probing the local failure mechanism of nanoscale structures.

The local instability condition (5.17) reproduces the Λ -criterion in refs. [17, 16] for perfect lattices (see Appendix D.2), but the present theory is derived from a different perspective. Note that the Λ -criterion was obtained by directly applying the continuum wave propagation theory in [48] and thus was confined to perfect

crystals with smoothly varying deformation. In Λ -criterion, the definition of elastic constants and strains on an atom is not clear in defective systems. In principle, the present work justifies the usage of strong ellipticity type of condition in atomic scale structures.

5.3.3 Implication of a singular atomic

acoustic tensor

5.3.3.1 Atomic stress and traction

The atomistic theory directly analyzes atoms and molecules. For an arbitrary atomic system that rests on an equilibrium state with zero temperature, the atomic level stress can be defined as

$$\boldsymbol{\tau}_a = \frac{1}{2\omega_a} \sum_{b \neq a} \mathbf{f}_{ab} \otimes \mathbf{r}_{ab}, \quad (5.20)$$

where ω_a is the atomic volume and

$$\mathbf{f}_{ab} = \frac{\partial E}{\partial \mathbf{r}_{ab}} \quad (5.21)$$

is the atomic force acting on atom a due to atom b . The definition (5.20) follows the static Virial stress [78, 79, 80, 81], BDT stress [82]. On the definition of microscopic stress, a more general form can be found in [83]. The atomic stress characterizes the interaction intensity measured in the local region containing atom a with volume ω_a . Following the atomic stress (5.20), the atomic traction, as a function of \mathbf{n} , is

$$\mathbf{t}_a(\mathbf{n}) = \frac{1}{\omega_a} \sum_{b \neq a} \mathbf{f}_{ab}(\mathbf{r}_{ab} \cdot \mathbf{n})/2. \quad (5.22)$$

where \mathbf{n} denotes a plane family as shown in Figure 5.1. The atomic traction is the contribution of atom a to the macroscopic traction and also represents an averaged

intensity of the interaction between atom a and its surroundings. In Figure 5.1, the effective path of interaction a - b acting on the plane family has length $(\mathbf{r}_{ab} \cdot \mathbf{n})$. Since two atoms share the interaction, $(\mathbf{r}_{ab} \cdot \mathbf{n})/2$ serves as the averaging weight. Although the sum of atomic forces $\sum_{b \neq a} \mathbf{f}_{ab}$ always vanishes at an equilibrium state, the weighted average is not zero unless $\mathbf{f}_{ab} \equiv 0$. Alternatively, $-\mathbf{t}_a(\mathbf{n})$ can also be considered as the cohesive force on plane \mathbf{n} supplied by atom a , which holds the atoms on two sides of the plane.

5.3.3.2 Vanishing the incremental atomic traction

When the material body deforms, atoms move and interact with each other to reach an equilibrium state. The macroscopic behavior is an average of microscopic responses. As demonstrated in [83, 84], the continuum balance equations such as the balance of linear momentum can be obtained by properly aggregating the atomic quantities within a certain length scale. The connection between the atomic level stress and the macroscopic stress can be found in [78, 83, 79]. From the kinetic stand point, the local instability can be identified from the incremental response of $\mathbf{t}_a(\mathbf{n})$.

By differentiating Eq. (5.22), one gets the incremental atomic traction

$$\delta \mathbf{t}_a(\mathbf{n}) = \frac{1}{2\omega_a} \sum_{b \neq a} \delta \mathbf{f}_{ab}(\mathbf{r}_{ab} \cdot \mathbf{n}) + \frac{1}{2\omega_a} \sum_{b \neq a} \mathbf{f}_{ab}(\delta \mathbf{r}_{ab} \cdot \mathbf{n}) - \frac{1}{2\omega_a^2} \sum_{b \neq a} \mathbf{f}_{ab}(\mathbf{r}_{ab} \cdot \mathbf{n}) \delta \omega_a. \quad (5.23)$$

Let $\delta \mathbf{r}_{ab}$ in Eq. (5.23) obey (5.16), then, $\delta \mathbf{t}_a(\mathbf{n})$ is the incremental response due to this virtual motion. Regardless of how ω_a is defined, for the testing mode (5.16), write the volume change as

$$\delta \omega_a = \omega_a(\mathbf{b} \cdot \mathbf{n}), \quad (5.24)$$

which can be obtained by the testing mode (5.16) that assigns an incremental deformation $\mathbf{b} \otimes \mathbf{n}$ to the local region. Using (5.24), the last two terms in Eq. (5.23) can be canceled, which leads to

$$\delta \mathbf{t}_a(\mathbf{n}) = \frac{1}{2\omega_a} \sum_{b \neq a} \delta \mathbf{f}_{ab}(\mathbf{r}_{ab} \cdot \mathbf{n}). \quad (5.25)$$

Substituting the internal force increment

$$\delta \mathbf{f}_{ab} = \sum_{c \neq d} \frac{\partial \mathbf{f}_{ab}}{\partial \mathbf{r}_{cd}} \cdot \delta \mathbf{r}_{cd} \quad (5.26)$$

into (5.25) and in the light of (5.16), the incremental atomic traction is rewritten as

$$\delta \mathbf{t}_a(\mathbf{n}) = \frac{1}{2\omega_a} \mathbf{Q}_a(\mathbf{n}) \mathbf{b}, \quad (5.27)$$

where

$$\mathbf{Q}_a(\mathbf{n}) = \sum_{b \neq a} \sum_{c \neq d} (\mathbf{r}_{ab} \cdot \mathbf{n}) \frac{\partial \mathbf{f}_{ab}}{\partial \mathbf{r}_{cd}} (\mathbf{r}_{cd} \cdot \mathbf{n}). \quad (5.28)$$

(5.28) is an alternative definition of atomic acoustic tensor and equivalent to (5.18).

It is apparent that $\delta \mathbf{t}_a(\mathbf{n})$ vanishes if $\mathbf{Q}_a(\mathbf{n})$ has zero eigenvalues. The zero increment in atomic traction has many important implications:

- **Losing restoring forces.** As discussed before, $-\mathbf{t}_a(\mathbf{n})$ can be considered as an averaged force that is supplied by atom a and acts on the neighboring atoms. $-\delta \mathbf{t}_a(\mathbf{n})$ is the corresponding increment when the neighboring atoms move according to the hypothetical mode (5.16). If $\mathbf{b} \cdot \mathbf{Q}_a(\mathbf{n}) \mathbf{b} > 0$ holds for any \mathbf{b} , it reads $-\delta \mathbf{t}_a(\mathbf{n})$ is converse to \mathbf{b} and serves as a restoring force to pull back the perturbed atoms toward the current equilibrium positions; if $\mathbf{b} \cdot \mathbf{Q}_a(\mathbf{n}) \mathbf{b} \leq 0$, then $-\delta \mathbf{t}_a(\mathbf{n}) \cdot \mathbf{b} \geq 0$, there are no restoring forces generated

from a , and then the local region of site a is unstable since atom a ceases supporting its surroundings under the particular testing mode.

- **Satisfying averaged monotonicity condition.** In the continuum stability theory, there is a macroscale *monotonicity condition* as $\delta\sigma \cdot \delta\varepsilon > 0$. In atomistic theory, one can define a similar condition for each atomic bond, i.e., $\delta\mathbf{f}_{ab} \cdot \delta\mathbf{r}_{ab} > 0$. Combining Eqs.(5.16), (5.21),(5.25),(5.26), (5.27), and (5.28), it is found $\mathbf{b} \cdot \mathbf{Q}_a(\mathbf{n})\mathbf{b} = \sum_{b \neq a} \delta\mathbf{f}_{ab} \cdot \delta\mathbf{r}_{ab}$. It means that the condition (5.17) represents an average of the monotonicity condition of each atomic bond. Notice the fact that the atom may still be stable (able to bear loads) with some bond breaking. Therefore, the condition (5.17) measures the stability of an atomic site in an average sense.
- **Inducing global failure.** The singularity of \mathbf{Q}_a signals the ultimate state that the associated atomic site can reach. Vanishing the incremental atomic traction is related to the loss of load-bearing capability from the unstable atom. Strain softening could occur at this site from which the instability of the whole system arises. A single unstable site does not lead to material failure; however, the coalescence of many singularities indicates strain localization.

5.3.3.3 Local instability and global failure

The atomic acoustic tensor captures the local elastic instability of an atomic site. Inequality (5.15) is a local version of (5.13) concentrating on an atom. For perfect lattices under uniform strain, these two conditions are equivalent if the

incremental motion is uniform too. For inhomogeneous media (either lattice or deformation is inhomogeneous), violating the local condition (5.15) at some isolated points may not necessarily make the global condition (5.13) fail. Therefore, a singular \mathbf{Q}_a does not imply global failure. Nonetheless, a singular \mathbf{Q}_a possesses the local significances as discussed above. The instability taking place in a local region is the origin of the instability of the whole structure. Here the local instability and global instability is distinguished because the local instability is the very reason for defect nucleation (like micro-cracks and dislocations). The atomic acoustic tensor is useful to investigate the propagation and development of a local singularity preceding global failure. The variation process may be presented by tracking the eigen-property of \mathbf{Q}_a temporarily and spatially.

It should be addressed that the application of \mathbf{Q}_a is convenient in practice. To check instabilities, instead of solving for the eigenvalues of a $3N \times 3N$ global stiffness matrix [19, 20, 21], the present method reduces the work to solving up to N times 3×3 local matrices. (N is the number of all the atoms; and the analysis can be made only in the critical region.) In the following, the atomic acoustic tensor is applied to discuss the local unstable mode in defective simple crystals and to predict the limit strains of carbon nanotubes with pre-existing defects.

5.4 Application: defective simple crystals

To show the validity of the atomic acoustic tensor, it has been applied in analyzing the defective structure with triangular 2-D lattices embedded with pre-existing cracks, voids and vacancies, as depicted in Figure 5.5. The 2-D triangle

lattice can be regarded as a (1 1 1) plane in the fcc crystal. In general, the pre-existing defects serve as the “weak spots” around which local instability tends to occur. Traditional stability theories cannot be directly applied to analyze the inhomogeneous media. In this section, the atomic acoustic tensor is used to study the local elastic stability in the defective region. The unstable modes of these 2-D models are obtained.

In computation, the Morse pair potential is employed to describe the interaction between two atoms, i.e.,

$$V(r) = \beta[e^{-2\alpha(r/r_0-1)} - 2e^{-\alpha(r/r_0-1)}] \quad (5.29)$$

where the equilibrium atomic distance r_0 and the bond energy β are assumed to be unit in computation, and the parameter $\alpha = 7$. The cutoff distance is set as $r_{max} = 2.50r_0$. Then, the site energy and the atomic acoustic tensor can be easily written out as in Appendix D.2.

The deformed configurations is obtained by prescribing displacement increment on the top boundary of the 2-D atomic sheet. The structure is relaxed to the equilibrium state by means of molecular statics. The second order tensor $\mathbf{Q}_a(\mathbf{n})$ is evaluated for each atom through a series of orientations, $\mathbf{n} = [\cos \theta \ \sin \theta]$ with $\theta \in [-90^\circ, 90^\circ]$. Meanwhile, for each orientation, the smallest eigenvalue of tensor $\mathbf{Q}_a(\mathbf{n})$ and its corresponding eigen-mode are computed. Thus, the minimum eigenvalue of this atomic site can be found. When the eigenvalue pass from positive to negative, the associated vectors (\mathbf{n}, \mathbf{b}) denote the critical orientation and the unstable moving direction respectively. If $\mathbf{n} \perp \mathbf{b}$, the unstable mode expressed by(5.16) is a shear (transverse) mode that may produce a dislocation with

slip plane described by its normal \mathbf{n} and Burgers vector \mathbf{b} ; if $\mathbf{n} \parallel \mathbf{b}$, mode(5.16) is longitudinal and represents an incipient microcrack. In the general case, the convention in ref.[16] is accepted. The mixed mode is transverse when the acute angle between (\mathbf{n}, \mathbf{b}) is larger than 60° , is longitudinal when the angle is smaller than 30° , and is just mixed when the angle is between 30° and 60° . To visualize the singularity, the deformed atomic structure is plotted, in which the grayness of each atom denotes the minimum eigenvalue of $\mathbf{Q}_a(\mathbf{n})$. The grayness is obtained by scaling the eigenvalue of \mathbf{Q}_a from 0 to 1. Increasing grayness stands for decreasing eigenvalues. The darkest (black) point is unstable. The vector pair (\mathbf{n}, \mathbf{b}) corresponding to the unstable atom is denoted by the angles $(\theta_{\mathbf{n}}, \theta_{\mathbf{b}})$ measured in the prescribed coordinate system.

Firstly, a 2-D atomic sheet embedded with Mode-I crack is stretched (see Figure 5.5). In Figure 5.3(a), the deformed Mode-I crack was shown and the minimum eigenvalue of \mathbf{Q}_a of each atom were plotted. The tensile strain in the direction perpendicular to the crack is about 4.4%. Singular atoms were found around the crack tip which was the most unstable region in a cracked body. Those unstable atoms were labeled by number 1 ~ 4, the corresponding critical vectors of which were listed in Table 5.1. The unstable mode of each singular atom can be analyzed respectively. To do this, the vicinity of each unstable atom was picked out, and the critical plane and moving direction of neighboring atoms were drawn schematically in Figure 5.3(b). (The same visualizing process was used in other following cases.) By the convention stated before, atom 2 was unstable in a longitudinal mode, the critical plane of which was parallel to the crack surface; the critical plane would

become the separation surface indicating the direction of crack growth. Atom 3 was unstable under a transverse mode, and atom 1 and 4 were unstable under mixed modes. Essentially, the combination of these modes indicated a tendency of dislocation emission from the crack tip. The critical planes of atom 1 and 4 captured the associated slip plane of dislocations.

Secondly, a shear strain was applied on the same cracked atomic structure, producing a Mode-II crack. In the same way, the deformed body was drawn. Figure 5.4(a) showed the Mode-II crack with 10% shear strain. Likewise, the crack tip was found to be the most unstable region. There were three atoms with singular Q_a . From Table 5.1, it was found that all unstable modes were longitudinal and had a common critical plane which was still parallel to the crack surface. As depicted in Figure 5.4(b), the moving direction tended to shear and separate the critical plane, which suggested the Mode-II crack would grow along the existing crack surface.

Afterwards, another example was a pre-existing void in the atomic sheet. Consider two types of loading conditions: uniaxial stretch and equally biaxial stretch. Under uniaxial tension, the void behaved like a Mode-I crack. Figure 5.5(a) presented the stretched void and unstable regions at 6.5% strains. The unstable region concentrated at two sides perpendicular to the stretched direction. Due to symmetry, half of the unstable region was plotted in Figure 5.5(b) due to symmetry. It was found that, as demonstrated in Table 5.2, the instability modes of a uniaxially stretched void were quite similar to those of the Mode-I crack in Table 5.1. Atoms 2 and 3 on the edge of the void were unstable under a longitudinal mode; then, a crack would initiate there. Atoms 1,4 and 5 were unstable due

to mixed and transverse modes, as might lead to dislocation nucleation. Thus, uniaxially stretching a void would result in crack nucleation and subsequent crack propagation.

For the void under biaxial tension, local instability modes were much different from the previous case. As shown in Figure 5.6(a), unstable region was uniformly distributed around the hole of a 5% biaxially stretched void. Crack would nucleate at different positions simultaneously. The instability modes of those unstable atoms were depicted in the upper-right quarter in Figure 5.6(b). Table 5.2 listed critical vector pairs of the instability modes. Mixed modes were found to be dominant in a biaxially stretched void. It suggests that dislocation emission and diffusion would happen with bond breaking. Thus, a biaxially stretched void tends to expand uniformly.

5.5 Application: carbon nanotubes

The criterion was also applied to identify the critical load at which the local instability occurs in defective carbon nanotubes (CNTs) under tension. Tersoff-Brenner potential [24] was employed to model the atomic interactions on nanotubes. This empirical potential has been widely used in studying carbon nanotubes and is found to be able to accurately describe the bond energy, elastic modulus and even defect nucleation. In this potential, the interatomic energy between atom a and b is expressed by the function

$$V_{ab} = V_R(r_{ab}) - B(\cos \bar{\theta}_{abj}, \cos \bar{\theta}_{kba})V_A(r_{ab}), \quad (i \neq j \neq a \neq b), \quad (5.30)$$

where r_{ab} is the distance between atoms a and b , $\bar{\theta}_{abj}$ denotes the angle between bond ba and bj , V_R and V_A are the repulsive and attractive terms depending on the interatomic distance, and function B models the multi-body coupling between bond ab and its environment, which characterizes π bond in sp^2 hybridized carbon rings and is a function of angles between bond ab and its adjacent bonds. The functional form and parameters are given in [24].

According to the bond structure of carbon nanotubes and graphites, the interaction between a carbon atom and its first layer neighboring atoms is responsible to bond breaking and rupture. The second layer dominates the bond-angle bending. The third layer relates to the out-plane bending. Under uniaxial tension, fracture due to bond breaking is the principal failure mechanism of carbon nanotubes at room temperature [85, 41]. As was pointed by Belytschko and Xiao [43], bond-angle bendings do not affect the fracture of nanotubes. By these observations, in this work, the summation in (5.18) was carried out for the bonds within the first layer neighborhoods of a carbon atom, and bending interactions were ignored. The potential energy was assumed to be determined merely by the distance between atoms within the first layer. In other word, the bond potential V_{ab} in (5.30) was considered as a function of bond length r_{ab} , r_{aj} , and r_{bk} where j and k are the first-layer neighboring atoms of a and b . The magnitude of the interatomic force between atom a and atom b was obtained by differentiating the total potential energy (summing up (5.30) through all C-C bonds) with respect to r_{ab} . For the definition of atomic stress in carbon nanotubes, we refer to ref. [86]. Note that the resulting interatomic force had an additional term than the case of

pure pairwise potentials (like(5.29)), which came from the derivative to function $B(\bar{\theta}_{abj}, \bar{\theta}_{kba})$, i.e. $\frac{\partial B}{\partial r_{ab}}$. This term reflects the influence of the π bond in strengthening the cohesive interaction between carbon atoms. Then, the atomic stress can be calculated by (5.20); The atomic acoustic tensor for nanotubes can be calculated by the alternative definition (5.28) in the sense of incremental atomic traction.

The calculation was carried out to both perfect and defective nanotubes by using the molecular mechanics method introduced in Chapter 4. After obtaining the equilibrium state of the carbon nanotube, the atomic acoustic tensor was computed for each carbon atom. As suggested in [75], the evaluated orientation \mathbf{n} was set to be parallel to the tube axis. If the atomic acoustic tensor has negative eigenvalues at some sites, there are local instabilities at this equilibrium configuration. Figure 5.7 shows the result of perfect carbon nanotubes, armchair type (10,10) and zigzag type (17,0). The deformed shape of nanotubes at different strains is plotted. For each configuration, the smallest eigenvalue of $\mathbf{Q}_a(\mathbf{n})$ of each atom were calculated and visualized in the same way as before.

As shown in Figure 5.7, carbon atoms in (10,10) became unstable at strain about 30%, which agreed with molecular dynamics (MD) and quantum mechanical results in [37, 41, 44, 87]. Since the axially oriented bond endured a higher strain, the zigzag tube (17,0) lost stability at a smaller strain 19.1% as reported in [85, 44]. The evolution of bond strength was demonstrated by the variation of \mathbf{Q}_a . Similar to ref. [75], the eigenvectors associated with those singular eigenvalues here were found to be parallel with tube axes in both cases, which indicated the bond could break locally. It was also found that nanotubes deformed uniformly in a long period

and the local unstable mode appeared quickly when the strain approached to the critical level. Thus, the brittleness of nanotube's rupture at low temperatures was verified by the local instability analysis.

Stone-Wales (SW) dislocation [88, 89] is a topological defect in nanotubes. It nucleates under large stresses via a C-C bond rotation. The resulting 5/7/7/5 ring destroys the hexagonal geometry of perfect nanotubes and releases the excessive strain energy. The successive separation and glide of pentagon-heptagon pairs induces the intramolecular plasticity and ductile response of carbon nanotubes. S-W defects may behave as a core of crack nucleation and moderately weaken the strength of the tube [88, 89, 44, 90]. In this work, one S-W defect was embedded in both (10,10) tube and (17,0). Adding axial loads by displacement control, it was found S-W defects disturbed the uniform deformation in the initially perfect tubes. Figure 5.8 shows the smallest eigenvalues of \mathbf{Q}_a at various strains. The incipient instability occurred around 21% and 14% strain for the armchair and the zigzag respectively. The unstable strain range was about 21.3~26.1% for armchair and 14~18% for zigzag tubes. In comparison, by molecular dynamics simulations, Marques et al. [41] reported that SW defective tubes break at about 25% strain; the *ab initio* simulations [90, 44] found a single S-W defect reduced breaking strain of a (5,5) tube to 22 ~ 24%, and a (10,0) tube to 13.9% strain. The local instability indicated by the atomic acoustic tensor agreed well with these atomistic simulations. Moreover, the atoms in heptagon rings became unstable first in both types of nanotube. When loaded further, the unstable zone spreads out along the heptagon ring and quickly leads to a global instability (MM computation fails to

converge). The same scenario has been found in ref.[43].

Furthermore, a cracked tube was created by removing one C-C bond. This resulted in a symmetric crack in the zigzag tube, an asymmetric crack in the armchair tube, similar to those considered in [43]. Figure 5.9 shows that, around 19% and 14% for armchair and zigzag respectively, local instability firstly occurs at the crack tips that becomes mechanically unstable. When loaded further, the unstable zone quickly spreads out till the tube lost global stability. The pattern of spreading appears qualitatively similar to the description in [43].

The introduced crack has a different bond structure as compared to vacancies considered by Mielke et al. [44, 87]. In order to make comparison, firstly, a non-reconstructed vacancy was studied. The critical strain of zigzag tube as 14% agreed fairly well with the predictions in [44]. The predicted limit strain of armchair was around 20%, slightly higher than that in ref. [44, 87]. The probable reason would be that since the armchair tube with vacancy in Figure 5.10 is not axially symmetric, the prescribed testing mode may not be the most critical mode. In fact, the predicted strain values were still comparable with some MD and quantum mechanics predictions.

We also considered reconstructed vacancies in a (17,0) zigzag tube with one-atom and two-atom missed respectively. In both cases, the initial instability was found to occur around 13.0% strain. When loaded further, the unstable zone spreads and the tube lost global stability at about 17% strain. Figure 5.11 shows the distribution of unstable sites at various strains. We have performed analysis on a (10,10) armchair tube with an asymmetric one-atom vacancy. The onset of

unstable atoms was captured at 12.8% strain, and the tube quickly lost global stability when loaded slightly further. The limit strains for both the armchair and the zigzag tubes compared reasonably well with Mielke's predictions. The armchair result also agreed with the reported range in [87].

Finally, the predicted critical strains for various case are listed in Table 5.3 and 5.4. Figure 5.5 shows the tensile stress strain curves of the pristine and selected defective tubes. The limit strains correlate nicely to the sudden loss of stress in the response.

Table 5.1: Instability modes in Mode-I and Mode-II cracks

Mode-I crack (Fig.5.3)				Mode-II crack (Fig.5.4)			
Atom	\mathbf{n} ($^\circ$)	\mathbf{b} ($^\circ$)	Mode	Atom	\mathbf{n} ($^\circ$)	\mathbf{b} ($^\circ$)	Mode
1	45	90	M	1	90	71	L
2	90	90	L	2	90	70	L
3	0	90	T	3	90	252	L
4	-45	-90	M	–	–	–	–

Table 5.2: Instability modes of the void under stretch

Mode-I crack (Fig.5.5)				Mode-II crack (Fig.5.6)			
Atom	\mathbf{n} ($^\circ$)	\mathbf{b} ($^\circ$)	Mode	Atom	\mathbf{n} ($^\circ$)	\mathbf{b} ($^\circ$)	Mode
1	45	90	M	1	-72	-34	M
2	90	90	L	2	117	120	L
3	90	90	L	3	90	147	M
4	0	-90	T	4	18	-18	M
5	-45	-90	M	5	-18	18	M

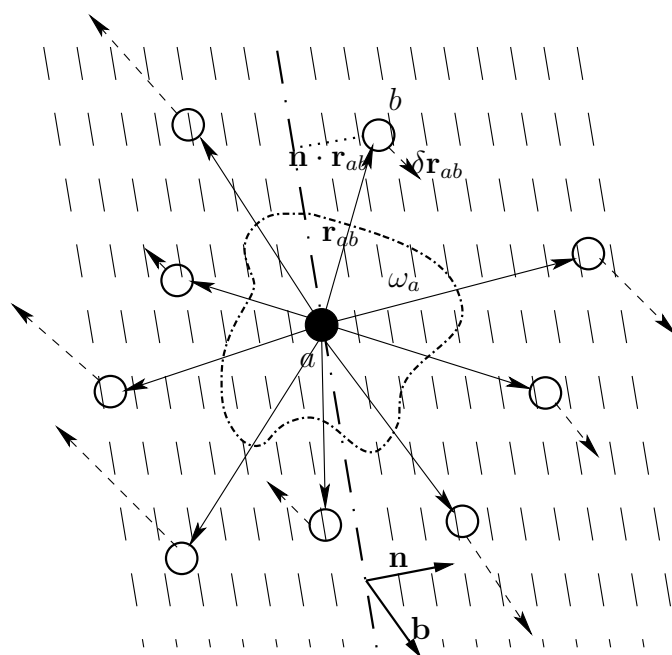
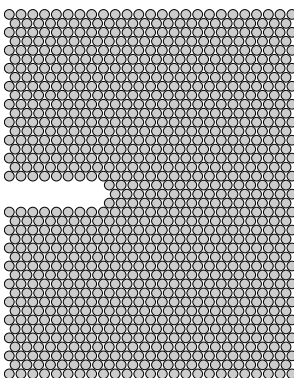
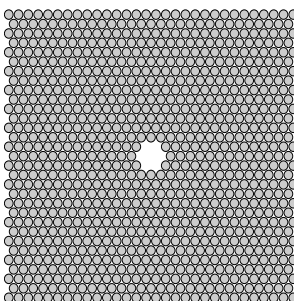


Figure 5.1: The local environment of an atom site a is shown in 2-D. \mathbf{r}_{ab} denotes the position vector and \mathbf{f}_{ab} represents the force between a and b parallel to \mathbf{r}_{ab} . A family of planes with normal \mathbf{n} exist spatially. The atomic traction is averaged in the assumed region with volume ω_i and measured with respect to plane \mathbf{n} . The variation of position vectors is supposed to be $\delta\mathbf{r}_{ab} = \mathbf{b}(\mathbf{r}_{ab} \cdot \mathbf{n})$. The moving magnitudes relative to a increase uniformly by ratio $(\mathbf{r}_{ab} \cdot \mathbf{n})$.

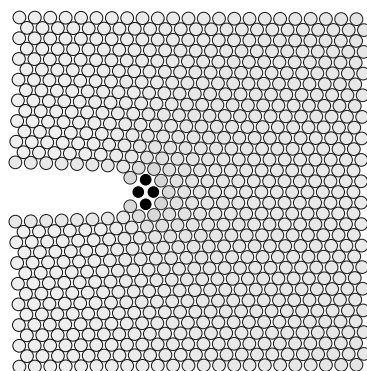


(a) An edge crack

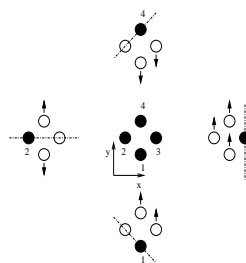


(b) A void

Figure 5.2: Undeformed 2-D atomic sheets:

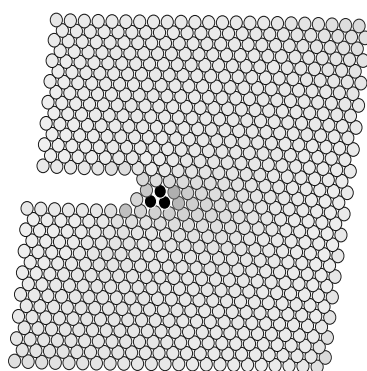


(a)

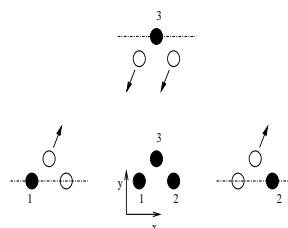


(b)

Figure 5.3: Unstable modes of atoms in the Mode-I crack. Atom 2 right at the crack tip had a longitudinal instability mode; atoms 1 and 4 were unstable by mixed modes; and atom 3 was unstable due to a shear mode. Crack would grow by breaking bonds at atom 2; meanwhile dislocations could form from the unstable region.

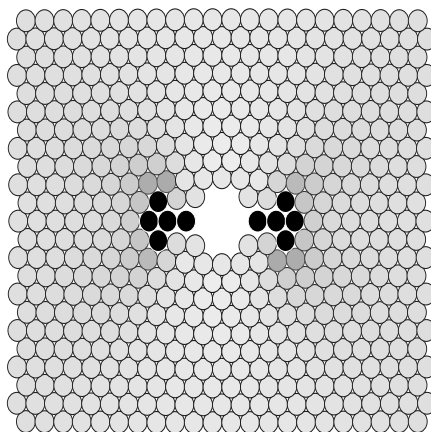


(a)

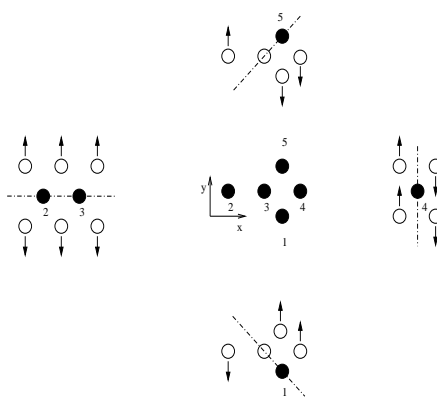


(b)

Figure 5.4: Unstable modes of atoms in the Mode-II crack.

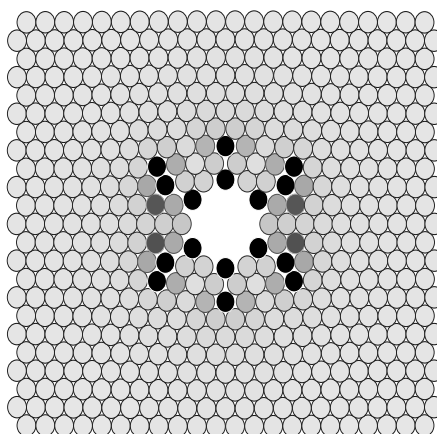


(a)

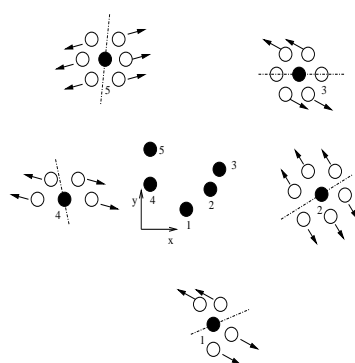


(b)

Figure 5.5: Unstable modes of atoms in the uniaxially stretched void.



(a)



(b)

Figure 5.6: Unstable modes of atoms in the biaxially stretched void.

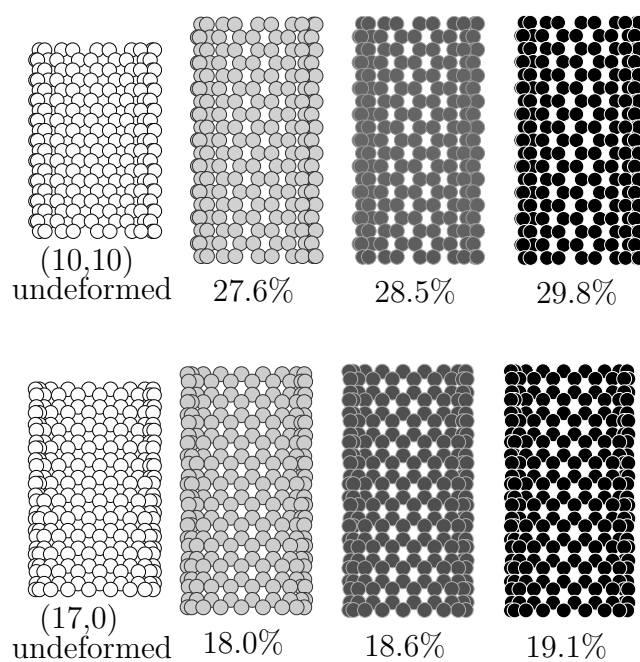


Figure 5.7: Perfect carbon nanotubes (10,10) and (17,0) were stretched axially. The deformed states in equilibrium were calculated by the molecular mechanics method. Atomic acoustic tensor $\bar{Q}_a(\mathbf{n})$ and its smallest eigenvalue were obtained and depicted: the darkest circles represents unstable sites. Nanotubes showed uniform deformation in a long period till critical strains, 27% and 18% for armchair and zigzag type respectively, which are very close to the prediction in reference by Dumitrica et al. As characterized by \bar{Q}_a , instability arrives quickly after critical strains.

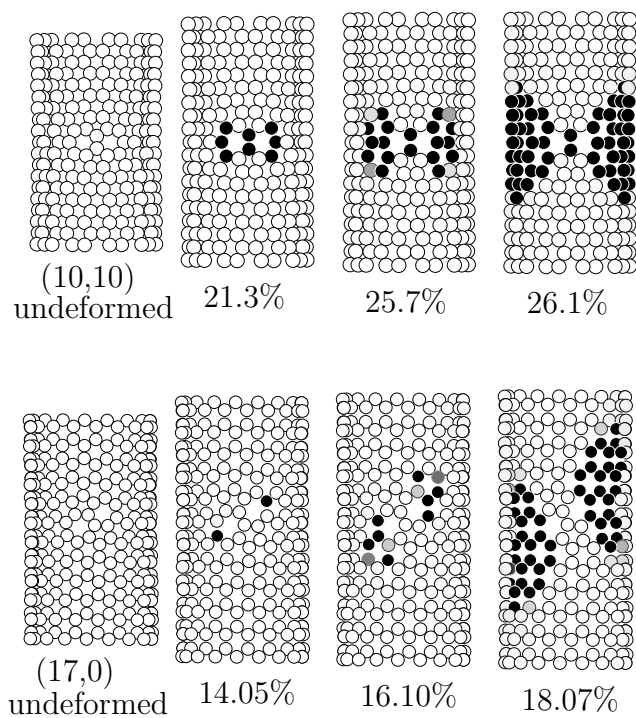


Figure 5.8: the Stone-Wales defect in carbon nanotubes.

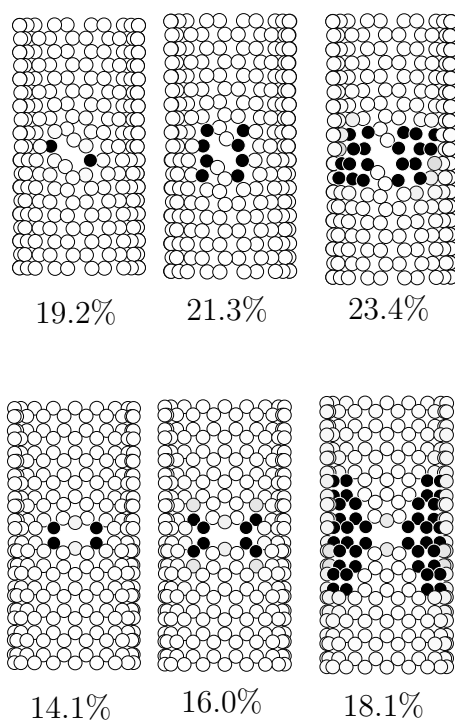


Figure 5.9: Microcrack in carbon nanotubes.

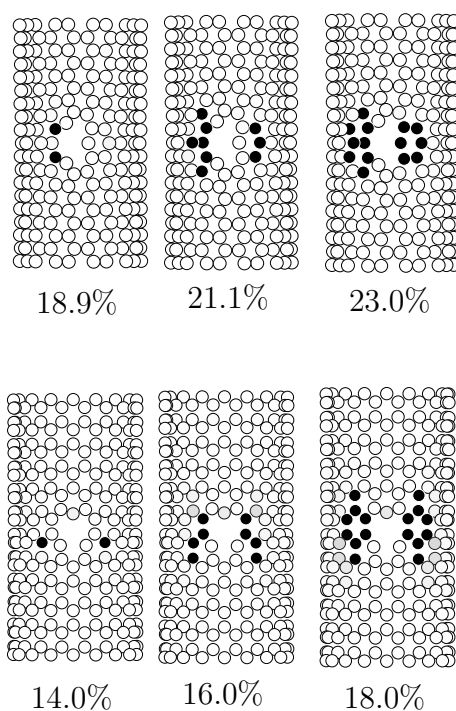


Figure 5.10: A non-reconstructed vacancy in carbon nanotubes.

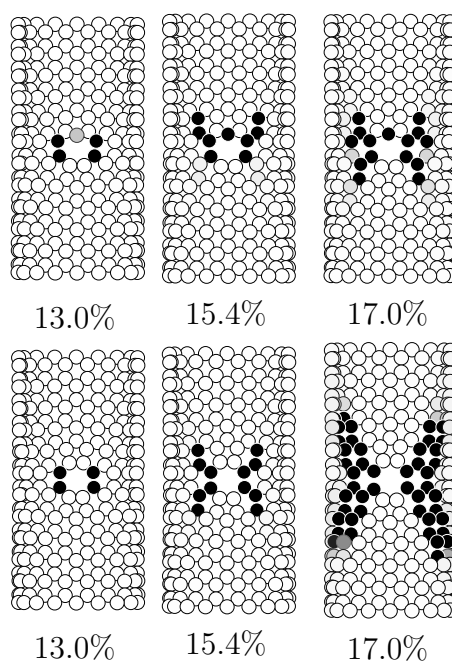


Figure 5.11: Evolution of unstable zone in the (17,0) tube with symmetric one-atom vacancy (upper row) and two-atom vacancy (lower row).

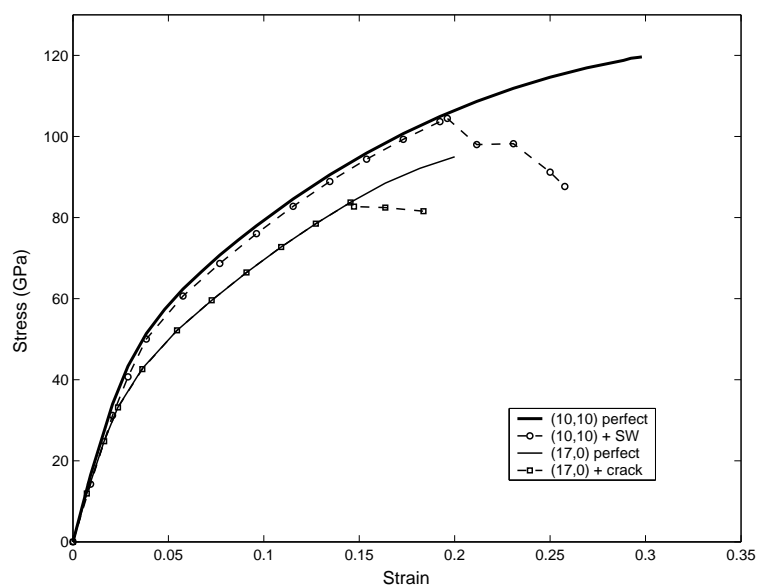


Figure 5.12: Strain-stress curves of pristine and defective CNTs.

Table 5.3: Tensile failure strain of pristine CNTs.

Critical Tensile Strains of pristine SWCNTs				
Tube type	Defect	$\varepsilon_{crit}(\%)$	Method	Reference
(17,0)	pristine	19.1	MM (TB-G1)	present
(10,0)	pristine	16.0	QM-DFT	[85]
(10,0)	pristine	20.0	QM-PM3	[44]
(10,0)	pristine	18.1	MD (MTB-G2)	[87]
(10,10)	pristine	29.8	MM (TB-G1)	present
(5,5)	pristine	27.9	QM-MSINDO	[90]
(5,5)	pristine	30.0	QM-DFT	[44]
(5,5)	pristine	29.7	MD (MTB-G2)	[87]

Table 5.4: Tensile failure strain of defective CNTs.

Critical Tensile Strains of defective SWCNTs				
Tube type	Defect	$\varepsilon_{crit}(\%)$	Method	Reference
(17,0)	SW	14.1	MM (TB-G1)	present
(17,0)	crack	14.0	MM (TB-G1)	present
(10,0)	SW	13.9	QM-PM3	[44]
(10,0)	vacancy	13.0	QM-PM3	[44]
(10,10)	SW	21.3	MM (TB-G1)	present
(10,10)	crack	19.5	MM (TB-G1)	present
(5,5)	SW	24.4	QM-MSINDO	[90]
(5,5)	SW	22.0	QM-PM3	[44]
(5,5)	vacancy	15.3	QM-PM3	[44]
(4,4)	vacancy	21.0	Tight-binding	[41]

CHAPTER 6 CRACK GROWTH IN BRITTLE FRACTURE

6.1 Introduction

The research on the fracture of nanoscale structures becomes more and more important because of recent advances in the application of nano-devices and nano-materials. The failure analysis at nanometer scale is useful in the design of such tiny machines. However, traditional fracture mechanics based on continuum theory cannot be directly applied at the atomic scale.

The linear elastic fracture mechanics (LEFM) in general cannot accurately characterize the rupture of atomic structures. The Stress Intensity Factor (SIF) is a significant quantity in LEFM, and usually evaluated by the analytical elastic solution around crack tips (e.g. Westergaard complex function method [91]). SIF determines the stress field near crack tips and depends on loading modes, geometry of the specimen, and crack length. For discrete atomic systems, however, SIF is not available since there is no such an elastic field as a continuum. Alternatively, the energy-based Griffith's criterion is often used in analyzing crack growth. Irwin[92] showed the equivalence of LEFM and Griffith's theory. In linear elasticity, SIF has a particular correspondence with the energy release rate. In an atomic system, SIF does not exist, and the energy release rate is available only in a quantized sense [93].

As a macroscopic average of local energetics, the energy-based Griffith's method meets other problems at the limit of atomic spacing. Firstly, Barenblatt

suggested [26] that Griffith's method was indeed not right in describing crack tip configuration. In detail, the magnitude of the radius of curvature at the end of blunt-cracks is of the order of intermolecular distance. However, in the framework of continuum theory, the interatomic distance cannot be considered as a finite value. Secondly, "lattice trapping" effect challenges Griffith's criterion. It was found in reference [94] that the discreteness of the lattice causes the crack to remain stable and not to advance until loads larger than the Griffith critical load. Gumbsch [95] pointed out that the increase in surface energy upon crack extension from one bond to the next would not be characterized by a linear increase as the Griffith's criterion does, instead, by a nonlinear oscillating function defined over the bond distance. As a matter of fact, the breaking of chemical bonds is a highly nonlinear and complex process. Therefore, Griffith's criterion is a coarse approximation on the continuum level and may not be accurate for discrete atomic structures.

In addition, an important common drawback of LEFM and Griffith's method relates to the famous paradox. On the one hand, according to elasticity theory, the presence of the singularity in the stress field around crack tips indicates that no matter how small the crack is, an infinitesimal load may induce material failure at the crack tip, whereas cracks under loads do exist. On the other hand, for a body with a crack of infinitesimal length, these two both predict an infinite load at failure, but any material has a certain strength limit even though it is defect free.

Barenblatt [26] introduced the forces of cohesion between molecules near

crack tips and eliminated the stress singularity therein. To address that paradox, Barenblatt suggested that LEFM did not include all forces acting on the body, and the molecular forces of cohesion acting near crack tips should be considered. Instead of a sharp cut or a round end, he proposed the crack surface near tips appeared as a cusp, and the opposite faces of cracks closed smoothly at the tip. According to elasticity theory, the internal cohesive forces acting on the crack surface near tips generate an additional auxiliary stress field which cancels the stress field due to external loads and makes the overall SIF vanish at the crack tip. Therefore, the stress at crack tips remains finite and the singularity can be removed. Moreover, Barenblatt introduced the concept of equilibrium cracks and claimed that, “cracks actually may be stable so that the beginning of crack development is not necessarily connected with the fracture of a body...”. The contribution of Barenblatt first explicitly introduced inter-molecular cohesive forces in fracture mechanics, and provided a reasonable description on the stress field near crack tips and the shape of crack tips.

However, most of cohesive zone models motivated [96, 97, 98, 98, 99, 100] are different from Barenblatt’s model in that they define the traction acting on the ligament as a function of the crack opening distance (COD), not of the distance from crack tip as Barenblatt suggested. In general, the distribution of cohesive forces over the crack surface is unknown. Hence, a traction-separation law is usually defined as cohesive force v.s. COD. In the prescribed cohesive zone (or cohesive elements in FEM), crack appears and grows when the COD approaches the critical value. Many separation laws under stretch and shear states have been

proposed [96, 97, 98]. While they have been widely used in simulations, it should be noted that a one-dimension force-distance law cannot accurately characterize the response of material elements in complex stressed state. In addition, a prerequisite of those cohesive methods is the second assumption in Barenblatt's theory [26], which said the edge region moves as if it had a motion of translation, and the form of its normal section remains unchanged when a crack expands. Current cohesive zone models are valid only if the assumption holds; otherwise, the critical separation cannot be definitely determined when the configuration of crack tip is various.

In this chapter, we aim to evaluate Barenblatt's fracture theory by the atomic stability theory and atomistic simulation. We interpret crack growth and fracture in terms of instabilities: crack growth is controlled by local instability till global instability occurs as fracture. For a cracked body, the stress always concentrates at the crack tip under external loads. Triggered by high stresses, the bond structure in the local region around crack tips may reorganize to release the excessive stress and strain energy. Crack growth and dislocation emission may occur. These microstructural variations are local events and induced by the local instability that does not necessarily cause a global failure. In other words, locally concentrated stresses (or interatomic forces) would in general affect only the local region. After the local region alters and excessive strain energy is dissipated, the whole system can reach another equilibrium, and is still able to sustain further loading. Thus, in this case, the crack at equilibrium is stable. This state is called a metastable state of equilibrium in thermodynamics [101] and must be

a local minimum of total potential in the system with a certain size of crack. As loads increasing, the loss of the local minimum corresponds to the limit of the metastability, which is called a *spinodal*, and also corresponds to the failure threshold. At the limit instant, any local variation in microstructure, except for complete rupture, cannot relax the whole system, and then the global instability appears.

We have proposed an atomic level material stability theory and distinguished local instability and global instability in Chapter 2 and Chapter 5. The singularity of atomic acoustic tensor defined in the stability criterion appears to be able to capture material failure at the atomic scale. The atomic stability condition is directly constructed on the atomistic theory and thus applicable to inhomogeneous systems. In Chapter 5, the bond structure is assumed fixed. No topological change is allowed previously, which is not realistic because local instability may cause local bond reconstruction. In this chapter, we combine the local atomic instability condition and certain bond-breaking algorithm, simulate quasi-static growth of cracks, investigate the equilibrium of cracks, and explore the atomistic foundation of Barenbaltt's fracture theory in such aspects as the presence and the shape of cohesive zone, and the location of crack tip.

6.2 Local atomic instability and bond-breaking algorithm

6.2.1 The atomic acoustic tensor

In Chapter 5, we have introduced an atomic level material stability theory in which the atomic acoustic tensor (AAT) is defined for detecting material failure at the atomic scale. In brief, for an atomic system characterized by interatomic potential $E(r)$, a function of bond length, the force acting on atom a from atom b is in Eq.(5.21) as

$$\mathbf{f}_{ab} = \frac{\partial E}{\partial \mathbf{r}_{ab}}.$$

We define the atomic acoustic tensor in the sense of force as (5.28)

$$\mathbf{Q}_a(\mathbf{n}) = \sum_{b \neq a} \sum_{c \neq d} (\mathbf{r}_{ab} \cdot \mathbf{n}) \frac{\partial \mathbf{f}_{ab}}{\partial \mathbf{r}_{cd}} (\mathbf{r}_{cd} \cdot \mathbf{n}).$$

If $\mathbf{Q}_a(\mathbf{n})$ is singular, i.e. with zero eigenvalues, at some orientation \mathbf{n} , we claim the associated atom is unstable, and the incremental atomic traction in \mathbf{n} direction vanishes. We refer to Chapter 5 for detailed discussion.

Barenblatt [26] proposed that the crack starts expanding only upon reaching the highest possible force of cohesion on the crack contour. In other words, at crack tips, the cohesive force should reach its maximum. The local instability with the singularity of AAT has proved to be able to capture the local softening point in an averaged sense. Therefore, in computation we use AAT to decide the location of crack tip, at which atoms are unstable and chemical bonds are unable to sustain load increases. To decide which bond to be broken, strictly speaking, quantum mechanical analysis should be performed. For simplicity, the bond connecting two

unstable atoms is assumed to be broken.

Klein and Gao [32] first made use of the loss of rank-one convexity as a condition of crack initiation and growth in the VIB model. Motivated by this, we employ the atomic acoustic tensor as an indicator for detecting bond breaking. As a quasicontinuum model, VIB only can be applied for locally homogeneous solids. In contrast, the local atomic instability theory does not rely on the pristine lattice structure and can be used to analyze inhomogeneous systems.

6.2.2 Computational method and bond-breaking algorithm

We have applied the atomic finite element method introduced in Chapter 4 for simulating the deformation and analyzing local instabilities of atomic systems in Chapter 5 where no bond reconstruction is introduced. In this chapter, we allow changes of bond structure. The algorithm is as follows.

- (1). Setup "nodes" (atoms) connectivity and obtain the "mesh" (bond structure);
- (2). Impose loads and boundary conditions;
- (3). Solve FEM equations and get the equilibrium configuration;
- (4). Evaluate the atomic acoustic tensor of atoms in the interested region; if AAT is singular, the atom is labeled unstable, then the bond connecting two unstable atoms is considered unstable and recorded in a bond list;
- (5). Remove bonds in the unstable bond list, update the connectivity and mesh, then go back to (3) until the unstable bond list is empty;
- (6). Increase loads, and repeat (3), (4), (5) until no equilibrium state can be found

in (3).

6.3 Results and discussions

6.3.1 Equilibrium cracks in atomic structures

We use molecular mechanics method and the atomic level stability theory to simulate crack initiation and growth, and explore the validity of Barenblatt's theory [26] of equilibrium cracks at the atomic scale. The body is assumed to be perfectly brittle, i.e. to retain elastic properties up to fracture, and no plastic behavior is considered.

We have discussed that the growth of a stable equilibrium crack is associated with local instability and the rupture corresponds to global instability. In the following, we utilize the singularity of atomic acoustic tensor to capture the instant of crack growth controlled by local instability. In the quasi-static computation, the global instability is determined by the loss of local minimum of the total energy (no convergence). To save computation, we analyzed only atoms around the crack tip, and drew atoms in different colors determined by scaling the minimum eigenvalue of the atomic acoustic tensor. (Red atoms are unstable.) The algorithm in section 6.2.2 was applied to update the geometry and proceed calculation.

We firstly performed analysis on a mode-I crack embedded in a 2-D atomic sheet with triangular lattices. Figure 6.1(e) shows the stretch-force curve. The kinks marked by arrow A, B, C, and D indicates reconstructing bond connectivity at the crack tip under certain load, which relaxes excessive stresses therein and enlarges crack length. When the crack reaches its equilibrium shape, the curve

goes up again under increasing loads till a next dropping. It read that equilibrium cracks in Figures 6.1(a), 6.1(b), and 6.1(c) were stable. At the arrow D associated with crack 6.1(d), the static calculation didn't converge, i.e. no local minimum could be found; then, global instability occurred, and the structure was to rupture. An advantage of applying the local instability condition is the ability to identify the location of crack tip. Barrenblatt pointed out that the crack starts expanding only upon reaching the highest possible intensity of cohesive forces at the tip. This critical state can be captured by the atomic acoustic tensor. We can find the trajectory of the crack tip. As an indicator, the atomic acoustic tensor can highlight the unstable atomic cluster which contains the moving crack tip.

We analyzed a mode-II crack by shearing the 2-D sheet as shown in Figure 6.2. The crack tip could be tracked too. But we found the shearing crack tended to be unstable, i.e. difficult to reach a stable equilibrium. We also altered the loading condition and generated a complex deformation on the 2-D sheet. Thus, a mixed mode crack appeared. Figure 6.3 shows the propagation direction does not follow the pre-existing crack orientation. Initially, unstable atoms located at two regions as in Figure 6.3(a). Then, the crack nucleated at the lower side (see Fig. 6.3(b)) and grew further. The location where the crack initiates depends on the particular shape of the prescribed blunt-crack tip. Crack-tip configurations appear to have a strong effect on brittle cleavage. In future works, we will explore the influence of different blunt shapes of crack-tip.

A weakness of using the local instability condition is that the unstable weakly-interacting bonds cannot be cut. As shown in Figure 6.1 and 6.3, the

bond, whose initial length is greater than the value of inflection point of Morse potential, does not affect the stability of atoms it connects. It is because the local instability condition presents the stability of atomic interactions in an averaged sense. When the long range interaction is weak, it cannot be identified by the averaged quantity, namely the atomic acoustic tensor. To improve this deficiency and display a more realistic fracture picture, we suggest to combine the cutoff criterion and the local instability criterion.

We use the atomic acoustic tensor to control short range interaction, and remove bonds when associated atoms became unstable; Meanwhile, we use cutoff distance to terminate those post-inflection bonds. Figures in 6.4 demonstrate the mode-I crack propagation obtained by using the combined criterion. The bond of length beyond cutoff distance, 2 times of the equilibrium bond length, was supposed to be broken. It was found that the crack tip and a cohesive zone could be clearly identified by using this combined condition. In particular, after a crack initiates, in Figures 6.4(b) ~ 6.4(f), the width and shape of the edge region over which cohesion forces act were nearly identical. These characteristics agree nicely with the second assumption of Barenblatt in ref. [26]. This assumption is important because it is the theoretical foundation of current cohesive zone models. Only if the shapes of the edge region do not differ remarkably, the crack opening criterion based on the distance between opposite crack surfaces, instead of the distribution of cohesive forces over the edge region, is valid. The present study provided simulation results that support this assumption.

6.3.2 Brittle fracture of carbon nanotubes

In Chapter 5, we have applied the local instability criterion to analyze the failure of carbon nanotubes and predict strain limits of defective tubes. A drawback of the work was that the carbon-carbon bonds were assumed unalterable no matter how large the distortion was. In reality, locally concentrated stresses induce bond reconfiguration and defects. In an inhomogeneous system, topological defects may also develop under external loads. At lower temperature, bond breaking is the principal mechanism of defects' evolution in carbon nanotubes. We utilize a slightly different criterion for bond breaking on CNTs. Similar to the de-bonding criterion in 6.2.2, we still remove the carbon-carbon bond connecting two unstable atoms. However, to avoid the appearance of isolated atoms (without connection with any other atoms), we remain the bond with which only one atom connects. In the sequel, we simulate quasi-static fracture of nanotubes at the presence of defects, e.g. Stone-Wales dislocation and reconstructed vacancies.

Stone-Wales defects weaken the strength and deformability of carbon nanotubes, disturb the uniform hexagonal geometry, and become a nucleation core of micro-cracks. After introducing the bond breaking mechanism, the development of SW defect into cracks was simulated as shown in Figures 6.5. Once the cracks nucleated, it grew quickly till rupture. In the quasi-static simulation, no equilibrium cracks were observed. The fracture of CNTs were quite brittle. The same brittleness was found in both armchair (10,10) and zigzag (17,0) tubes. Without special condition like high temperatures, SW defects are more likely to generate micro-cracks instead of a propagating dislocation. The brittleness of fracture was

also observed in MD simulation performed in reference [43].

Regarding the path on which cracks develop, the most vulnerable locations occur on two outer sides of heptagon rings but not the axial bond linking two pentagons. The length of unstable C-C bond in the perfect armchair tube were found around 1.72 Å and 1.64 Å in perfect zigzag tube. For the armchair tube with SW defect in Figure 6.5(a), C-C bonds linking unstable atoms in heptagons that were 1.6792 Å long while the central bond connecting two pentagons was 1.6106 Å long. Those outer side bonds firstly approached limit rather than the rotated C-C bond that links two pentagons. The nucleation mechanism of SW defects indicates that C-C bond rotates a 90 degree such that a 5/7/7/5 dislocation core replace hexagons, and excessive strain energy is released because the rotated bond is less stretched compared to other bonds in the hexagonal structure. Thus, the rotated bond becomes more stable (further apart from the limit length). For the zigzag tube with SW defect in Figure 6.6, the similar phenomenon was observed. In detail, outer bonds in heptagons were 1.6481 Å which is precisely the maximum length for perfect zigzag tube. The central bond has length of 1.4944 Å far less than the critical value. In both armchair tube and zigzag tube, moreover, the rotated central bond broke quickly after cracks initiate at outer heptagons because it could not sustain additional loads generated when removing out the side bonds. Therefore, for a SW defect, the rotated bond in the center of 5/7/7/5 core was more stable than outer heptagon bonds connecting other hexagons; cracks usually appeared at outer sides of heptagons, and the rotated central bond broke afterwards.

We also investigated the development of vacancies on nanotubes. Figure 6.7 shows the (17,0) zigzag tube containing a reconstructed vacancy with one carbon atom missing. The symmetric reconstructed configuration includes a larger polygonal defect core which behaves like a small crack. The crack tips were highlighted by the unstable couple of atoms in 6.7(a). Once unstable C-C bonds were removed, no equilibrium cracked configuration existed and the crack propagated along the original crack surface till rupture. Under axial loading, the crack was mode-I. The symmetric reconstructed vacancy with 2 missing atoms in Figure 6.8 also developed into a mode-I crack whose orientation was perpendicular to the tube axis. Those reconstructed bonds in symmetric vacancies became stable because they were not aligned in the loading direction.

Finally, we performed analysis on a (10,10) armchair carbon nanotube with vacancies. For armchair tubes, reconstructed vacancies do not have the symmetry relative to tube axis. Figures 6.9 and 6.10 show two types of reconstructed vacancy with one missing atom. The first type in Figure 6.9 is completely asymmetric while the second type in Figure 6.10 possesses symmetry relative to the hoop direction. Neither of these two has axial symmetry as those in zigzag tubes. For the vacancy with one missing atom, the stability of the reconstructed C-C bond in armchair tube is slightly complex. For type-1, the unstable bond was not the reconstructed one that is nearly perpendicular to tube axis, but the one more closely aligned along tube axis; whereas for type-2, the reconstructed bond was parallel to the loading direction, thus it was more vulnerable and turned unstable firstly. Moreover, the propagation path of cracks in these two cases are different too. After the most

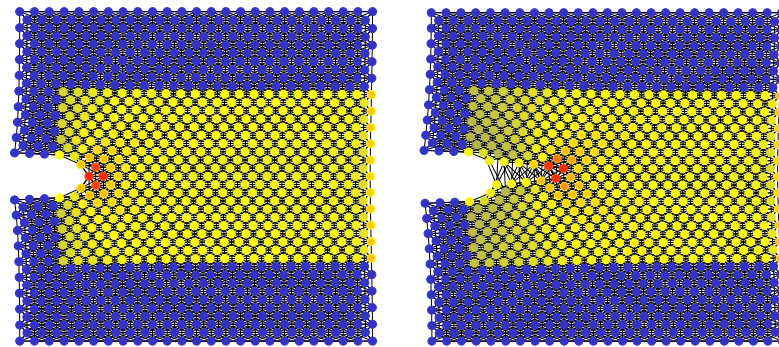
vulnerable bond broke, type-1 vacancy became symmetric, and at each tip the crack bifurcated into two paths as shown in Figure 6.9(c). Then, the tube ruptured with bifurcated cracks. The type-2 became a non-reconstructed vacancy in Figure 6.10(b) after the reconstructed bond broke, and then, a crack not perpendicular to the tube axis appeared. It is because the bonds sustaining loads in armchair tubes are not parallel to tube axis as those in zigzag tubes. When the bond breaks, the surface of generated cracks is usually not perpendicular to the axis. The resulting crack is a mixed mode.

6.3.3 Discussions

In this chapter, we applied the atomic acoustic tensor proposed in Chapter 5 as an indicator of bond breaking, analyzed the development of defects in metallic crystals and carbon nanotubes, and simulated quasi-static crack propagation in these nanoscale structures. The atomic acoustic tensor is used to identify the crack tip, and link the atomic level instability and the material failure in macroscale. Together with assumed bond breaking criteria, the simulation turns to be able to investigate the development of defects in inhomogeneous atomic systems.

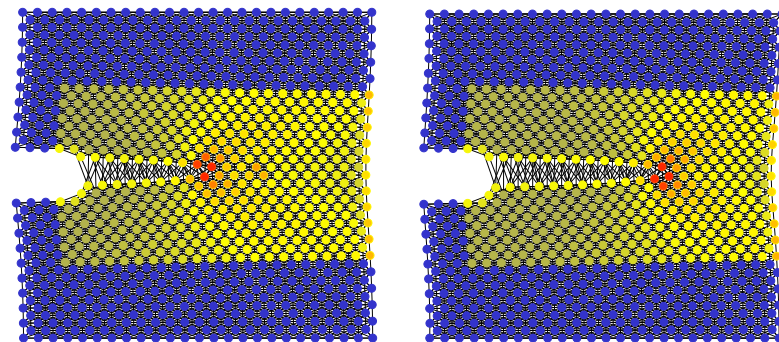
Strictly speaking, the mechanism of bond breaking cannot be thoroughly analyzed under the empirical framework. Most empirical interatomic potentials are unable to describe bond breaking or bond reconstruction. The stability of chemical bond cannot be predicted precisely by empirical methods either. To do these, quantum mechanical analysis is necessary. Although the predictability of empirical potential is limited, the atomic acoustic tensor is still useful and can be

employed as an indicator for detecting unstable responses, and signaling the switch over from empirical method to more accurate quantum analysis in a multiscale framework.



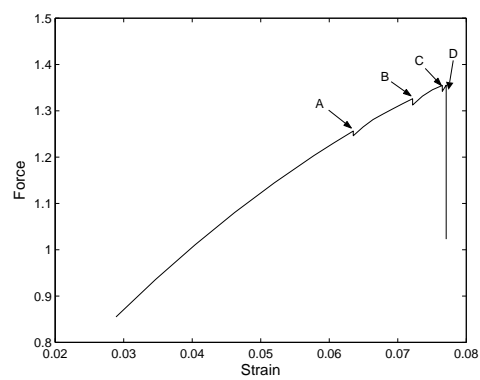
(a) A

(b) B



(c) C

(d) D



(e) Stretch-force curve

Figure 6.1: Propagation of a mode-I crack determined by local instability condition.

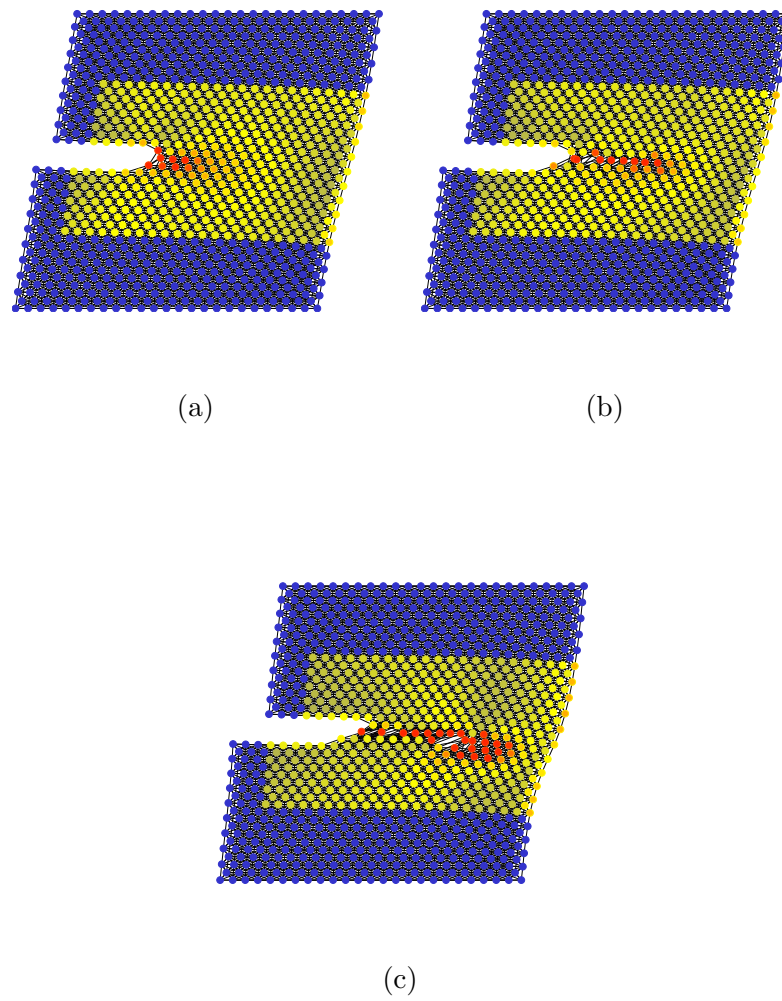


Figure 6.2: Propagation of a mode-II crack determined by local instability condition.

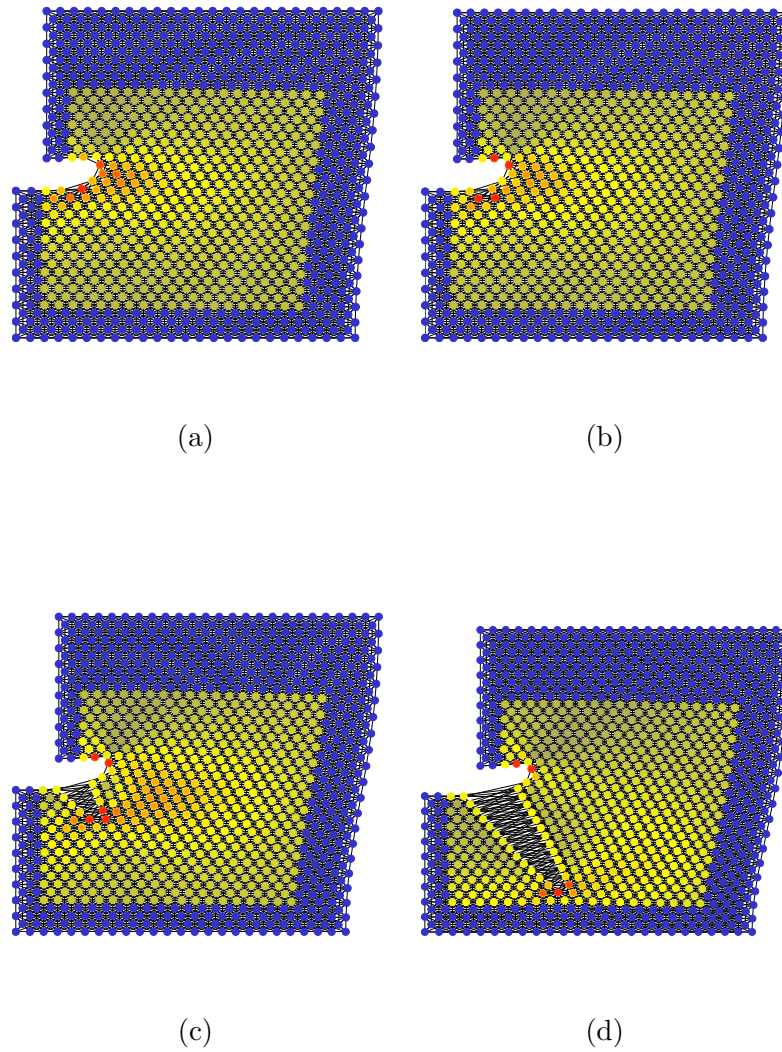


Figure 6.3: Propagation of a mixed mode crack determined by local instability condition.

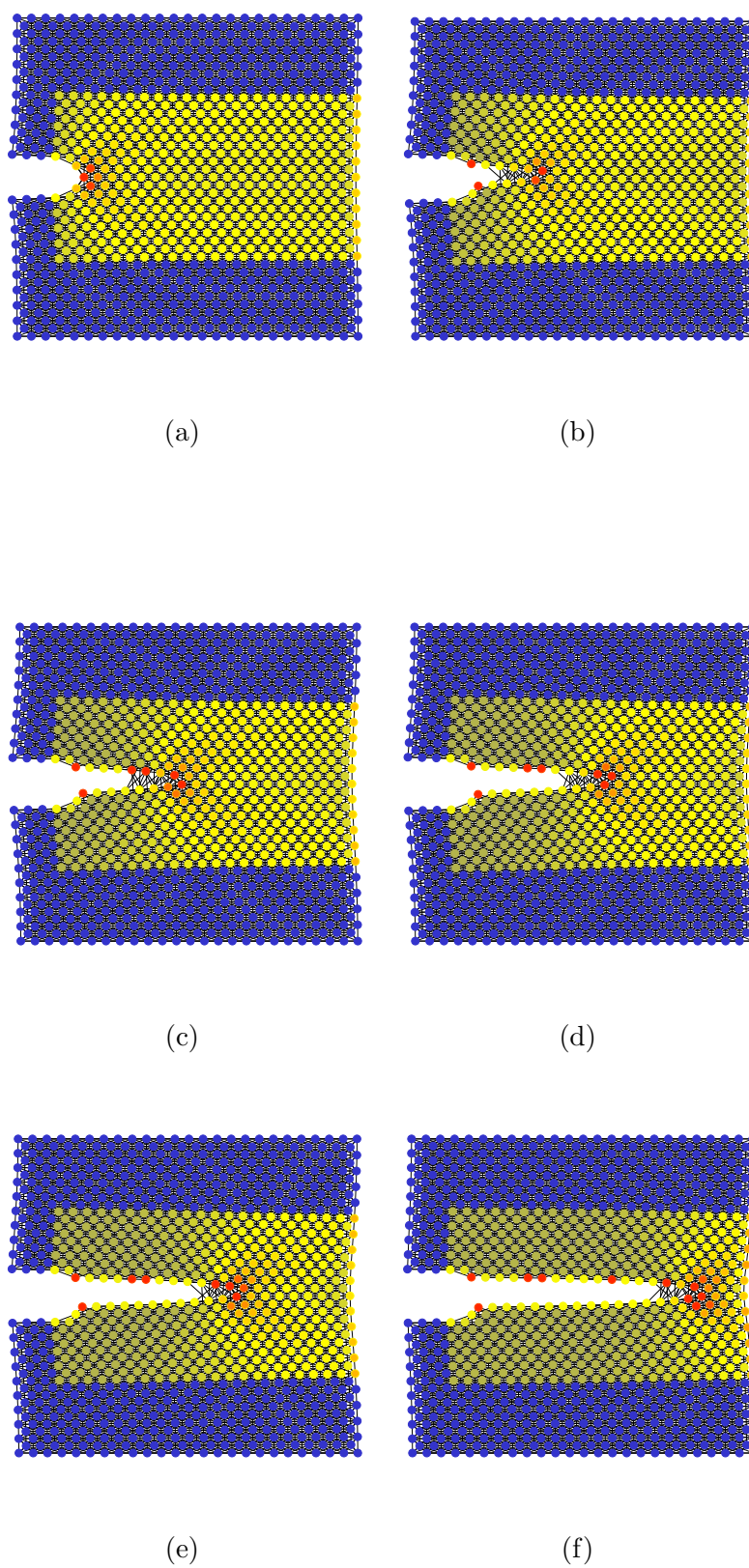


Figure 6.4: Propagation of a mode-I crack determined by combining the local instability condition and the cutoff condition.

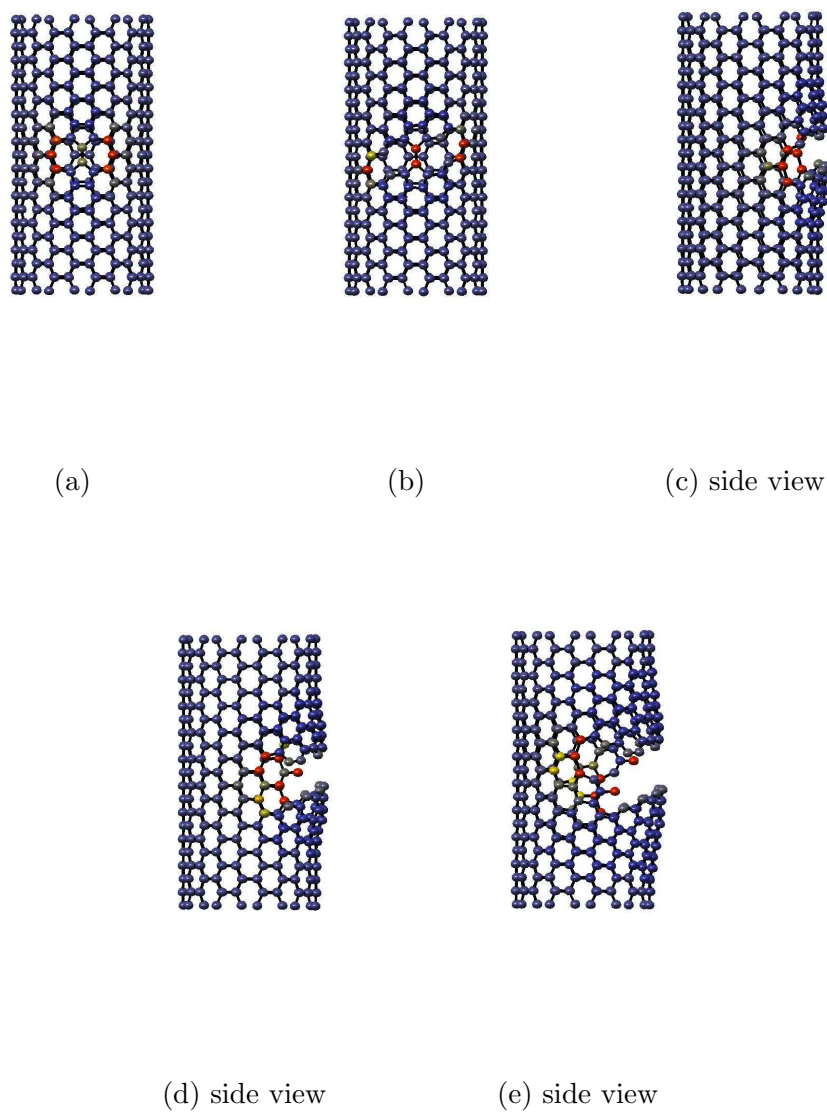


Figure 6.5: Development of Stone-Wales defect in armchair carbon nanotube.

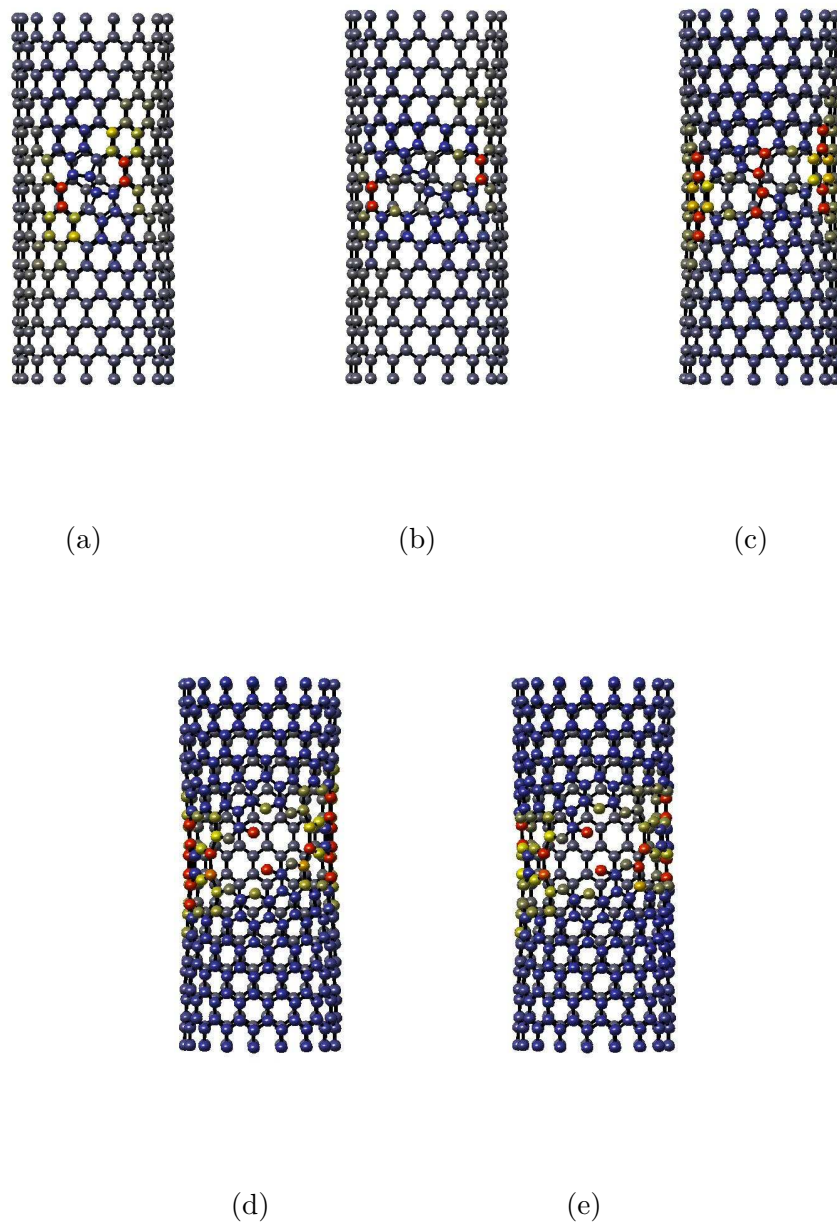


Figure 6.6: Development of Stone-Wales defect in zigzag carbon nanotube.

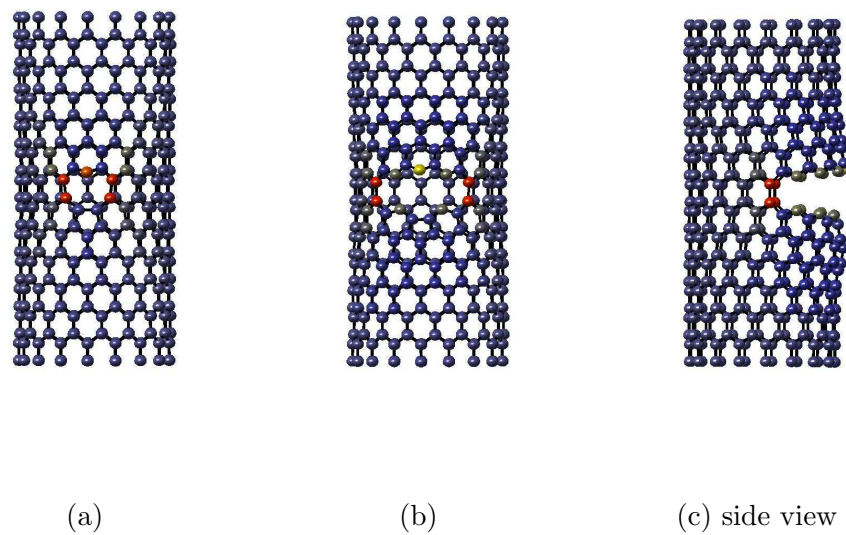


Figure 6.7: Development of reconstructed vacancy with one atom missing in zigzag carbon nanotube.

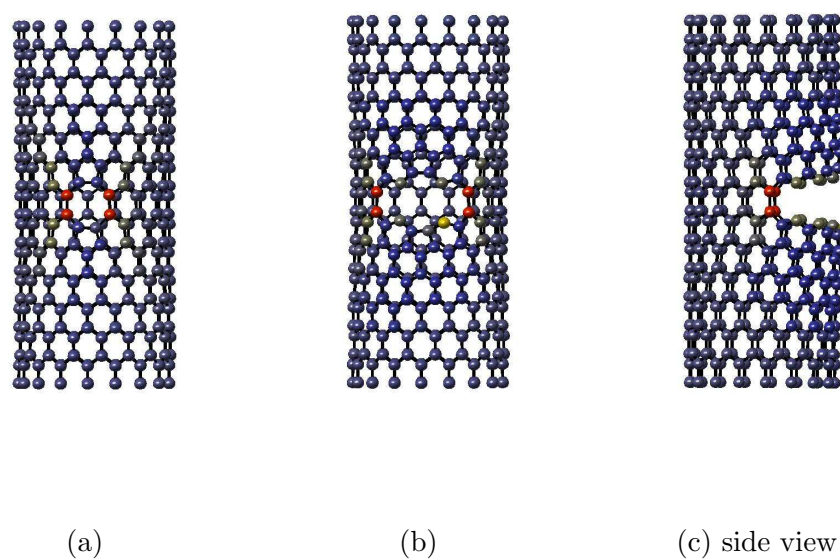


Figure 6.8: Development of reconstructed vacancy with two atoms missing in zigzag carbon nanotube.

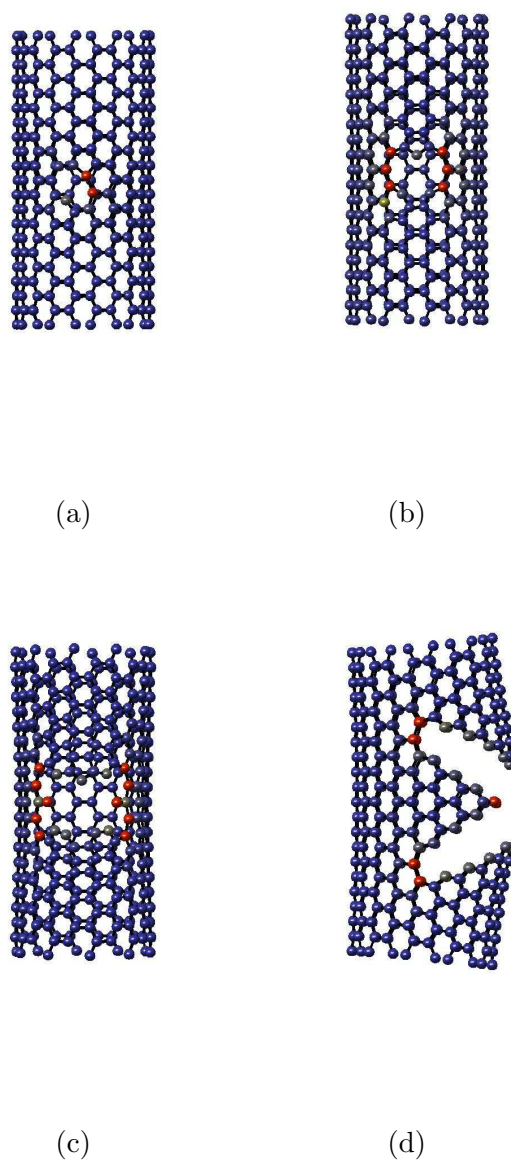
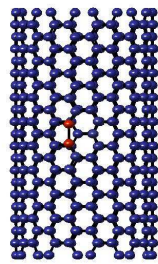
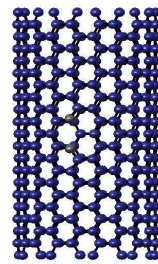


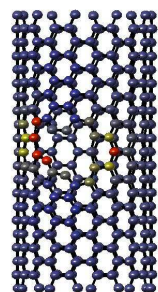
Figure 6.9: Development of type-I reconstructed vacancy with one atom missing in armchair carbon nanotube.



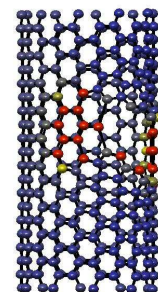
(a)



(b)



(c)



(d) side view

Figure 6.10: Development of type-II reconstructed vacancy with one atom missing in armchair carbon nanotube.

CHAPTER 7 DEFECT ENERGETICS IN CARBON NANOTUBES

7.1 Introduction

Many promising applications of CNTs have been suggested, such as the use as reinforcing materials for high-strength light-weight composites, and as the building blocks and functional components for nano-devices. Moreover, perfect armchair nanotubes can conduct electricity up to ten times better than copper and weight about one sixth as much at room temperature [102]. The metallic CNTs have been selected to be a candidate of “Quantum Wires” [102]. Some recent works [103, 104, 105] reported that the mechanical deformation and the presence of defects seriously affect the electrical properties of CNTs. So far, the elastic deformation and properties CNTs have been well investigated [106, 58], but a full characterization of their inelastic and defective responses is still lacking.

When loaded beyond a certain limit, carbon nanotubes may respond to mechanical load via the formation of topological defects [52, 88]. In a stretched CNT, a fundamental defect appears via a 90° rotation of a C-C bond from predominately transverse direction to predominately axial direction. This transition, known as the Stone-Wales (SW) transformation [107], preserves the threefold sp^2 bond structure but replaces the hexagon rings with two pentagon-heptagon (5-7-7-5) pairs as indicated in Figure 7.2. At large stretches the bond rotation releases the excessive strain [52, 88] and results in an energetically favorable state. Recent studies reported that the SW defect can significantly reduce the limit strain of

carbon nanotube [108, 109, 51, 90, 44], and also affects the electrical properties of CNTs [110, 103, 104].

The energy barrier affects the rate of SW transformation. Recently, it has been found that the energy barrier of Stone-Wales transition is noticeably high such that at room temperature the SW transition unlikely occurs and SW defects do not tend to propagate [111, 52, 51, 112]. Due to the high barrier, the bond reconfiguration is too rare to be observed, and thus, the Stone-Wales transition is inactive at the room temperature. The presence of SW defects weakens the local stiffness [86] and presents potential sites for crack nucleation. At high temperatures, further relaxation through successive SW rotations at neighboring bonds becomes possible [113]. In this case, the SW transition provides the mechanism of “intramolecular plasticity” [89, 52, 88].

While the energy barrier determines the kinetic stability of SW transformation, the *formation energy*, namely the energy difference between defective and maiden states, is also a significant energetic quantity that reflects the tendency and the thermodynamical stability of the transformation [114, 52, 88, 89, 113, 115, 116, 117, 118, 119]. Firstly, for a transition being energetically favorable, the formation energy must be less than zero, i.e. the defective state must rest at a lower energy level. Hence, a negative formation energy is the necessary condition for defect formation, and is also the thermodynamical driving force for the transformation. Secondly, the magnitude of formation energy also affects the thermodynamical stability of the post-transition system. The lower the formation energy, the more stable the defective state, the smaller the possibility of a transition being reversible.

In addition, the formation energy also provides significant information about defect interaction. In [113], the energy of multiple SW defects as function of the relative position was shown to signify the probable directions for defect propagation. Therefore, calculating the formation energy is an important task in energetic analysis.

Ab initio methods are often employed for computing the formation energy of defects. In quantum mechanics computations, the supercell model is a common method using limited number of atoms and assuming periodical boundary condition, for example in refs. [115, 120]. However, assuming the structure to be infinite and periodic as supercell method does, the influence of the interaction between images of defects in different cells is inevitable. Another quantum mechanical approach is the cluster method [116, 85, 117] that considers an isolated patch of atoms. While the cluster calculation avoids the spurious interaction of imaged defects, the size of the atomic cluster is limited due to the computational intensity of quantum mechanics simulations. Consequently, *ab initio* methods are infeasible for structural level energetic analysis, especially when the structure is very large. The formation energy of defects in nanotubes is dependent on the geometry, size, and deformation of the tube. In theory, the potential energy is defined for the whole system. However, presently, it remains prohibitively expensive for *ab initio* methods to simulate a relatively large system in practice.

To overcome this difficulty, molecular dynamics (MD) and molecular mechanics (MM) simulation are good candidates since they are based on empirical atomistic theory. Some MD techniques have been developed to investigate the

structural energetic characteristics of topological defects in nanotubes. It is found that the formation energy calculated by empirical methods can arrive at the same conclusion [119] on the energetic behavior of defects in nanotubes as those obtained by *ab initio* methods [116] with comparably lower computational expense, as long as a proper interatomic potential is employed.

In earlier studies on the energetics of SW defect in CNTs [52, 88], the formation energy is by definition computed as the energy difference of whole tubes. While correct, this approach overlooks an important feature of defect mechanics, that is, the locality of the defect. Stone-Wales transformation is a local phenomenon. The distortion of a 5-7-7-5 ring to its surroundings diminishes rapidly as the distance to the defect increases [111]. Recently, a one-meter long carbon nanotube is under development [102, 105], which is used for power cables. It is still nontrivial to analyze the structural energetics of such a large tube using full configuration calculation in MD.

In this chapter, we present an approximate method for computing the formation energy of the Stone-Wales dislocation in pre-loaded CNTs. Besides the bond reconfiguration in the local defective patch, the remaining structure and the applied load do have energetic influences on the defective system and need to be properly considered. In Section 7.2, a formula for the change of the Gibbs free energy is derived. The relative energy is found to consist of the energy variation in a local defective region and a second order correction that approximates the influence of the remaining system. The formula suggests an efficient way to compute the formation energy in relatively large atomic systems. Instead of computing the global

energetics of the defective system, one only considers an embedded local defective cluster, and takes into account of the remaining system approximately through the correction term. This simplification allows one to readily perform structural level energetic analysis. For example, one can employ the method to compute the “formation energy map”, i.e., formation energy as function of the defect position in non-uniformly deformed CNTs. Likewise, one can study the energetic interaction between multiple defects by embedding new defects in a pre-defective system. With the proposed method, the global solution only needs to be performed once. In section 7.4, the method is utilized to study the SW defects in carbon nanotubes under axial tension and bending. The method itself is sufficiently general, and can be applied to other types of local defect.

7.2 Structural Formation Energy of Stone- Wales Defect

We consider CNTs at low temperatures where the thermal fluctuation is negligibly small and the atomic system remains approximately in a quasi-equilibrium state. The formation of a defect causes a change of the total energy in the system. The difference

$$E_f = \Pi^{(2)} - \Pi^{(1)} \quad (7.1)$$

defines the formation energy, where $\Pi^{(1)}$ and $\Pi^{(2)}$ are the Gibbs free energies of the reference and the defective systems. As alluded earlier, the energy difference should primarily result from the reconfiguration of sp^2 bonds in the defect and its perturbation to the surrounding atoms. Inspired by Eshelby’s method for the

inclusion problem [121] and his approach to defect energetics [122], we propose a local approach for computing the energy difference of the entire system.

Figure 7.1 illustrates the notions used in the localization method. The local cluster D is a small set of atoms in which a 5-7-7-5 dislocation is to be embedded. The atoms in the pristine domain complement to D are denoted by the set P . The interface, denoted by I , includes the atoms in D that have energetic interaction with any atom in P and vice versa. For pairwise interaction, the interface set contains the bonding pairs along the internal boundary. For many-body potentials the interface may extend to a thin layer of atoms. We employ the Brenner bond order potential [24] to model the bond energy. The interface set consists of the atoms on the layer of hexagon rings directly connecting D and P (see Figure 7.1). In addition, we identify the atoms in P that are subject to external load as the boundary set B , which can be further divided into disjoint subsets $B = B_r \cup B_t$ corresponding to displacement and force boundary points.

Consider a reference tube subject to the load

$$\begin{aligned} \mathbf{r}_i^{(1)} &= \bar{\mathbf{r}}_i \quad \text{for atom } i \in B_r \\ \mathbf{t}_i^{(1)} &= \bar{\mathbf{t}}_i \quad \text{for atom } i \in B_t . \end{aligned} \tag{7.2}$$

Let $\mathbf{r}_j^{(1)}$ be the coordinates of atom j at equilibrium. Under the same external load, a defective tube with a SW dipole embedded in D produces a different equilibrium state $\mathbf{r}^{(2)}$. The Gibbs free energies of the reference and the defective tubes are

$$\begin{aligned} \Pi^{(1)} &= E_{P+D}(\mathbf{r}_j^{(1)}) - \sum_{b \in B_t} \bar{\mathbf{t}}_b \cdot \mathbf{r}_b^{(1)} , \\ \Pi^{(2)} &= E_{P+\hat{D}}(\mathbf{r}_j^{(2)}) - \sum_{b \in B_t} \bar{\mathbf{t}}_b \cdot \mathbf{r}_b^{(2)} \end{aligned} \tag{7.3}$$

where \widehat{D} differs from D since defect is inserted. The total interatomic potential consists of the sum of bond energies V_{ij} and can be regrouped into the sum of *site* potentials E_i . We write

$$E_{P+D} = \sum_{i<j} V_{ij} = \sum_{i \in P+D} E_i. \quad (7.4)$$

With Brenner potential and the threefold bond structure, the energy of the site i is

$$E_i = \frac{1}{2} \sum_j V_{ij}, \quad (7.5)$$

with the sum running over the three sp^2 bonds connecting to atom i . The potential of the whole tube can be naturally split into $E_{P+D} = E_P + E_D$ where each term consists of the sum of site energies in the respective region.

For the succeeding development, we introduce an auxiliary configuration $\hat{\mathbf{r}}^{(1)}$ of the defective tube using an imaginary fixing and replacing process: (1) Select a region D that a 5-7-7-5 ring is to be inserted; (2) Fix all the interface atoms; (3) Replace the interior atoms in D with a defective replica. The interior atoms in D do not directly interact with the interior atoms in P and hence, once the interface atoms are fixed, any reconfiguration in D will not induce atomic displacements in P . However, a set of force (called mismatch force) is needed on the interface atoms to keep the them from moving. This imaginary process leads to a configuration

$$\hat{\mathbf{r}}^{(1)} = \begin{cases} \mathbf{r}_i^{(1)} & i \in P \cup I \\ \hat{\mathbf{r}}_d^{(1)} & d \in \widehat{D} \setminus I \end{cases}. \quad (7.6)$$

Imagine that one isolates the local cluster D and keeps it in the deformed state $\mathbf{r}^{(1)}$. To sustain the deformation, one must apply a set of force, denoted by $\mathbf{t}^{(1)}$,

on the interface atoms (this set of force corresponds to the boundary force that D experiences in the reference state $\mathbf{r}^{(1)}$). Likewise, to deform the defective replica \widehat{D} to the auxiliary configuration, one must apply another set of force $\hat{\mathbf{t}}^{(1)}$ on the interface atoms. By equilibrium, the difference $\hat{\mathbf{t}}^{(1)} - \mathbf{t}^{(1)}$ is the interface mismatch force, which is necessary to sustain the configuration $\hat{\mathbf{r}}^{(1)}$ in addition to the original boundary forces that are left intact. If the mismatch force is released, the defective tube will relax to the final configuration $\mathbf{r}^{(2)}$.

With the auxiliary configuration, we can deduce an expression for the formation energy $E_f = \Pi^{(2)} - \Pi^{(1)}$:

$$E_f \approx E_{\widehat{D}}(\hat{\mathbf{r}}_d^{(1)}) - E_D(\mathbf{r}_d^{(1)}) - \frac{1}{2} \sum_{s,t \in I} (\hat{\mathbf{t}}_s^{(1)} - \mathbf{t}_s^{(1)}) \cdot \mathbb{C}_{st} (\hat{\mathbf{t}}_t^{(1)} - \mathbf{t}_t^{(1)}). \quad (7.7)$$

The derivation is given in the Appendix E. Here, \mathbb{C}_{st} is the compliance matrix associated with the interface atoms I evaluated at the auxiliary configuration $\hat{\mathbf{r}}^{(1)}$. The leading term $E_{\widehat{D}}(\hat{\mathbf{r}}_d^{(1)}) - E_D(\mathbf{r}_d^{(1)})$ represents the local energetic variation that gives the first order approximation to the structural formation energy. The remaining term represents the nonlocal effect and provides a second order correction to the formation energy.

Remark 1. Strictly speaking, the method is not a local scheme as the compliance matrix takes into account the structural influence. For defects nucleated in the bulk, if the region D is sufficiently large, the perturbation term in (7.7) can be negligibly small. Then, the formation energy can be reasonably approximated by the local change of potential energy $\approx E_{\widehat{D}}(\hat{\mathbf{r}}_d^{(1)}) - E_D(\mathbf{r}_d^{(1)})$. The computation of the defective system remains purely local. In this case, the atomic cluster method in *ab initio* calculation is appropriate. However, in the structural energetic analysis

of nanotubes, the remaining structure outside the cluster also have energetic influences, and the contribution of the second order term would be large and should not be ignored.

Remark 2. For calculating the compliance matrix, our experience indicates that it can be replaced by the corresponding compliance of the reference tube without causing noticeable difference to the formation energy. This further simplifies the computation. Within the framework of molecular mechanics or molecular dynamics, the compliance matrix of the reference tube can be readily obtained as a by-product of configuration optimization.

7.3 Computational Procedure

The molecular mechanics (MM) method with the implementation proposed in [62] is employed to obtain the equilibrium state of the CNT under loads. The MM calculation is based on the energy minimization with respect to discrete atomic positions. The free energy in the system is

$$\Pi = E(\mathbf{r}_i) - \sum_{k \in B_t} \bar{\mathbf{t}}_k \cdot \mathbf{r}_k \quad (7.8)$$

The first generation Brenner potential [24] is used to model CNT bond energy. The parameters listed as potential-I in [24] are utilized in the computation.

The equilibrium of the atomic system requires that atomic positions make the total potential energy reach its minimum

$$\frac{\partial \Pi}{\partial \mathbf{r}_i} = 0, \quad (7.9)$$

subjected to $\mathbf{r}_i = \bar{\mathbf{r}}$ on B_r . This yields a nonlinear system of $3(N - N_{B_r})$ equations where N is the total number of atoms and N_{B_r} the number of atoms subject

to boundary displacements. To find equilibrium atomic positions, the Newton-Raphson method is employed to solve the equations (7.9). At the k th iteration (configuration), the increments of the atomic coordinates are given by

$$\left[\frac{\partial^2 \Pi}{\partial \mathbf{d} \partial \mathbf{d}} \right] \Big|_{\mathbf{d}^{(k)}} \Delta \mathbf{d}^{(k+1)} = - \frac{\partial \Pi}{\partial \mathbf{d}} \Big|_{\mathbf{d}^{(k)}}, \quad (7.10)$$

where

$$\mathbb{K} := \frac{\partial^2 \Pi}{\partial \mathbf{d} \partial \mathbf{d}}$$

is the tangent stiffness matrix (the Hessian), \mathbf{d} is the vector of atomic displacements. The system (7.10) is solved iteratively till convergence is achieved.

At convergence we partition the stiffness matrix \mathbb{K} into

$$\mathbb{K} = \begin{bmatrix} \mathbb{K}_{ss} & \mathbb{K}_{sd} \\ \mathbb{K}_{ds} & \mathbb{K}_{dd} \end{bmatrix}, \quad (7.11)$$

where s stands for the degree of freedoms (DOF) of the interface atoms I , d denotes the remaining DOFs. The compliance matrix \mathbb{C} in (7.7) is computed according to

$$\mathbb{C} = (\mathbb{K}_{ss} - \mathbb{K}_{sd} \mathbb{K}_{dd}^{-1} \mathbb{K}_{sd})^{-1}. \quad (7.12)$$

The procedure for computing the energy difference are summarized below:

1. Compute the equilibrium configuration of the reference tube;
2. At the position where a SW ring is to be inserted, select a local cluster, identify the interface and record the coordinates of the interface atoms;
3. Replace the cluster with a defective replica, solve a local equilibrium problem to compute the atomic coordinates in the replica keeping interface atoms fixed from step 2;

4. Compute the relative energy according to (7.7).

Note that, to compute the energetics of defects as function of position, the global solution needs to be performed only once. This allows one to efficiently compute the defect energetics in a relative large system. If the structure has unconstrained rigid body modes, the tangent stiffness \mathbb{K} is singular and hence the compliance can not be directly computed. In this case, one can augment \mathbb{K} with several rank-one updates $\sum_{\alpha} a_{\alpha} \mathbf{R}_{\alpha} \otimes \mathbf{R}_{\alpha}$ necessary to eliminate the singularity, where a_{α} ($\alpha \leq 6$) are positive scalars and \mathbf{R}_{α} are independent rigid body modes, $\mathbb{K} \mathbf{R}_{\alpha} = \mathbf{0}$. This will not affect the energy computation due to the fact that the matching force $\hat{\mathbf{t}}_t^{(1)} - \mathbf{t}_t^{(1)}$ is self-equilibrium. The proof of this claim is straightforward and is omitted.

7.4 Results and Discussions

7.4.1 Cluster size

The proposed method exists on the premise that, if the size of the local cluster is sufficiently large, the mismatch force should be sufficiently small hence formula (7.7) should provide a second order accurate estimation for the formation energy. For practical purpose, it is of foremost importance to investigate the influence of cluster size on the energy computation. We employed two types of clusters. For large diameter tubes we introduced the layer patch as shown in Figures 7.2(a) and 7.2(b). The pentagon-heptagon ring itself (bold solid line), which possesses 16 atoms, is defined as the layer-0 patch. The region enclosed by dashed lines which has 42 atoms is termed layer-1; the layer-2 region is enveloped by the dotted line.

This type of clusters is consistent with the defect-shell model in [117]. For small diameter tubes, the ring model was introduced. A defective ring is a tube segment that contains a SW defect. Figure 7.2(c) shows the family of hierarchically defined defective rings in a (5,5) armchair tube. The ring-1 corresponds to the segment that just contains a 5-7-7-5 dipole, and the ring-2 extends to two additional layers of atoms, and so on. The corresponding ring models in a (10,0) zigzag are depicted in 7.2(d). Note that, a 5-7-7-5 dipole has three possible orientations in each chirality [117]; here we considered the one in which the pentagon-pentagon axis points predominately to the tube axis.

We considered tubes under axial tension by prescribed end-displacement. A SW defect is inserted in a 5 nm long (10,10) armchair and a 5 nm long (17,0) zigzag. Figures 7.3(a) and 7.3(b) show the values of formation energy obtained using clusters of various sizes. It is seen that, for the (10,10) armchair, the local cluster as small as layer-0 can yield results almost identical to those by the full tube. The high accuracy may be attributed to the relatively minor distortion the SW defect produces in the armchair configuration. In contrast, Figure 7.3(b) shows that the layer-2 cluster is necessary to achieve a comparable accuracy in the (17,0) zigzag owing to the relative large distortion the SW defect produces in a zigzag tube.

The analyses were repeated for the 12 nm long (5,5) armchair and the (10,0) zigzag shown in Figures 7.4(a) and 7.4(b) using the defective ring. Figures 7.3(c) and 7.3(d) present the formulation energy results. For the armchair, the ring-1 and the ring-2 results are almost identical and both are sufficiently accurate

comparing to the full tube computations. On the contrary, for zigzag tube the ring-1 results show a moderately large deviation from the full tube result. The ring-2 cluster seems necessary for an accurate estimation. The formation energies of the SW defect are found to approach zero when the strain is around 6% for armchair tubes and around 12% in zigzag tubes. These values agree nicely with the existing reports [52].

7.4.2 Formation energy map

In a non-uniformly deforming CNT, the defect formation energy depends on the local strain (stress) level and factors such as the distance to the tube boundary. Hence, the spatial distribution of formation energy provides an indicator for potential “weak spot” where a defect transformation is most likely to occur. We applied the method to study the position dependence. We first computed the formation energy distribution in a 12 nm long (5,5) under axial tension. We chose nine locations where a SW dipole was to be inserted. The locations were uniformly placed along the tube length. The formation energies were calculated for these nine locations respectively, assuming a single SW defect appears in the tube for each time. The ring-1 model (see Figures 7.2(c)) was employed. Figure 7.5 presents the formation energy distribution under three levels of strain. Notably, the formation energy possesses a symmetric distribution and attains lowest value in the middle, implying that the defect transformation is most likely to initiate near the middle. Although the reference state is uniform, the formation energy shows a small variation across the tube length due to boundary effect. For a further assessment of the

accuracy, the full tube results are also computed. The approximate results agree well with the full tube computations in most locations except near the ends of the tube where the solutions deviate slightly.

Bending is a common mode of deformation that slender CNTs are likely to sustain in their service. We calculated the formation energies of the 12nm (5,5) armchair in four bended configurations shown in Figure 7.6. Configurations (a) and (b) were obtained by applying a transverse force at the tip; and configurations (c) and (d) were obtained by prescribing end-displacement. Since we were interested in stretch-induced SW rotation, the defect was inserted in the stretched side of the tube. The same nine locations were employed. In configurations (a) and (b), the maximum bending moment occurs at the fixed end while in (c) and (d) the maximum bending occurs in the middle of the tube. Figure 7.7 shows the formation energy distribution. For (a) and (b), where maximum bending appears at the end, the lowest formation energy is found near the end. In contrast, for (c) and (d), formation energy is lowest in the middle. The distribution indicates that the formation energy correlates directly with the bending moment, which is expected since the latter determines the local stretch in the tube. Figure 7.7 also includes the results from full tube computation. The approximate results are found to be sufficiently accurate in most locations. Only near the boundary the solution shows minor deviations.

7.4.3 Defect interaction

Samsonidze et al. [113] reported that when two SW defects are placed close to each other, the formation energy varies with their relative position and orientation, indicating that two defects may repulse or attract each other depends on their relative position. We studied the interaction of SW defects in stretched tubes using the proposed method. Figure 7.8 shows a defective (10,0) tube having a primary SW defect (bold line upper) and a secondary defect (bold solid lower) inserted at various positions. We considered the following cases: axially adjacent (a); axially distanced (b) and (c); diagonally adjacent (d); axially skewed (e), and diagonally distanced (f) (g). For locations (b) and (c), we employed the ring-1 model for each defect. A larger ring enclosing two SW defects (see Figure 7.8(d)) was used for other cases. The formation energy is defined as the difference of the Gibbs free energies with and without the secondary defect.

The energy curves are presented in Figure 7.9. The diagonally adjacent case (d) shows the lowest formation energy cross the strain range, indicating that such a configuration is most favorable. The axially skewed location (e) has the second lowest formation energy cross the strain range. The rotated bonds at locations (d) and (e) are aligned with 20~50 degrees measured from the tube axis, and this pattern is similar to the findings in [113]. Although the defects are closely packed in (a), the formation energy is only slightly lower than other cases where the defects are further separated, suggesting that axially adjacent defects are less likely to appear in a zigzag tube. It is seen that if the defects are sufficiently distanced from each other, the formation energies appear to be insensitive to the

relative position.

7.4.4 Discussions

We have proposed a method to compute the structural energetic variation induced by the formation of SW defects. The method exploits the local nature of the SW defect and yet properly takes into account the energetic influence from the remaining system. The method falls into the framework of *perturbation method* which is most useful when the few first steps reveal the important features of the solution and the remaining ones give corrections. An attractive feature of perturbation methods is that they do not solve for any additional solution but make use of the obtained unperturbed solution to correct themselves. This approximate method has been widely applied in many mathematical physics problems. This method itself is sufficiently general and should be applicable to other types of local defect.

Compared with more accurate first principle methods, empirical methods (MD/MM) provide an efficient way to study the defect energetics in relatively large systems, allowing to explore the energetic variation at the structural level. In contrast, quantum mechanics analysis can consider only a cluster of atoms. Instead of a small atomic patch, we suggest to use the present method for analyzing the energetic influence of the whole structure. In particular, when the structure is too large to be applied for quantum methods, the present method would help to approximately consider the influence of the environment outside the local defective patch. Note that a combination of the proposed method and quantum mechanical

calculation is ready, that is, to perform quantum analysis on a small cluster and utilize this method to estimate the correction. We expect to motivate further applications using the present method.

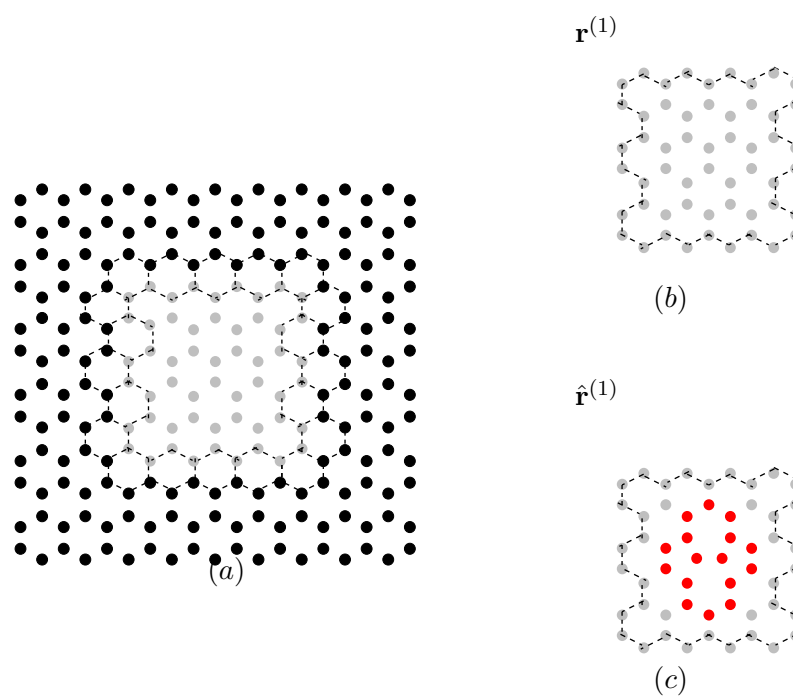


Figure 7.1: Schematics of the method. (a) The grey dots represent the atoms of the local cluster D and the black dots represent pristine atoms. The interface is marked by the layer of dashed hexagon rings. (b) The deformed local region with the atom positioned at $\mathbf{r}^{(1)}$; (c) The defective replica \hat{D} , whose boundary is fixed but the interior atoms are allowed to relax.

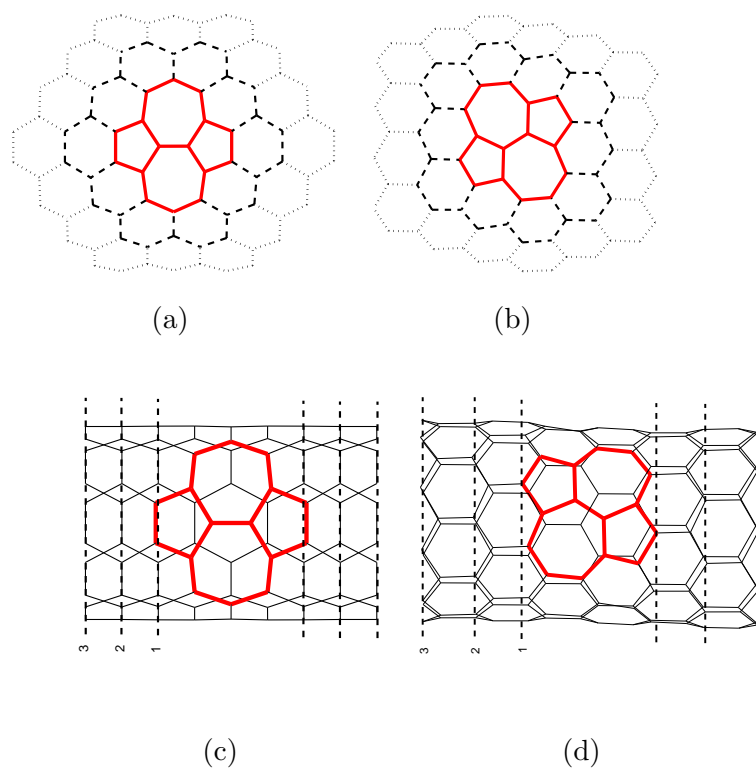
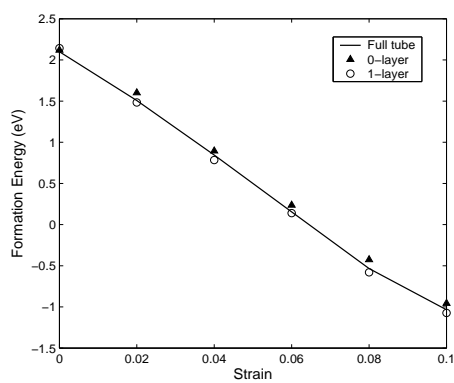
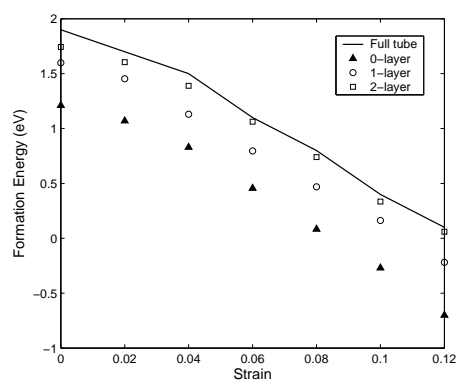


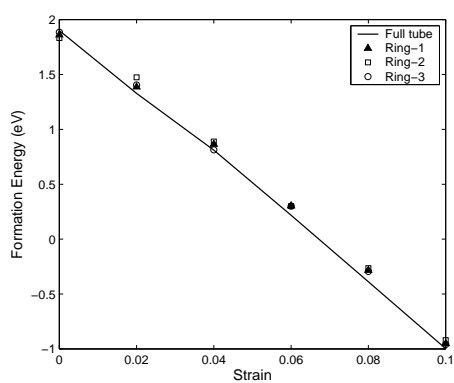
Figure 7.2: Illustration of the defective patches. (a) and (b) The layer models for large diameter tubes; (c) and (d) The ring models for small diameter tubes.



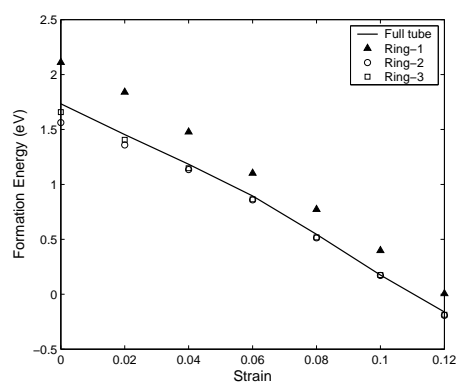
(a) armchair (10,10)



(b) zigzag (17,0)



(c) armchair (5,5)



(d) zigzag (10,0)

Figure 7.3: Comparative formation energies versus stretch

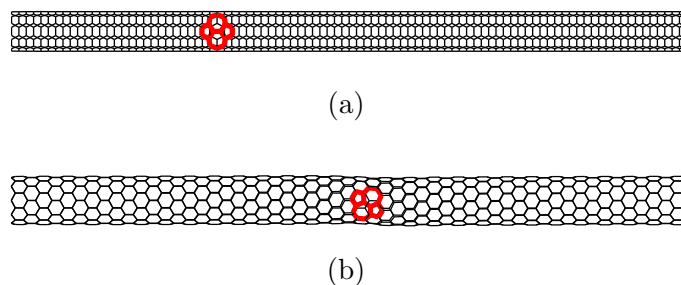


Figure 7.4: Slender tubes (12nm) used in the computation. (a) (5,5) armchair; (b) (10,0) zigzag.

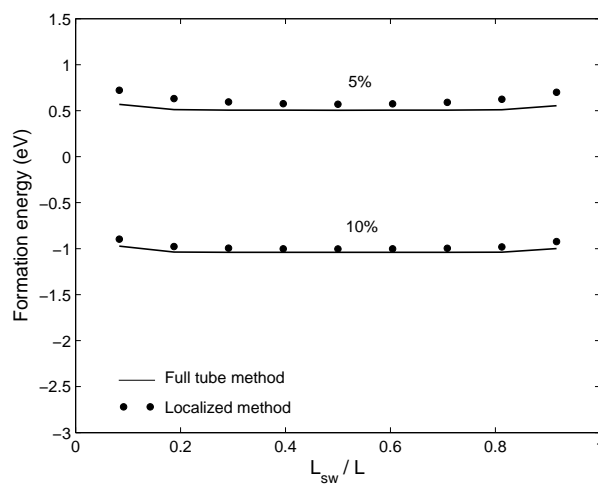


Figure 7.5: The distribution of formation energy in the uniformly stretched nanotube.

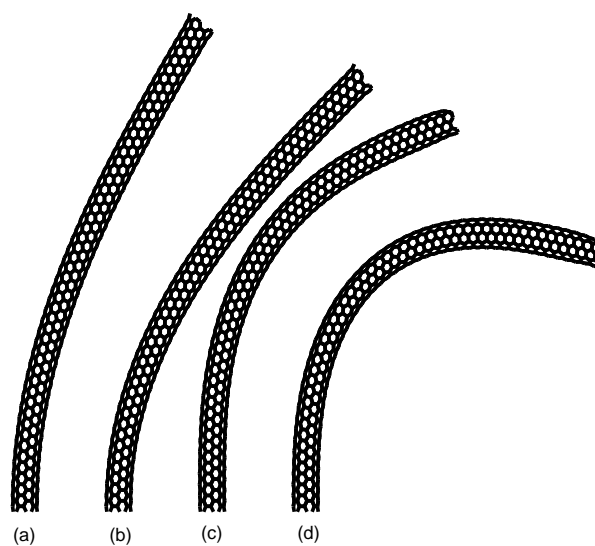


Figure 7.6: Four bended configurations of the (5,5) carbon nanotube.

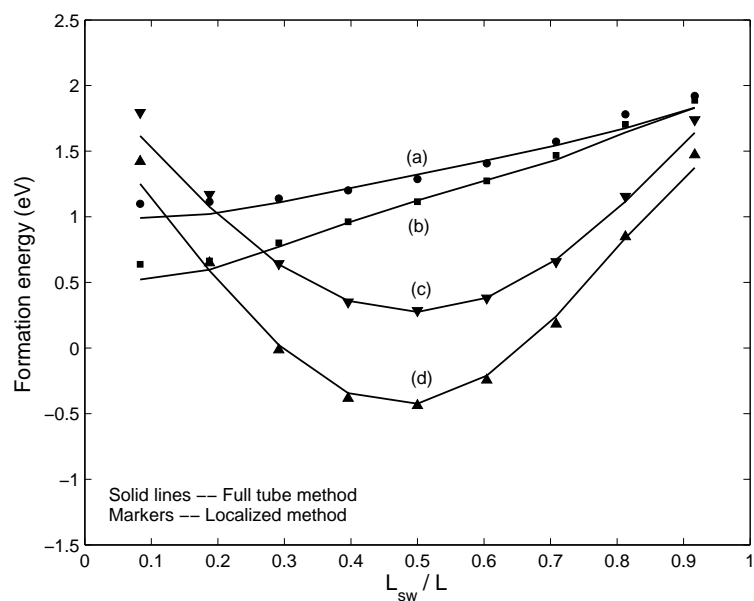


Figure 7.7: The distribution of formation energy on bended (5,5) nanotubes. The curves (a) through (d) correspond to the configurations in Figure 7.6.

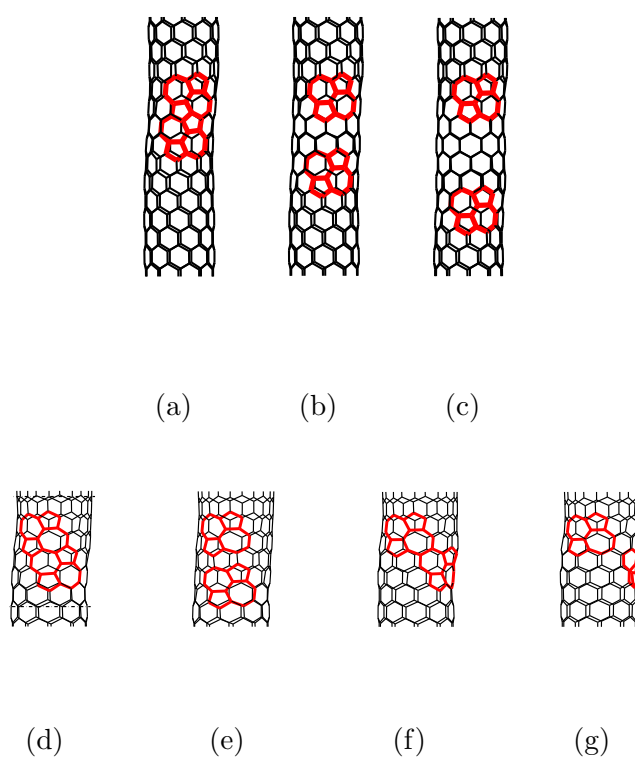


Figure 7.8: Relatively positioned multiple defects.

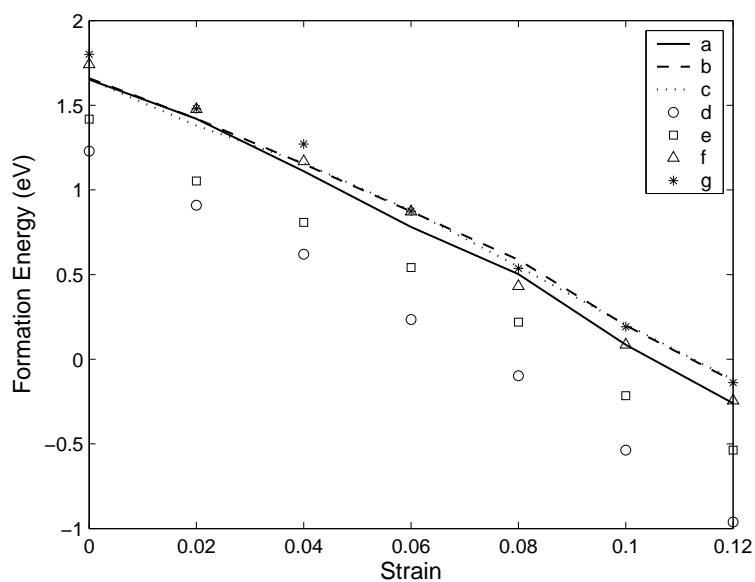


Figure 7.9: Formation energy of a second SW defect. The cases (a) through (f) correspond to the relative positions illustrated in Figure 7.8.

CHAPTER 8 SUMMARY

A framework of analyzing material failure at the atomic scale is presented in this thesis. The failure analysis is performed in terms of the material stability theory. An important characteristic of material instability is the locality, i.e. the loss of material stability may occur merely in a localized region. The local instability may or may not lead to failure of the entire structure, namely, global instability. Predicting the occurrence of local instability and analyzing its development in atomic structures are addressed in this thesis. Both quasi-continuum method and direct atomistic approach are utilized.

A homogenized continuum method for predicting the onset of localized failure of carbon nanotubes is proposed. Failure modes of interest include ductile necking under tension and localized collapse zones under compression, both have been reported by MD simulation and observed in experiments. The onset of such localized failure in carbon nanotubes (CNT) is examined at the continuum level and is captured by the singularity point of the acoustic tensor derived from the continuum model. The criterion derived in this approach corresponds to the instability of a material body under all around displacement boundary conditions. Hence, the results can have direct relevance to the failure of constrained tubes, for instance if the lateral motions are restricted.

The proposed atomistic FEM provides a unified logic for implementing molecular mechanics into existing FEM codes according to the form of bond poten-

tial and lattice topology. For crystals of the same class, the same element can be used. The element preserves the systematic and localized characteristics as classic FEM. A new six-node atomic element is designed for CNTs.

An atomic level material stability theory is developed and provides the atomistic foundation of its continuum counterpart. An atomic acoustic tensor is proposed and utilized in the material stability analysis for atomic systems. The proposed stability criterion does not rely on the continuum stability theory and the pristine lattice structure. The applications in simple crystals and carbon nanotubes are demonstrated, where both perfect and defective systems are considered. The present work justifies the use of strong ellipticity type of condition in atomic scale structure and also validates the applicability of the local instability criterion to defective systems.

Combining the atomistic FEM and the atomic material stability theory, crack growth and fracture in simple crystals and CNTs in the presence of defects have been simulated. Essentially, bond breaking and crack growing all result from instabilities localized at a small region around crack tips. The local instability may not necessarily cause the complete fracture of the structure. The atomic acoustic tensor is applied to decide bond breaking near crack tips. It is found that incorporating the atomic stability criterion into conventional cutoff distance conditions can clearly determine the location of crack tips and observe the cohesive zone near the crack tip. The theory of Barenblatt on equilibrium cracks is justified based on the quasi-static simulation.

An Eshelby-type approximate method is proposed for calculating the for-

mation energy of Stone-Wales defects on carbon nanotubes. Using the empirical method, the energetic analysis is performed at the structural level. The new method presents the fact that the structural energy variation can be evaluated by the energy change in a local defective patch with a correction term representing the structural influence of the remaining system. Then, the optimization of the whole defective system can be bypassed. The method is utilized to investigate the formation energy distribution in non-uniformly deforming nanotubes and the energetic interaction between multiple defects. This energetic information is rare in literature but very useful to understand defect nucleation so as to minimize its affects.

APPENDIX A PROOF OF VAN HOVE'S THEOREM

Here, the proof by Van Hove [29] is shortly reviewed. Consider an elastic body subjected to Dirichlet boundary condition. It is equilibrium at a current configuration. Ω denotes the physical domain occupied by the elastic body. Extend the finite physical domain onto the whole \mathbf{R}^3 by zero outside Ω . Performing the inverse Fourier Transform to the perturbed field, one obtains

$$\delta \mathbf{u}(\mathbf{x}) = \left(\frac{1}{2\pi}\right)^{3/2} \int_{\mathbf{R}^3} e^{i\mathbf{p}\cdot\mathbf{x}} \hat{\mathbf{u}}(\mathbf{p}) d\hat{v}; \quad \mathbf{p} \in \mathbf{R}^3, \quad (\text{A.1})$$

where \mathbf{p} is the wave vector in the spectrum space, $\hat{\mathbf{u}}(\mathbf{p})$ is the Fourier Transform of perturbation $\delta \mathbf{u}(\mathbf{x})$, and $\widehat{(\)}$ denotes the Fourier Transform quantity. Due to the fixed boundary on $\partial\Omega$, the following identity of the gradient field can be easily got as

$$\widehat{\nabla \delta \mathbf{u}(\mathbf{x})} = i\mathbf{p} \otimes \hat{\mathbf{u}}(\mathbf{p}). \quad (\text{A.2})$$

Also, the Fourier Transform is isometric. Thus, the inner product is conserved during the transform. Assume the elastic body is homogeneous and deforms uniformly. Then, the elasticity tensor \mathcal{A} is constant through out the body. The following relation is obvious,

$$\begin{aligned} \int_{\mathbf{R}^3} \mathcal{A}_{i\alpha j\beta} \delta u_{i,\alpha} \delta u_{j,\beta} dv &= \int_{\mathbf{R}^3} \mathcal{A}_{i\alpha j\beta} \widehat{\delta u_{i,\alpha}} \widehat{\delta u_{j,\beta}}^* d\hat{v} \\ &= \int_{\mathbf{R}^3} \mathcal{A}_{i\alpha j\beta} p_\alpha p_\beta \widehat{\delta u_i} \widehat{\delta u_j}^* d\hat{v} \\ &= \text{Re} \left[\int_{\mathbf{R}^3} \mathcal{A}_{i\alpha j\beta} p_\alpha p_\beta \widehat{\delta u_i} \widehat{\delta u_j}^* d\hat{v} \right]. \end{aligned}$$

where (*) represents the conjugate complex. Write $\widehat{\delta\mathbf{u}} = \mathbf{q} + i\mathbf{y}$ with $\mathbf{q}, \mathbf{y} \in \mathbf{R}^3$.

Then,

$$\operatorname{Re} \left[\widehat{\delta u}_i \widehat{\delta u}_j^* \right] = q_i q_j + y_i y_j.$$

Therefore,

$$\operatorname{Re} \left[\int_{\mathbf{R}^3} \mathcal{A}_{i\alpha j\beta} p_\alpha p_\beta \widehat{\delta u}_i \widehat{\delta u}_j^* d\hat{v} \right] = \int_{\mathbf{R}^3} \mathcal{A}_{i\alpha j\beta} (p_\alpha p_\beta q_i q_j + p_\alpha p_\beta y_i y_j) d\hat{v}. \quad (\text{A.3})$$

The strong ellipticity (2.44) is the necessary and sufficient condition to make the stability condition (2.42) hold in this case.

APPENDIX B
VAN HOVE'S THEOREM IN DISCRETE CASE

A finite pristine crystal can be constructed by a three-dimensional array of $L \times L \times L$ unit cells. For simple crystals, i.e., only one basis atom in each primitive unit cell, the total number of atoms is $N_0 = L^3$. Assume lattice basis vectors of the crystal be denoted by \mathbf{a}_1 , \mathbf{a}_2 , and \mathbf{a}_3 . The position vector of a unit cell is expressed as

$$\mathbf{R} = M_1\mathbf{a}_1 + M_2\mathbf{a}_2 + M_3\mathbf{a}_3, \quad (\text{B.1})$$

where $M_{1,2,3}$ are integers in the range of L , $0 < M_{1,2,3} < L$. In classic lattice dynamics, the periodic boundary condition is often applied, such that $U(M) = U(M + L)$.

The reciprocal lattice is defined by the set of vectors

$$\mathbf{Q} = N_1\mathbf{b}_1 + N_2\mathbf{b}_2 + N_3\mathbf{b}_3, \quad (\text{B.2})$$

where $N_{1,2,3}$ are integers and $0 < N_{1,2,3} < L$, the basis vectors of the reciprocal space are

$$\begin{aligned} \mathbf{b}_1 &= (2\pi/V_c)(\mathbf{a}_2 \times \mathbf{a}_3), \\ \mathbf{b}_2 &= (2\pi/V_c)(\mathbf{a}_3 \times \mathbf{a}_1), \\ \mathbf{b}_3 &= (2\pi/V_c)(\mathbf{a}_1 \times \mathbf{a}_2), \end{aligned} \quad (\text{B.3})$$

and $V_c = \mathbf{a}_1 \cdot (\mathbf{a}_2 \times \mathbf{a}_3)$. It is easy to show

$$\mathbf{R} \cdot \mathbf{Q} = 2\pi \times (\text{integer}).$$

Assume the wave vector \mathbf{k} of a plane wave has the form

$$\mathbf{k} = L^{-1}(N_1 \mathbf{b}_1 + N_2 \mathbf{b}_2 + N_3 \mathbf{b}_3). \quad (\text{B.4})$$

Then,

$$\mathbf{k} \cdot \mathbf{Q} = 2\pi \times \frac{M_1 N_1 + M_2 N_2 + M_3 N_3}{L}.$$

When L is finite, the expression (B.4) of wave vector can easily satisfy the periodic boundary condition by using the plane wave expansion in Fourier Transform. If $L \rightarrow \infty$, wave vector \mathbf{k} belongs to one reciprocal unit cell, and $|\mathbf{k} \cdot \mathbf{Q}| < 2\pi$.

Next, to obtain the Fourier Transform, the orthogonality of the plane wave basis is necessary. In one-dimension, the plane waves basis with wave vector y and y' has orthogonality as

$$\sum_{\text{all } n} e^{i(y-y')n} = (2\pi)\delta_{2\pi}(y - y'), \quad (\text{B.5})$$

where $\delta_{2\pi}(y - y') = 0$ unless $y = y'$ or $y - y' = 2\pi$. In three-dimension, in terms of (B.1), the lattice vectors are labelled by M in three directions, namely M_1 , M_2 and M_3 . Using wave vector's definition (B.4), one can write out

$$\begin{aligned} & \sum_{\text{all } M} e^{i(\mathbf{k}(N) - \mathbf{k}'(N')) \cdot \mathbf{R}(M)} \\ &= \sum_{\text{all } M_{1,2,3}} e^{i\frac{2\pi}{L}(N_1 - N'_1)M_1} e^{i\frac{2\pi}{L}(N_2 - N'_2)M_2} e^{i\frac{2\pi}{L}(N_3 - N'_3)M_3} \\ &= \left[\sum_{\text{all } M_1} e^{i\frac{2\pi}{L}(N_1 - N'_1)M_1} \right] \times \left[\sum_{\text{all } M_2} e^{i\frac{2\pi}{L}(N_2 - N'_2)M_2} \right] \times \left[\sum_{\text{all } M_3} e^{i\frac{2\pi}{L}(N_3 - N'_3)M_3} \right] \\ &= (2\pi)^3 \delta_{2\pi}[(N_1 - N'_1)\frac{2\pi}{L}] \delta_{2\pi}[(N_2 - N'_2)\frac{2\pi}{L}] \delta_{2\pi}[(N_3 - N'_3)\frac{2\pi}{L}] \end{aligned} \quad (\text{B.6})$$

where $(N - N')\frac{2\pi}{L} < 2\pi$ since $L \rightarrow \infty$. Therefore, one concludes that

$$\sum_{\text{all } M} e^{i(\mathbf{k} - \mathbf{k}') \cdot \mathbf{R}(M)} = (2\pi)^3 \delta(\mathbf{k} - \mathbf{k}'), \quad (\text{B.7})$$

where $\delta(\mathbf{k} - \mathbf{k}') = 0$ unless $\mathbf{k} - \mathbf{k}' = 0$.

Suppose all displacements of the atoms in the finite crystal denoted by \mathcal{B} , as a sequence of 3-D vectors, constitute a continuous function $\mathbf{u}(\mathbf{X})$, such that

$$\mathbf{u}_i = \mathbf{u}(\mathbf{R}_i). \quad (\text{B.8})$$

Any arbitrary finite crystal \mathcal{B} can be extended to a infinite lattice set \mathcal{L} which is $L \times L \times L$ with $L \rightarrow \infty$. Thus, the function $\mathbf{u}(\mathbf{X})$ can be extended to an infinite lattice \mathcal{L} by assuming zero at the lattice point outside \mathcal{B} , namely $\mathbf{u}(\mathbf{R}_i) = 0$ for $\mathbf{R}_i \in \mathcal{L} \setminus \mathcal{B}$. Here, the displacements of atoms on the boundary of \mathcal{B} are required to be zero. Then, the extended function $\mathbf{u}(\mathbf{X})$ is continuous in \mathbb{R}^3 with period of infinity. Expand the continuous function $\mathbf{u}(\mathbf{X})$ in terms of Fourier Series,

$$\mathbf{u}(\mathbf{X}) = \sum_{\mathbf{k}} \hat{\mathbf{u}}_{\mathbf{k}} e^{i\mathbf{k} \cdot \mathbf{X}}. \quad (\text{B.9})$$

(Usually, for a continuous function with infinite period, instead of Fourier series, the Continuous Fourier Transform is used. Here, the discrete form is retained since an atomic system is essentially discrete and later the Discrete Fourier Transform is directly introduced.) Then, for each atomic position, one writes

$$\mathbf{u}_i = \mathbf{u}(\mathbf{R}_i) = \sum_{\mathbf{k}} \hat{\mathbf{u}}_{\mathbf{k}} e^{i\mathbf{k} \cdot \mathbf{R}_i}. \quad (\text{B.10})$$

The coefficient $\hat{\mathbf{u}}_{\mathbf{k}}$ of plane wave with \mathbf{k} can be obtained by multiplying $e^{-i\mathbf{k}' \cdot \mathbf{R}_i}$ and summing over all \mathbf{R} in (B.1). Making use of the orthogonality condition (B.7), one arrives at

$$\begin{aligned} \sum_{\mathbf{R}_i \in \mathcal{L}} \mathbf{u}_i e^{-i\mathbf{k}' \cdot \mathbf{R}_i} &= \sum_{\mathbf{R}_i \in \mathcal{L}} \sum_{\mathbf{k}} \hat{\mathbf{u}}_{\mathbf{k}} e^{i\mathbf{k} \cdot \mathbf{R}_i} e^{-i\mathbf{k}' \cdot \mathbf{R}_i} = \sum_{\mathbf{k}} \hat{\mathbf{u}}_{\mathbf{k}} \left[\sum_{\mathbf{R}_i \in \mathcal{L}} e^{i(\mathbf{k} - \mathbf{k}') \cdot \mathbf{R}_i} \right] \\ &= \sum_{\mathbf{k}} \hat{\mathbf{u}}_{\mathbf{k}} (2\pi)^3 \delta(\mathbf{k} - \mathbf{k}') = (2\pi)^3 \hat{\mathbf{u}}_{\mathbf{k}'} \end{aligned} \quad (\text{B.11})$$

By the derivation above, finally, the Discrete Fourier Transform can be defined as

$$\hat{\mathbf{u}}_{\mathbf{k}} = (2\pi)^{-3/2} \sum_{\mathbf{R}_i \in \mathcal{L}} \mathbf{u}_i e^{-i\mathbf{k} \cdot \mathbf{R}_i}. \quad (\text{B.12})$$

Clearly, $\hat{\mathbf{u}}_{\mathbf{k}}$ only depends on wave vector \mathbf{k} . The corresponding Inverse Discrete Fourier Transform is

$$\mathbf{u}_i = (2\pi)^{-3/2} \sum_{\mathbf{k}} e^{i\mathbf{k} \cdot \mathbf{R}_i} \hat{\mathbf{u}}_{\mathbf{k}}. \quad (\text{B.13})$$

According to Eq.(B.13), one can write out the expression of the change of interacting lattice vectors

$$\begin{aligned} \delta \mathbf{r}_{ij} = \mathbf{u}_j - \mathbf{u}_i &= (2\pi)^{-3/2} \sum_{\mathbf{k}} [e^{i\mathbf{k} \cdot \mathbf{R}_j} - e^{i\mathbf{k} \cdot \mathbf{R}_i}] \hat{\mathbf{u}}_{\mathbf{k}} \\ &= (2\pi)^{-3/2} \sum_{\mathbf{k}} e^{i\mathbf{k} \cdot \mathbf{R}_i} [(e^{i\mathbf{k} \cdot \mathbf{R}_{ij}} - 1) \hat{\mathbf{u}}_{\mathbf{k}}]. \end{aligned} \quad (\text{B.14})$$

Here $\delta \mathbf{r}_{ij}$ can be considered as a function of position \mathbf{R}_i since by expanding the displacement into plane waves the change of \mathbf{r}_j and \mathbf{r}_i differ by only a phase difference depending on the relative distance \mathbf{R}_{ij} . Then, if considering $[(e^{i\mathbf{k} \cdot \mathbf{R}_{ij}} - 1) \hat{\mathbf{u}}_{\mathbf{k}}]$ as a whole, it is the DFT of $\delta \mathbf{r}_{ij}$,

$$\widehat{\delta \mathbf{r}_{IJ}} = (e^{i\mathbf{k} \cdot \mathbf{R}_{ij}} - 1) \hat{\mathbf{u}}_{\mathbf{k}}. \quad (\text{B.15})$$

In the extended infinite domain, lattice vectors \mathbf{R}_{ij} belong to a constant set \mathcal{L}_0 in which atom j is assumed to interact with atom i . The size of \mathcal{L}_0 depends on the interaction range: if an atom interacts with all the other atoms j , then $\mathcal{L}_0 = \mathcal{L}$; if an atom only interacts with its neighborhoods j within a certain range, then $\mathcal{L}_0 \subset \mathcal{L}$. Since the atoms are identical due to translational invariance, \mathcal{L}_0 is constant and independent of position \mathbf{R}_i . Moreover, seen from (B.15), the interacting pairs ij are identical in physical space and Fourier space, $IJ \leftrightarrow ij$

where the captical letter is used to denote the pair in Fourier space. Then, the DFT $\widehat{\delta\mathbf{r}_{IJ}}$ is also independent of position \mathbf{R}_i or \mathbf{R}_j and only a function of wave vector.

The stability of an atomic system is written according to (D.2) as

$$\delta^2 E = \sum_i \sum_k \delta\mathbf{r}_i \cdot \frac{\partial^2 E}{\partial\mathbf{r}_i \partial\mathbf{r}_k} \delta\mathbf{r}_k > 0. \quad (\text{B.16})$$

In Appendix D.1, it is shown that if the crystal is simple and a pairwise potential is used to describe the atomic interaction,

$$\delta^2 E = \sum_i \left[\sum_{i,j} \sum_{i,k} \delta\mathbf{r}_{ij} \cdot \frac{\partial^2 E_i}{\partial\mathbf{r}_{ij} \partial\mathbf{r}_{ik}} \delta\mathbf{r}_{ik} \right] \quad (\text{B.17})$$

holds, where j and k run through the neighboring atoms of atom i . These neighboring atoms locate within the interaction range of atom i . The range determines the size of \mathcal{L}_0 . Usually, \mathcal{L}_0 is a finite set containing lattice vectors that connect an atom and the ones interacting with it. For the translational invariance, when the configuration is uniform, the stiffness matrix $\frac{\partial^2 E_i}{\partial\mathbf{r}_{ij} \partial\mathbf{r}_{ik}}$ is constant, independent of position \mathbf{R}_i , and denoted by $\mathcal{M}_{ij,ik}$.

In terms of Plancherel theorem which states that DFT is a unitary transformation, and the inner product is conserved during transform,

$$\int_{-\infty}^{\infty} f(x)g(x) dx = \int_{-\infty}^{\infty} \hat{f}(k)\hat{g}^*(k) dk. \quad (\text{B.18})$$

Thus, applying the Plancherel theorem, one writes

$$\begin{aligned} \delta^2 E &= \sum_{\mathbf{R}_i} \left[\sum_{i,j} \sum_{i,k} \delta\mathbf{r}_{ij} \cdot [\mathcal{M}_{ij,ik}] \delta\mathbf{r}_{ik} \right] \\ &= \sum_{\mathbf{k}} \left[\sum_{i,j} \sum_{i,k} \widehat{\delta\mathbf{r}_{IJ}}(\mathbf{k}) \cdot [\mathcal{M}_{ij,ik}] \widehat{\delta\mathbf{r}_{IK}}^*(\mathbf{k}) \right]. \end{aligned} \quad (\text{B.19})$$

It can be proved as follows:

$$\begin{aligned}
& \sum_{\mathbf{R}_i} \left[\sum_{i,j} \sum_{i,k} \delta \mathbf{r}_{ij} \cdot [\mathcal{M}_{ij,ik}] \delta \mathbf{r}_{ik} \right] \\
&= \sum_{\mathbf{R}_i} \{ \delta \mathbf{r}_{ij} \}^T \{ \mathcal{M}_{ij,ik} \} \{ \delta \mathbf{r}_{ik}^* \} \\
&= (2\pi)^{-3} \sum_{\mathbf{R}_i} \left[\sum_{\mathbf{k}} e^{i\mathbf{k} \cdot \mathbf{R}_i} \{ \widehat{\delta \mathbf{r}_{IJ}}(\mathbf{k}) \}^T \right] \{ \mathcal{M}_{ij,ik} \} \left[\sum_{\mathbf{k}'} e^{-i\mathbf{k}' \cdot \mathbf{R}_i} \{ \widehat{\delta \mathbf{r}_{IK}}^*(\mathbf{k}') \} \right] \\
&= (2\pi)^{-3} \sum_{\mathbf{k}} \sum_{\mathbf{k}'} \{ \widehat{\delta \mathbf{r}_{IJ}}(\mathbf{k}) \}^T \{ \mathcal{M}_{ij,ik} \} \{ \widehat{\delta \mathbf{r}_{IK}}^*(\mathbf{k}') \} \left[\sum_{\mathbf{R}_i} e^{i\mathbf{k} \cdot \mathbf{R}_i} e^{-i\mathbf{k}' \cdot \mathbf{R}_i} \right] \quad (\text{B.20}) \\
&= \sum_{\mathbf{k}} \sum_{\mathbf{k}'} \{ \widehat{\delta \mathbf{r}_{IJ}}(\mathbf{k}) \}^T \{ \mathcal{M}_{ij,ik} \} \{ \widehat{\delta \mathbf{r}_{IK}}^*(\mathbf{k}') \} \delta(\mathbf{k} - \mathbf{k}') \\
&= \sum_{\mathbf{k}} \{ \widehat{\delta \mathbf{r}_{IJ}}(\mathbf{k}) \}^T \{ \mathcal{M}_{ij,ik} \} \{ \widehat{\delta \mathbf{r}_{IK}}^*(\mathbf{k}) \} \\
&= \sum_{\mathbf{k}} \left[\sum_{i,j} \sum_{i,k} \widehat{\delta \mathbf{r}_{IJ}}(\mathbf{k}) \cdot [\mathcal{M}_{ij,ik}] \widehat{\delta \mathbf{r}_{IK}}^*(\mathbf{k}) \right],
\end{aligned}$$

where $\{\cdot\}$ stands for the matrix form which replaces the summations, the Inverse DFT $\delta \mathbf{r}_{ij} = (2\pi)^{-3/2} \sum_{\mathbf{k}} e^{i\mathbf{k} \cdot \mathbf{R}_i} \widehat{\delta \mathbf{r}_{IJ}}(\mathbf{k})$ and the orthogonality (B.7) are applied, and the switch of summations between \mathbf{R}_i and \mathbf{k} is employed since $\widehat{\delta \mathbf{r}_{IJ}}(\mathbf{k})$, $\{\mathcal{M}_{ij,ik}\}$ and $\widehat{\delta \mathbf{r}_{IK}}^*(\mathbf{k}')$ are all independent of \mathbf{R}_i . Plugging (B.15) in (B.19) gives

$$\begin{aligned}
\delta^2 E &= \sum_{\mathbf{k}} \left[\sum_{i,j} \sum_{i,k} \hat{\mathbf{u}}_{\mathbf{k}} \cdot (e^{i\mathbf{k} \cdot \mathbf{R}_{ij}} - 1) [\mathcal{M}_{ij,ik}] (e^{i\mathbf{k} \cdot \mathbf{R}_{ik}} - 1)^* \hat{\mathbf{u}}_{\mathbf{k}} \right] \\
&\approx \sum_{\mathbf{k}} \hat{\mathbf{u}}_{\mathbf{k}} \cdot \left[\sum_{i,j} \sum_{i,k} (\mathbf{k} \cdot \mathbf{R}_{ij}) [\mathcal{M}_{ij,ik}] (\mathbf{k} \cdot \mathbf{R}_{ik}) \right] \hat{\mathbf{u}}_{\mathbf{k}} \quad (\text{B.21}) \\
&= \sum_{\mathbf{k}} \hat{\mathbf{u}}_{\mathbf{k}} \cdot \mathbf{Q}_i \hat{\mathbf{u}}_{\mathbf{k}},
\end{aligned}$$

where the expansion

$$e^{i\mathbf{k} \cdot \mathbf{R}_{ij}} = 1 + i\mathbf{k} \cdot \mathbf{R}_{ij} - (\mathbf{k} \cdot \mathbf{R}_{ij})^2/2 + \dots$$

is applied, the higher order terms can be ignored when the wave number approaches zero, and \mathbf{Q}_i is the atomic acoustic tensor. Therefore, it is proved that $\delta^2 E > 0$

if \mathbf{Q}_i is positive definite. Notice that assuming fixed boundary atoms is necessary because (1) the convergence of the Fourier series requires the continuity on the boundary; and (2) the periodicity (or translational invariance) cannot strictly hold when there are free boundaries.

APPENDIX C TENSILE BIFURCATION OF ARMCHAIR TUBES

This Appendix provides a brief comparison of the buckling analysis in [57] and the current work for the special case of armchair tube under uniaxial tension. Starting from a relation between elasticity tensors \mathcal{A} and \mathbb{D}

$$\mathcal{A}_{i\alpha j\beta} = S_{\alpha\beta}\delta_{ij} + F_{i\nu}F_{j\rho}D_{\nu\alpha\rho\beta}, \quad (\text{C.1})$$

where \mathbf{S} is the second Piola-Kirchhoff stress and $\mathbb{D} = \frac{d\mathbf{S}}{d\mathbf{E}}$ is the referential elasticity tensor, the acoustic tensor can be written as

$$Q_{ij} = S_{\alpha\beta}N_{\alpha}N_{\beta}\delta_{ij} + F_{i\nu}F_{j\rho}D_{\nu\alpha\rho\beta}N_{\alpha}N_{\beta}. \quad (\text{C.2})$$

For the uniaxial tension specified in (3.29), the non-zero terms are axial stress S_{11} , the axial stretch λ_Z and hoop stretch λ_{Θ} . Setting $\mathbf{N} = \mathbf{E}_Z$, the nonzero entries of \mathbf{Q} are

$$\begin{aligned} Q_{11} &= S_{ZZ} + \lambda_Z^2 D_{ZZZZ}, \\ Q_{22} &= S_{ZZ} + \lambda_{\Theta}^2 D_{\Theta Z \Theta Z}, \\ Q_{12} &= \lambda_Z \lambda_{\Theta} D_{ZZ \Theta Z}. \end{aligned} \quad (\text{C.3})$$

The condition $\det \mathbf{Q} = 0$ reduces to

$$\left(D_{ZZZZ} + \frac{S_{ZZ}}{\lambda_Z^2}\right)\left(D_{\Theta Z \Theta Z} + \frac{S_{ZZ}}{\lambda_{\Theta}^2}\right) - D_{ZZ \Theta Z} = 0. \quad (\text{C.4})$$

Assuming that $B(\cos \theta_{ij}, \cos \theta_{ik})$ in T-B potential is constant and that $\boldsymbol{\beta} = \mathbf{0}$, as in reference [57], the tangent modulus takes the form

$$\mathbb{D} = \frac{1}{A_0} \sum_{i=1}^3 \left(\frac{V_i''}{r_i^2} - \frac{V_i'}{r_i^3} \right) \mathbf{A}_i \otimes \mathbf{A}_i \otimes \mathbf{A}_i \otimes \mathbf{A}_i, \quad (\text{C.5})$$

where $V_i = V(r_i) = V_R(r_i) - BV_A(r_i)$. In this case, $D_{ZZ\Theta Z} = D_{\Theta ZZZ} = D_{Z\Theta ZZ} = D_{ZZZ\Theta} = 0$ holds regardless of chirality angle. The jump condition reduces to

$$S_{ZZ} + \lambda_Z^2 D_{ZZZZ} = 0 \quad \text{or} \quad S_{ZZ} + \lambda_{\Theta}^2 D_{\Theta Z\Theta Z} = 0, \quad (\text{C.6})$$

whichever reaches first. In tension, actual computation shows that $S_{ZZ} + \lambda_{\Theta}^2 D_{\Theta Z\Theta Z} \neq 0$ within the range of stretch considered, therefore the critical state is characterized by $S_{ZZ} + \lambda_Z^2 D_{ZZZZ} = 0$.

The criterion deduced by Huang's group (Eq.(32) of [57]) states that

$$(D_{ZZZZ} + \frac{S_{ZZ}}{\lambda_Z^2})(D_{\Theta\Theta\Theta\Theta} + \frac{S_{ZZ}}{\lambda_{\Theta}^2}(\frac{m\pi R}{L})) = D_{\Theta\Theta ZZ}^2, \quad (\text{C.7})$$

where R is the tube radius and L is the tube length. Now, if $R \rightarrow \infty$, to make the right hand side finite, the first factor should be diminishingly small, which yields the same condition. In [54], Huang et al further showed that for axisymmetric buckling, the critical strain for an armchair is almost insensitive to tube geometry.

APPENDIX D THE ATOMIC STABILITY

D.1 Proof of the sufficiency of stability

For a general interatomic potential $E = E(\mathbf{r}_{ij}, \mathbf{r}_{kl}, \dots)$, we take the variation with respect to \mathbf{r}_i , the position vector of each atom.

$$\begin{aligned}
 \delta E &= \sum_{i < j} \frac{\partial E}{\partial \mathbf{r}_{ij}} \cdot \delta \mathbf{r}_{ij} = \sum_{i < j} \frac{\partial E}{\partial \mathbf{r}_{ij}} \cdot (\delta \mathbf{r}_j - \delta \mathbf{r}_i) \\
 &= \delta \mathbf{r}_1 \cdot \left(- \sum_{j \neq 1} \frac{\partial E}{\partial \mathbf{r}_{1j}} \right) + \delta \mathbf{r}_2 \cdot \left(- \sum_{j \neq 2} \frac{\partial E}{\partial \mathbf{r}_{2j}} \right) + \dots \\
 &= \sum_i \frac{\partial E}{\partial \mathbf{r}_i} \cdot \delta \mathbf{r}_i,
 \end{aligned} \tag{D.1}$$

where the chain rule $\frac{\partial E}{\partial \mathbf{r}_i} = - \sum_{j \neq i} \frac{\partial E}{\partial \mathbf{r}_{ij}}$ is used. Straightforwardly, we can write out the second variation

$$\begin{aligned}
 \delta^2 E &= \sum_{i < j} \sum_{k < l} \delta \mathbf{r}_{ij} \cdot \frac{\partial^2 E}{\partial \mathbf{r}_{ij} \partial \mathbf{r}_{kl}} \cdot \delta \mathbf{r}_{kl} \\
 &= \sum_i \delta \left(\frac{\partial E}{\partial \mathbf{r}_i} \right) \cdot \delta \mathbf{r}_i \\
 &= \sum_i \sum_j \delta \mathbf{r}_i \cdot \frac{\partial^2 E}{\partial \mathbf{r}_i \partial \mathbf{r}_j} \cdot \delta \mathbf{r}_j.
 \end{aligned} \tag{D.2}$$

Then, the equivalence of different forms in second-order variation is obvious. The requirement on the partition of total potential is

$$\sum_{i < j} \frac{\partial E}{\partial \mathbf{r}_{ij}} = \sum_i \sum_{j \neq i} \frac{\partial E_i}{\partial \mathbf{r}_{ij}}. \tag{D.3}$$

The pairwise interatomic potential $E = \sum_{i < j} V(r_{ij})$ can be easily shown to satisfy (D.3), where the site potential is

$$E_i = \frac{1}{2} \sum_{j \neq i} V_{ij}.$$

With (D.3), we have

$$\sum_{i<j} \sum_{k<l} \delta \mathbf{r}_{ij} \cdot \frac{\partial^2 E}{\partial \mathbf{r}_{ij} \partial \mathbf{r}_{kl}} \cdot \delta \mathbf{r}_{kl} = \sum_i \left[\sum_{j \neq i} \sum_{k<l} \delta \mathbf{r}_{ij} \cdot \frac{\partial^2 E_i}{\partial \mathbf{r}_{ij} \partial \mathbf{r}_{kl}} \cdot \delta \mathbf{r}_{kl} \right]. \quad (\text{D.4})$$

As shown, the global condition can be regrouped and expressed in terms of a summation of local entities in the square bracket. While all these local terms are positive definite as (5.15), the global condition (5.13) is guaranteed. If the equilibrium configuration and the perturbed configuration are uniform, the atomic condition (5.15) and global condition (5.13) are equivalent.

D.2 Atomic acoustic tensor for pairwise potentials

Further insight into the tensor \mathbf{Q}_a may be obtained by examining it in the context of pairwise potentials in which the interaction between two atoms depends on the bond length r_{ab} only, namely $V_{ab} = V(r_{ab})$. For this system, the expression of site energy is fairly simple, i.e., $E_a = \frac{1}{2} \sum_{b \neq a} V_{ab}$. Then, the acoustic tensor (5.18) reads

$$\mathbf{Q}_a = \sum_{b \neq a} \left[\frac{1}{r_{ab}^2} \left(\frac{\partial^2 V_{ab}}{\partial r_{ab}^2} - \frac{1}{r_{ab}} \frac{\partial V_{ab}}{\partial r_{ab}} \right) (\mathbf{r}_{ab} \cdot \mathbf{n})^2 \mathbf{r}_{ab} \otimes \mathbf{r}_{ab} + \frac{1}{r_{ab}} \frac{\partial V_{ab}}{\partial r_{ab}} (\mathbf{r}_{ab} \cdot \mathbf{n})^2 \mathbf{I} \right], \quad (\text{D.5})$$

where \mathbf{I} is the second order identity tensor. The summation is over all bonds emanating from atom a . On the other hand, following the definition of the Virial stress [78, 79, 80, 81], in the static case ($T=0$) we can write

$$\boldsymbol{\tau} = \frac{1}{\omega_a} \sum_{b \neq a} \frac{1}{r_{ab}} \frac{\partial V_{ab}}{\partial r_{ab}} \mathbf{r}_{ab} \otimes \mathbf{r}_{ab}, \quad (\text{D.6})$$

where ω_a is the volume of site a . The isothermal elastic constant for a particular thermodynamical ensemble at $T = 0$ can be obtained from the Ray sum [73, 74]

$$\mathbb{C} = \frac{1}{\omega_a} \sum_{b \neq a} \frac{1}{r_{ab}^2} \left(\frac{\partial^2 V_{ab}}{\partial r_{ab}^2} - \frac{1}{r_{ab}} \frac{\partial V_{ab}}{\partial r_{ab}} \right) \mathbf{r}_{ab} \otimes \mathbf{r}_{ab} \otimes \mathbf{r}_{ab} \otimes \mathbf{r}_{ab}. \quad (\text{D.7})$$

Substituting these expressions into the continuum acoustic tensor (5.4) in Eulerian framework (Λ -criterion), i.e.,

$$Q(\mathbf{n})_{ij} = \mathbb{C}_{ijkl}n_k n_l + \delta_{ik}\tau_{jl}n_k n_l, \quad (\text{D.8})$$

results in an expression identical to (D.5). For a complicate system with multibody interaction, the application of (5.18) requires a proper partition of the site energy.

APPENDIX E PROOF OF FORMATION ENERGY CALCULATION

Starting from equations (7.1) and (7.3), adding and subtracting the boundary term $\sum_{s \in I} \mathbf{t}_s^{(1)} \cdot (\mathbf{r}_s^{(2)} - \mathbf{r}_s^{(1)})$ gives

$$\begin{aligned}
 E_f &\equiv \Pi^{(2)} - \Pi^{(1)} \\
 &= \left[E_P(\mathbf{r}_i^{(2)}) - E_P(\mathbf{r}_i^{(1)}) - \sum_{b \in B_t} \bar{\mathbf{t}}_b \cdot (\mathbf{r}_b^{(2)} - \mathbf{r}_b^{(1)}) - \sum_{s \in I} (-\mathbf{t}_s^{(1)}) \cdot (\mathbf{r}_s^{(2)} - \mathbf{r}_s^{(1)}) \right] \\
 &+ \left[E_{\hat{D}}(\mathbf{r}_d^{(2)}) - E_D(\mathbf{r}_d^{(1)}) - \sum_{s \in I} \mathbf{t}_s^{(1)} \cdot (\mathbf{r}_s^{(2)} - \mathbf{r}_s^{(1)}) \right],
 \end{aligned} \tag{E.1}$$

where $\mathbf{t}_s^{(1)}$ is the internal force exerted on the interface atoms to maintain D in the reference state $\mathbf{r}^{(1)}$. Adding and subtracting terms further, the energy difference can be written as

$$\begin{aligned}
 E_f &= \left[E_P(\mathbf{r}_i^{(2)}) - E_P(\mathbf{r}_i^{(1)}) - \sum_{b \in B_t} \bar{\mathbf{t}}_b \cdot (\mathbf{r}_b^{(2)} - \mathbf{r}_b^{(1)}) - \sum_{s \in I} (-\mathbf{t}_s^{(1)}) \cdot (\mathbf{r}_s^{(2)} - \mathbf{r}_s^{(1)}) \right] \\
 &+ \left[E_{\hat{D}}(\mathbf{r}_d^{(2)}) - E_{\hat{D}}(\hat{\mathbf{r}}_d^{(1)}) - \sum_{s \in I} \hat{\mathbf{t}}_s^{(1)} \cdot (\mathbf{r}_s^{(2)} - \mathbf{r}_s^{(1)}) \right] \\
 &+ E_{\hat{D}}(\hat{\mathbf{r}}_d^{(1)}) - E_D(\mathbf{r}_d^{(1)}) + \sum_{s \in I} (\hat{\mathbf{t}}_s^{(1)} - \mathbf{t}_s^{(1)}) \cdot (\mathbf{r}_s^{(2)} - \mathbf{r}_s^{(1)}).
 \end{aligned} \tag{E.2}$$

In what follows the terms in square brackets will be simplified. The first term corresponds to the energy variation in region P under the variation of atomic positions $\mathbf{r}^{(1)} \rightarrow \mathbf{r}^{(2)}$, here $\mathbf{r}^{(1)}$ is the equilibrium configuration under the specified external load whereas and $\mathbf{r}^{(2)}$ is regarded as a kinematically admissible deformation. By

Taylor expansion,

$$E_P(\mathbf{r}_i^{(2)}) - E_P(\mathbf{r}_i^{(1)}) = \sum_{i \in P} \left. \frac{\partial E}{\partial \mathbf{r}_i} \right|_{\mathbf{r}^{(1)}} \cdot \Delta \mathbf{r}_i + \frac{1}{2} \sum_{i,j \in P} \Delta \mathbf{r}_i \cdot \left[\left. \frac{\partial^2 E}{\partial \mathbf{r}_i \partial \mathbf{r}_j} \right|_{\mathbf{r}^{(1)}} \Delta \mathbf{r}_j \right] + O(|\Delta \mathbf{r}|^3), \quad (\text{E.3})$$

where $\Delta \mathbf{r}_i = \mathbf{r}_i^{(2)} - \mathbf{r}_i^{(1)}$. Invoking the virtual work principle,

$$\sum_{i \in P} \left. \frac{\partial E}{\partial \mathbf{r}_i} \right|_{\mathbf{r}^{(1)}} \cdot \delta \mathbf{r}_i = \sum_{b \in B_t} \bar{\mathbf{t}}_b \cdot \delta \mathbf{r}_b + \sum_{s \in I} (-\mathbf{t}_s^{(1)}) \cdot \delta \mathbf{r}_s \quad (\text{E.4})$$

for any kinematically admissible variation $\delta \mathbf{r}$. Setting $\delta \mathbf{r} = \mathbf{r}^{(2)} - \mathbf{r}^{(1)}$ in (E.4), the first order terms in the first square bracket of (E.2) vanishes, leaving

$$\frac{1}{2} \sum_{i,j \in P} \Delta \mathbf{r}_i \cdot \left[\left. \frac{\partial^2 E}{\partial \mathbf{r}_i \partial \mathbf{r}_j} \right|_{\mathbf{r}^{(1)}} \Delta \mathbf{r}_j \right] + O(|\Delta \mathbf{r}|^3). \quad (\text{E.5})$$

The remainder can be further expressed in terms of boundary sums. Setting $\delta \mathbf{r} = \mathbf{r}^{(2)} - \mathbf{r}^{(1)}$ in the virtual work principle (E.4) gives

$$\sum_{i \in P} \left. \frac{\partial E}{\partial \mathbf{r}_i} \right|_{\mathbf{r}^{(1)}} \cdot (\mathbf{r}_i^{(2)} - \mathbf{r}_i^{(1)}) = \sum_{b \in B_t} \bar{\mathbf{t}}_b \cdot (\mathbf{r}_b^{(2)} - \mathbf{r}_b^{(1)}) + \sum_{s \in I} (-\mathbf{t}_s^{(1)}) \cdot (\mathbf{r}_s^{(2)} - \mathbf{r}_s^{(1)}). \quad (\text{E.6})$$

On the other hand, regarding $\mathbf{r}^{(2)}$ as the equilibrium solution under the external load $\bar{\mathbf{t}}$ on B and internal force $\mathbf{t}_s^{(2)}$ on I , we have,

$$\sum_{i \in P} \left. \frac{\partial E}{\partial \mathbf{r}_i} \right|_{\mathbf{r}^{(2)}} \cdot (\mathbf{r}_i^{(1)} - \mathbf{r}_i^{(2)}) = \sum_{b \in B_t} \bar{\mathbf{t}}_b \cdot (\mathbf{r}_b^{(1)} - \mathbf{r}_b^{(2)}) + \sum_{s \in I} (-\mathbf{t}_s^{(2)}) \cdot (\mathbf{r}_s^{(1)} - \mathbf{r}_s^{(2)}). \quad (\text{E.7})$$

Adding (E.6) and (E.7), and using

$$\begin{aligned} & \sum_{i \in P} \left. \frac{\partial E}{\partial \mathbf{r}_i} \right|_{\mathbf{r}^{(1)}} \cdot (\mathbf{r}_i^{(2)} - \mathbf{r}_i^{(1)}) + \sum_{i \in P} \left. \frac{\partial E}{\partial \mathbf{r}_i} \right|_{\mathbf{r}^{(2)}} \cdot (\mathbf{r}_i^{(1)} - \mathbf{r}_i^{(2)}) \\ &= - \sum_{i,j \in P} \Delta \mathbf{r}_i \cdot \left[\left. \frac{\partial^2 E}{\partial \mathbf{r}_i \partial \mathbf{r}_j} \right|_{\mathbf{r}^{(1)}} \Delta \mathbf{r}_j \right] + O(|\Delta \mathbf{r}|^3), \end{aligned} \quad (\text{E.8})$$

we obtain

$$\frac{1}{2} \sum_{i \in P} \Delta \mathbf{r}_i \cdot \left[\left. \frac{\partial^2 E}{\partial \mathbf{r}_i \partial \mathbf{r}_j} \right|_{\mathbf{r}^{(1)}} \Delta \mathbf{r}_j \right] = \frac{1}{2} \sum_{s \in I} -(\mathbf{t}_s^{(2)} - \mathbf{t}_s^{(1)}) \cdot (\mathbf{r}_s^{(2)} - \mathbf{r}_s^{(1)}) + O(|\Delta \mathbf{r}|^3). \quad (\text{E.9})$$

Combining (E.5) and (E.9), we conclude that the first square bracket of (E.2) becomes

$$\begin{aligned} E_P(\mathbf{r}_i^{(2)}) - E_P(\mathbf{r}_i^{(1)}) - \sum_{b \in B} \bar{\mathbf{t}}_b \cdot (\mathbf{r}_b^{(2)} - \mathbf{r}_b^{(1)}) - \sum_{s \in I} (-\mathbf{t}_s^{(1)}) \cdot (\mathbf{r}_s^{(2)} - \mathbf{t}_s^{(1)}) \\ = \frac{1}{2} \sum_{s \in I} -(\mathbf{t}_s^{(2)} - \mathbf{t}_s^{(1)}) \cdot (\mathbf{r}_s^{(2)} - \mathbf{r}_s^{(1)}) + O(|\Delta \mathbf{r}|^3). \end{aligned} \quad (\text{E.10})$$

Applying the same procedure to the second bracket yields,

$$E_{\hat{D}}(\mathbf{r}_d^{(2)}) - E_{\hat{D}}(\hat{\mathbf{r}}_d^{(1)}) - \sum_{s \in I} \hat{\mathbf{t}}_s^{(1)} \cdot (\mathbf{r}_s^{(2)} - \hat{\mathbf{r}}_d^{(1)}) = \frac{1}{2} \sum_{s \in I} (\mathbf{t}_s^{(2)} - \hat{\mathbf{t}}_s^{(1)}) \cdot (\mathbf{r}_s^{(2)} - \mathbf{r}_s^{(1)}) + O(|\Delta \mathbf{r}|^3). \quad (\text{E.11})$$

Substituting (E.10) and (E.11) into (E.2), the energy release (E.1) becomes

$$E_f = E_{\hat{D}}(\hat{\mathbf{r}}_d^{(1)}) - E_D(\mathbf{r}_d^{(1)}) + \frac{1}{2} \sum_{s \in I} (\hat{\mathbf{t}}_s^{(1)} - \mathbf{t}_s^{(1)}) \cdot (\mathbf{r}_s^{(2)} - \mathbf{r}_s^{(1)}) + O(|\Delta \mathbf{r}|^3), \quad (\text{E.12})$$

where $\hat{\mathbf{t}}_s^{(1)} - \mathbf{t}_s^{(1)}$ is the mismatching force. The final position $\mathbf{r}^{(2)}$ can be obtained by relaxing the mismatching force, or equivalently by applying a set of equal and opposite forces on the interface. To the first order, the interface atoms incremental displacements induced by the relaxation can be computed by

$$\mathbf{r}_s^{(2)} - \mathbf{r}_s^{(1)} = - \sum_{s,t \in I} \mathbb{C}_{st} (\hat{\mathbf{t}}_t^{(1)} - \mathbf{t}_t^{(1)}). \quad (\text{E.13})$$

Here \mathbb{C} is the current compliance associated with the interface atoms. In light of this, we can further write

$$E_f = E_{\hat{D}}(\hat{\mathbf{r}}_d^{(1)}) - E_D(\mathbf{r}_d^{(1)}) - \frac{1}{2} \sum_{s,t \in I} (\hat{\mathbf{t}}_s^{(1)} - \mathbf{t}_s^{(1)}) \cdot \mathbb{C}_{st} (\hat{\mathbf{t}}_t^{(1)} - \mathbf{t}_t^{(1)}) + O(|\Delta \mathbf{r}|^3). \quad (\text{E.14})$$

It is evident that the formula (7.7) is second order accurate with respect to the magnitude of the mismatch force. If the potential energy is quadratic, the third order remainders is identically zero.

REFERENCES

- [1] C. Truesdell and W. Noll. *The Non-Linear Field Theories of Mechanics. Handbuch der Physik III/3 (S.Flugge, Ed.)*. Springer-Verlag, Berlin, 1965.
- [2] R. Hill. On uniqueness and stability in the theory of finite elastic strain. *Journal of the Mechanics and Physics of Solids*, 5:229–241, 1957.
- [3] R.W. Ogden. *Non-linear elastic deformations*. Dover Publication, New York, 1997.
- [4] Z.P. Bazant and L. Cedolin. *Stability of Structures: Elastic, Inelastic, Fracture and Damage Theories*. Dover Publications, New York, 2003.
- [5] Quoc Son Nguyen. *Stability and Nonlinear Solid Mechanics*. John Wiley and Sons, Ltd, Chichester, 2000.
- [6] M. Born and K. Huang. *Dynamical Theory of Crystal Lattices*. Oxford University Press, Oxford, 1954.
- [7] H. Bottger. *Principles of the Theory of Lattice Dynamics*. Weinheim Physik-Verlag, Berlin, 1983.
- [8] F. Milstein. Theoretical strength of a perfect crystal. *Physical Review B*, 3(4):1130–1141, 1971.
- [9] R. Hill and F. Milstein. Principles of stability analysis of ideal crystals. *Physical Review B*, 15(6):3087–3096, 1977.
- [10] F. Milstein and R. Hill. Theoretical properties of cubic crystals at arbitrary pressure - iii. stability. *Journal of the Mechanics and Physics of Solids*, 27:255–279, 1979.
- [11] J.H. Wang, J. Li, and S. Yip. Mechanical instabilities of homogeneous crystals. *Physical Review B*, 52(17):12627, 1995.
- [12] J. H. Wang, J. Li, S. Yip, D. Wolf, and S. Phillpot. Unifying two criteria of born: Elastic instability and melting of homogeneous crystals. *Physica A*, 240:396–403, 1997.
- [13] J. M. Morris and C. R. Krenn. The internal stability of an elastic solid. *Philosophical Magazine A*, 80(12):2827–2840, 2000.

- [14] J.W. Morris, C.R. Krenn, D. Roundy, and Marvin L. Cohen. Deformation at the limit of elastic stability. *Materials Science and Engineering A*, 309-310:121–124, 2001.
- [15] K. Yashiro and Y Tomita. Local lattice instability at a dislocation nucleation and motion. *Journal de Physique IV (Proceedings)*, 11(Pr5):Pr5–3 10, 2001.
- [16] K.J. Van Vliet, J. Li, T. Zhu, S. Yip, and S. Suresh. Quantifying the early stages of plasticity through nanoscale experiments and simulations. *Physical Review B*, 67(10):104105, 2003.
- [17] J. Li, K. J. Van Vliet, T. Zhu, S. Yip, and S. Suresh. Atomistic mechanisms governing elastic limit and incipient plasticity in crystals. *Nature*, 418(18):307–310, 2002.
- [18] T. Zhu, J. Li, K. J. Van Vliet, S. Ogata, S. Yip, and S. Suresh. Predictive modeling of nanoindentation-induced homogeneous dislocation nucleation in copper. *Journal of the Mechanics and Physics of Solids*, 52:691–724, 2004.
- [19] C.S. Jayanthi, M. Tang, S.Y. Wu, J.A. Cocks, and S. Yip. Local analysis of structural instability in stressed lattices: crack nucleation in a covalent solid. *Physical Review Letters*, 79(23):4601–4604, 1997.
- [20] T. Kitamura, Y. Umeno, and R. Fushino. Instability criterion of inhomogeneous atomic system. *Materials Science and Engineering A*, 379:229–233, 2004.
- [21] T. Kitamura, Y. Umeno, and N. Tsuji. Analytical evaluation of unstable deformation criterion of atomic structure and its application to nanostructure. *Computational Materials Science*, 29:499–510, 2004.
- [22] S.V. Dmitriev, J. Li, N. Yoshikawa, Y. Tanaka, Y. Kagawa, T. Kitamura, and S. Yip. Breaking atomic bonds through vibrational mode localization. *Defect and Diffusion Forum*, 233-234:49–59, 2004.
- [23] S. V. Dmitriev, T. Kitamura, J. Li, Y. Umeno, K. Yashiro, and N. Yoshikawa. Near-surface lattice instability in 2d fiber and half-space. *Acta Materialia*, 53:1215–1224, 2005.
- [24] Q.W. Brenner. Empirical potential for hydrocarbons for use in simulating the chemical vapor deposition of diamond films. *Physical Review B*, 42:9458–9471, 1990.
- [25] D. W. Brenner et al. A second-generation reactive empirical bond order (rebo) potential energy expression for hydrocarbons. *Journal of Physics: Condensed Matter*, 14:783–802, 2002.

- [26] G. I. Barenblatt. The mathematical theory of equilibrium cracks in brittle fracture. *Advances in Applied Mechanics*, 7:55–129, 1962.
- [27] J.H. Wang and S. Yip. Crystal instabilities at finite strain. *Physical Review Letters*, 71(25):4182–4185, 1993.
- [28] J. W. Gibbs. *The Scientific Papers of J. Willard Gibbs, vol. 1, Thermodynamics*. Ox Bow Press, Woodbridge, Connecticut, U.S., 1993.
- [29] L. Van Hove. Sur l'extension de la condition de Legendre du calcul des variations aux intégrales multiples à plusieurs fonctions inconnues. *Koninklijke Nederlandse Akademie van Wetenschappen. Afdeling Natuurkunde. Proceedings of the section of sciences*, 50:18–23, 1947.
- [30] J.R. Rice. *The localization of plastic deformation*. In W.T. Koiter, editor, *Theoretical and Applied Mechanics*, Page:207-220. North-Holland Publishing Company, 1976.
- [31] P. Klein and H. Gao. Numerical simulation of crack growth in an isotropic solid with randomized internal cohesive bonds. *Journal of the Mechanics and Physics of Solids*, 46(2):187, 1998.
- [32] P. Klein and H. Gao. Crack nucleation and growth as strain localization in a virtual-bond continuum. *Engineering Fracture Mechanics*, 61:21–48, 1998.
- [33] R. Sunyk and P. Steinmann. Localization analysis of mixed continuum-atomistic models. *Journal de Physique IV (Proceedings)*, Pr5:251, 2001.
- [34] E.B. Tadmor, M. Ortiz, , and R. Phillips. Quasicontinuum analysis of defects in solids. *Philosophical Magazine*, 73:1529–1563, 1996.
- [35] Duane C. Wallace. *Thermodynamics of Crystals*. John Wiley and Sons, Inc, New York, 1972.
- [36] B.I. Yakobson, C.J. Brabec, and J. Bernholc. Nanomechanics of carbon tubes: instabilities beyond linear response. *Physical Review Letters*, 76:2511–2514, 1996.
- [37] B.I. Yakobson, M.P. Campbell, C.J. Brabec, and J. Bernholc. High strain rate fracture and c-chain unraveling in carbon. *Computational Materials Science*, 8:341–348, 1997.
- [38] S. Iijima, C. Brabec, A. Matti, and J. Bernholc. Structural flexibility of carbon nanotubes. *Journal of Chemical Physics*, 104(5):2089–2092, February 1996.

- [39] M. Arroyo and T. Belytschko. Finite crystal elasticity of carbon nanotubes based on the exponential Cauchy-Born rule. *Physical Review B*, 69:115415, 2004.
- [40] M. Arroyo and T. Belytschko. Finite element methods for the non-linear mechanics of crystalline sheets and nanotubes. *International Journal for Numerical Methods in Engineering*, 59:419–456, 2004.
- [41] M.A.L. Marques, H.E. Troiani, M. Miki-Yoshida, M. Jose-Yacaman, and a. Rubio. On the breaking of carbon nanotubes under tension. *Nano Letters*, 4(5):811–815, 2004.
- [42] M.F. Yu, O. Lourie, M.J. Dyer, K. Moloni, T.F. Kelly, and R.S. Ruoff. Strength and breaking mechanism of multiwalled carbon nanotubes under tensile load. *Science*, 287:637–640, 2000.
- [43] T. Belytschko, S.P. Xiao, G.C. Schatz, and R.S. Ruoff. Atomistic simulations of nanotube fracture. *Physical Review B*, 65:235430, 2002.
- [44] S.L. Mielke, D. Troya, S.L. Zhang, J.L. Li, S. Xiao, R. Car, R.S. Ruoff, G.C. Schatz, and T. Belytschko. The role of vacancy defects and holes in the fracture of carbon nanotubes. *Chemical Physics Letters*, 390:413–420, 2004.
- [45] O. Lourie, D.M. Cox, and H.D. Wagner. Buckling and collapse of embedded carbon nanotubes. *Physical Review Letters*, 81(8):1638–1641, August 1998.
- [46] D. Srivastava, M. Meunon, and K. Cho. Nanoplasticity of single-walled carbon nanotubes under uniaxial compression. *Physical Review Letters*, 83:2973–2976, 1999.
- [47] D. Srivastava, M. Meunon, and K. Cho. Anisotropic nanomechanis of boron nitrid nanotubes: nanostructured “skin” effect. *Physical Review B*, 63:195413–195416, 2001.
- [48] R. Hill. Acceleration waves in solids. *Journal of the Mechanics and Physics of Solids*, 10:1–16, 1962.
- [49] A. Needleman. Analysis of plastic flow localization in metals. *Applied Mechanics Review*, 45:S3–S18, 1992.
- [50] J. Tersoff. New empirical approach to the structure and energy of covalent systems. *Physical Review B*, 37:6991–7000, 1988.
- [51] Q. Zhao, M.B. Nardelli, and J. Bernholc. Ultimate strength of carbon nanotubes:a theoretical study. *Physical Review B*, 65:144105, 2002.

- [52] M.B. Nardelli, B.I. Yakobson, , and J. Bernholc. Brittle and ductile behavior in carbon nanotubes. *Physical Review Letters*, 81:4656, 1998.
- [53] P. Zhang, Y. Huang, P.H. Geubelle, P.A. Klein, and K.C. Hwang. The elastic modulus of single-wall carbon nanotubes: a continuum analysis incorporating interatomic potentials. *International Journal of Solids and Structures*, 39:3893–3906, 2002.
- [54] P. Zhang, J. Jiang, Y. Huang, P.H. Geubelle, and K.C. Hwang. An atomistic-based continuum theory for carbon nanotubes: analysis of fracture nucleation. *Journal of the Mechanics and Physics of Solids*, 52:977–998, 2004.
- [55] M. Arroyo and T. Belytschko. An atomistic-based finite deformation membrane for single layer crystalline films. *Journal of the Mechanics and Physics of Solids*, 50(9):1941–1977., 2002.
- [56] R. Hill. On the theory of plane strain in finitely deformed compressible materials. *Mathematical Proceedings of the Cambridge Philosophical Society*, 86:161–178, 1979.
- [57] P. Zhang, Y. Huang, H. Gao, and K.C. Hwang. Fracture nucleation in single-wall carbon nanotubes under tension: a continuum analysis incorporating interatomic potentials. *Journal of Applied Mechanics*, 69:454–458, 2002.
- [58] D. Srivastava, C. Wei, and K. Cho. Nanomechanis of carbon nanotubes and composites. *Applied Mechanics Review*, 56:215–229, 2003.
- [59] H. Jiang, X.Q. Feng, , Y. Huang, K.C. Hwang, and P.D. Wu. Defect nucleation in carbon nanotubes under tension and torsion: Stone-wales transformation. *Computer Methods in Applied Mechanics and Engineering*, 193:3419–3429, 2004.
- [60] H. Jiang, P. Zhang, B. Liu, Y. Huang, P.H. Geubelle, H. Gao, and K.C. Hwang. The effect of nanotube radius on the constitutive model for carbon nanotubes. *Computational Materials Science*, 28:429–442, 2003.
- [61] Wang Yu amd Wang Xiu Xi and Xianggui Ni. Atomistic simulation of the torsion deformation of carbon nanotubes. *Modelling and Simulation in Materials Science and Engineering*, 12:1099 – 1107, 2004.
- [62] B. Liu, Y. Huang, H. Jiang, S. Qu, and K.C. Hwang. The atomic-scale finite element method. *Computer Methods in Applied Mechanics and Engineering*, 193:1849–1864, 2004.
- [63] B. Liu et al. Atomic-scale finite element method in multiscale computation with applications to carbon nanotubes. *Physical Review B*, 72:035435, 2005.

- [64] Y. W. Kwon and S.H Jung. Atomic model and coupling with continuum model for static equilibrium problems. *Computers and Structures*, 82:1993 – 2000, 2004.
- [65] Arash Mahdavi and Eric Mockensturm. A new hierarchical technique for the multiscale modeling of carbon nanostructures. *Proceedings of IMECE2005, 2005 ASME International Mechanical Engineering Congress and Exposition November 5-11, 2005, Orlando, Florida, USA*.
- [66] L. Nasdala, G. Ernst, M. Lengnick, and H. Rothert. Finite element analysis of carbon nanotubes with stone-wales defects. *CMES-Computer Modeling in Engineering and Sciences*, 7(3):293–304, 2005.
- [67] S. L. Mayo, B. D. Olafson, and W. A. Goddard (III). Dreiding: A generic force field for molecular simulations. *Journal of Physical Chemistry*, 94:8897–8909, 1990.
- [68] M. I. Baskes. Modified embedded-atom potentials for cubic materials and impurities. *Physical Review B*, 46:2727–2742, 1992.
- [69] S. J. Stuart, A. B. Tutein, and J. A. Harrison. A reactive potential for hydrocarbons with intermolecular interactions. *Journal of Chemical Physics*, 112:6472–6486, 2000.
- [70] S. V. Dmitriev, J. Li, N. Yoshikawa, Y. Tanaka, Y. Kagawa, T. Kitamura, and S. Yip. Breaking atomic bonds through vibrational mode localization. *Defect and Diffusion Forum*, 233-234:49–59, 2004.
- [71] J. K. Knowles and ELI Sternberg. On the ellipticity of the equations of non-linear elastostatics for a special material. *Journal of Elasticity*, 5(3-4):341–361, 1975.
- [72] J. Li, T. Zhu, S. Yip, K.J. Van Vliet, and S. Suresh. Elastic criterion for dislocation nucleation. *Materials Science and Engineering A*, 365:25–30, 2004.
- [73] J.R. Ray and M.C. Moody. Molecular dynamics calculation of elastic constants for a crystalline system in equilibrium. *Physical Review B*, 32(2):733–735, 1986.
- [74] J.F. Lutsko. Stress and elastic constants in anisotropic solids: Molecular dynamics techniques. *Journal of Applied Physics*, 64(3):1152–1154, 1988.
- [75] J. Lu and L. Zhang. Analysis of localized failure of single-wall carbon nanotubes. *Computational Materials Science*, 2005 (in press).

- [76] M. S. Daw and M. I. Baskes. Embedded-atom method: Derivation and application to impurities, surfaces, and other defects in metals. *Physical Review B*, 29:6443–6453, 1984.
- [77] M. Silhavy. *The Mechanics and Thermodynamics of Continuous Media*. Seiten - Springer, Berlin, 1997.
- [78] J.H. Irving and J.G. Kirkwood. The statistical mechanical theory of transport processes.iv. the equations of hydrodynamics. *The Journal of Chemical Physics*, 18(6):817–829, 1950.
- [79] L. Van Dommelen. Physical interpretation of the virial stress. <http://www.eng.fsu.edu/~dommelen/papers/virial/mosaic/index.html>.
- [80] K.S. Cheung and S. Yip. Atomic-level stress in an inhomogeneous system. *Journal of Applied Physics*, 70(10):5688–5690, 1991.
- [81] S.P. Shen and S.N. Atluri. Atomic-level stress calculation and continuum-molecular system equivalence. *CMES-Computer Modeling in Engineering and Sciences*, 6(1):91–104, 2004.
- [82] Z.S. Basinski, M.S. Duesberry, and R. Taylor. Influence of shear stress on screw dislocations in a model sodium lattice. *Canadian Journal of Physics*, 49:2160–2180, 1971.
- [83] A. I. Murdoch. On the microscopic interpretation of stress and couple stress. *Journal of Elasticity*, 71:105–131, 2003.
- [84] A. I. Murdoch and D. Bedeaux. Continuum equations of balance via weighted averages of microscopic quantities. *Proceedings of the Royal Society A: Mathematical, Physical and Engineering Sciences*, 445:157–179, 1994.
- [85] T. Dumitrica, T. Belytschko, and B. I. Yakobson. Bond-breaking bifurcation states in carbon nanotube fracture. *Journal of Chemical Physics*, 118(21):9485–9488, 2003.
- [86] N. Chandra, S. Namilaee, and C. Chet. Local elastic properties of carbon nanotubes in the presence of stone-wales defects. *Physical Review B*, 69(9):094101, 2004.
- [87] S.L. Zhang, S.L. Mielke, R. Khare, D. Troya, R.S. Ruoff, G.C. Schatz, and T. Belytschko. Mechanics of defects in carbon nanotubes: Atomistic and multiscale simulations. *Physical Review B*, 71:115403, 2005.
- [88] M.B. Nardelli, B.I. Yakobson, and J. Bernholc. Mechanism of strain release in carbon nanotubes. *Physical Review B*, 57(8):R4277–R4280, 1998.

- [89] B.I. Yakobson. Mechanical relaxation and “intramolecular plasticity” in carbon nanotubes. *Applied Physics Letters*, 72(8):918–920, 1998.
- [90] D. Troya, S.L. Mielke, and George C. Schatz. Carbon nanotube fracture - difference between quantum mechanical mechanisms and those of empirical potentials. *Chemical Physics Letters*, 382:133–141, 2003.
- [91] H. M. Westergaard. Bearing pressures and cracks. *Journal of Applied Mechanics*, 6(2):A-49–A-53, 1939.
- [92] G. R. Irwin and J. A. Kies. Critical energy rate analysis of fracture strength. *Welding Journal-Welding Research Supplement*, 33:193-s – 198-s, 1954.
- [93] N. N. Pugno and R. S. Ruoff. Quantized fracture mechanics. *Philosophical Magazine*, 84(27):2829–2845, 2004.
- [94] Robb Thomson, C. Hsieh, and V. Rana. Lattice trapping of fracture cracks. *Journal of Applied Physics*, 42(8):3154, 1971.
- [95] Peter Gumbsch and R. M. Cannon. Atomistic aspects of brittle fracture. *MRS Bulletin*, pages 15–20, May 2000.
- [96] A. Needelman. A continuum model for void nucleation by inclusion debonding. *Journal of Applied Mechanics*, 54:525–531, 1987.
- [97] V. Tvergaard. *Material failure by void growth to coalescence*. Academic Press, 1990.
- [98] A. Needelman. An analysis of deshesion along an interface. *Journal of the Mechanics and Physics of Solids*, 38:289–324, 1990.
- [99] V. Tvergaard and J. W. Hutchinson. The relation between crack growth resistance and fracture process parameters in elastic-plastic solids. *Journal of the Mechanics and Physics of Solids*, 40:1377–1397, 1992.
- [100] B. Yang, S. Mall, and K. Ravi-Chandar. A cohesive zone model for fatigue crack growth in quasibrittle materials. *International Journal of Solids and Structures*, 38:3927–3944, 2001.
- [101] R. L. Blumberg Selinger, Zhen-Gang Wang, W. M. Gelbart, and Avinoam Ben-Shaul. Statistical-thermodynamic approach to fracture. *Physical Review A*, 43(8):4396, 1991.
- [102] Nasa awards \$11 million “quantum wire” contract to rice., 2005. <http://www.nasa.gov/centers/johnson/news/releases/J05-018.html>.

- [103] B. Liu, H. Jiang, H. T. Johnson, and Y. Huang. The influence of mechanical deformation on the electrical properties of single wall-carbon nanotubes. *Journal of the Mechanics and Physics of Solids*, 52:1–26, 2004.
- [104] K. Nordlund and P. Hakonen. Nanotube: Controlling conductance. *Nature-Materials*, 4:514, 2005.
- [105] An interview with Dr. Richard Smalley., 2002. ESI Special Topics, <http://www.esi-topics.com/nano/interviews/Richard-Smalley.html>.
- [106] D. Qian, G.J. Wagner, and W.K. Liu. Mechanics of carbon nanotubes. *Applied Mechanics Review*, 55:495–532, 2002.
- [107] A.J. Stone and D.J. Wales. Theoretical studies of icosahedral c_{60} and some related species. *Chemical Physical Letters*, 128:502–503, 1986.
- [108] P. Zhang, P. E. Lammert, and V. H. Crespi. Plastic deformations of carbon nanotubes. *Physical Review Letters*, 81:5346–5349, 1998.
- [109] P. Zhang and V. H. Crespi. Plastic deformations of boron-nitrid nanotubes: An unexpected weakness. *Physical Review B*, 62:11050–1105, 2000.
- [110] H. J. Choi, J. Ihm, S. G. Louie, and M. L. Cohen. Defects, quasibound states, and quantum conductance in metallic carbon nanotubes. *Physical Review Letters*, 84:2917–2920, 2000.
- [111] Ge.G. Samsonidze, G.G. Samsonidze, and B.I. Yakobson. Kinetic theory of symmetry-dependent strength in carbon nanotubes. *Physical Review Letters*, 88(6):065501, 2002.
- [112] T. Dumitrica and B.I. Yakobson. Strain-rate and temperature dependent plastic yield in carbon nanotubes from *ab initio* calculations. *Applied Physics Letters*, 84(15):2775–2777, 2004.
- [113] Ge.G. Samsonidze, G.G. Samsonidze, and B.I. Yakobson. Energetics of stone-wales defects in deformations of monoatomic hexagonal layers. *Computational Materials Science*, 23:62–72, 2002.
- [114] M. J. Gillan. Calculation of the vacancy formation energy in aluminium. *Journal of Physics: Condensed Matter*, 1:689–711, 1989.
- [115] B. C. Pan, W. S. Yang, and Jinlong Yang. Formation energies of topological defects in carbon nanotubes. *Physical Review B*, 62(19):12652, 2000.

- [116] H. F. Bettinger, T. Dumitrica, G. E. Scuseria, and B. I. Yakobson. Mechanical induced defects and strength of bn nanotubes. *Physical Review B*, 65:041406, 2002.
- [117] L. G. Zhou and San-Qiang Shi. Formation energy of stone-wales defects in carbon nanotubes. *Applied Physics Letters*, 83(6):1222, 2003.
- [118] W. H. Moon and H. J. Hwang. A force field approach of structure and formation energy of defects of boron nitride nanotubes with tetragon-octagon pairs. *Materials Letters*, 58:2331–2334, 2004.
- [119] W. H. Moon and H. J. Hwang. Molecular-dynamics simulation of defect formation energy in boron nitride nanotubes. *Physics Letters A*, 320:446–451, 2004.
- [120] P. Piquini, R. J. Baierle, T. M. Schmidt, and A. Fazzio. Formation energy of native defects in bn nanotubes: an ab initio study. *Nanotechnology*, 16:827–831, 2005.
- [121] J.D. Eshelby. The determination of the elastic field of an ellipsoidal inclusion, and related problems. *Proceedings of the Royal Society of London. A*, 241:376–396, 1957.
- [122] J.D. Eshelby. The elastic energy-momentum tensor. *Journal of Elasticity*, 5:321–335, 1975.